# A method for in situ SEM fracture studies of brittle materials using the double torsion technique: Application to nuclear graphite




Kathryn A. Rosie

*A thesis submitted for the degree of Master of Science*

August 2011

# Declaration

1. I know that plagiarism is wrong. Plagiarism is to use another's work and pretend that it is one's own.

2. I have used the Vancouver convention for citation and referencing. Each significant contribution to, and quotation in, this project from the works of other people has been attributed, and has been cited and referenced.

3. This project is my own work.

4. I have not allowed, and will not allow anyone to copy my work with the intention of passing it off as his or her own work.

SIGNED:

Kathryn Rosie
RSXKAT004

08/08/2011

# Acknowledgements

The following people contributed their brains, time, services, and patience to this thesis, and I am truly grateful to all of them, and to everyone not mentioned who supported me throughout.

- To Professor Bob Tait, as always, for his enthusiasm, support, understanding, and guidance. My academic and professional career would be nowhere near where it is today had not been for his efforts and advice.

- To PBMR Ltd. and the South African Nuclear Energy Corporation (NECSA) for financial assistance throughout the course of this project.

- To Thorsten Becker, who is a fracture mechanics, nuclear graphite, and double torsion guru. Many thanks for the hours spent talking through ideas with me, and for proof reading various chapters. Also to Dr Mahmoud Mostafavi for running DIC analyses on selected image sequences; his time is greatly acknowledged.

- To Glen Newins, Horst Emrich, and all the staff at the UCT Department of Mechanical Engineering workshop for the construction of the parts for the mini-DT rig. Their unwavering patience with students is to be admired. Huge gratitude also goes to Philip Potgieter of Strident Engineering, who performed modifications to the rig under immense pressure, assisting me and inspiring me all over again.

- To Julian Mayer, for stepper motor help, fascinating conversations on old watches, and for teaching me how to attach strain gauges correctly. Also to Tracy Booysen for electronics and data acquisition help, and for lending me the data acquisition card.

- To Miranda Waldron and James Duncan of the Electron Microscope Unit (EMU). Without their accommodation, the project would never have hap-

pened. James' willingness to stay up until strange hours of the morning offering technical insight into the workings of the SEM was invaluable, as was his Rooibos tea. Miranda on dayshift provided training and support and answers to my silliest questions. Special thanks must also be made to both them and the EMU for letting me poke holes in their SEM.

- To my partner, Nicholas Roux, not only for putting up with my strange hours and unwillingness to cook supper, but also for his electronics skills, which made the stepper motor controller and associated circuitry happen.
- To the staff and students of the Centre for Materials Engineering, especially Dr Sarah George, Naseeba Abbas, and Liezl Matthews for their sharing their knowledge of etching, polishing, and cutting techniques.

And to my dad, for being proud of me.

# List of Figures

# List of Symbols

| Symbol | Description | Units |
|---|---|---|
| $a$ | Crack length | m, mm |
| $A$ | Constant describing the intercept of a v-K curve | |
| $d$ | Thickness of the double torsion specimen | m, mm |
| $E$ | Young's Modulus | GPa |
| $E'$ | Subsitution for plane stress/strain expression for Young's Modulus | GPa |
| $\varepsilon$ | Strain, usually measured in microstrain | $\mu\varepsilon$ |
| $f$ | Frequency of activation of stepper motor coil transistors | Hz |
| $G$ | Elastic strain energy release rate | $^{\mathrm{J}}/_{\mathrm{m}^2}$ |
| $\gamma_e$ | Elastic surface energy term | |
| $K_{\mathrm{I}}$ | Mode I stress intensity factor | $\mathrm{MPa}\sqrt{\mathrm{m}}$ |
| $K_{\mathrm{Ic}}$ | Fracture toughness | $\mathrm{MPa}\sqrt{\mathrm{m}}$ |
| $n$ | Constant describing the slope of a v-K curve | |
| $\nu$ | Poisson's ratio | |
| $\psi$ | Thickness correction factor in the analyses of a DT specimen | |
| $P$ | Load | N |
| $P_{peak}$ | Maximum allowable load applicable to the load cell before plasticity occurs | N |
| $R$ | Crack resistance | $^{\mathrm{J}}/_{\mathrm{m}^2}$ |
| $\sigma$ | Stress, commonly applied stress | MPa |
| $U$ | Energy involved in crack propagation | J |
| v | Crack velocity da/dt | m/s |
| $\omega$ | RPM of input motor | rev/min |
| $W$ | Width of the double torsion specimen | m, mm |
| $w_m$ | Moment arm from DT specimen centreline to loading point | m, mm |

# Glossary of Terms

**Compliance** The inverse of stiffness. In the case of the DT specimen, a measure of how much torsional deformation is present in the two symmetrical arms.

**CT** Compact Tension. A fracture mechanics specimen which applies a tensile load to either side of a notched region in order to induce a crack at the notch.

**DAQ** Data acquisition card. A device which is used to collect either analog or digital input, and log it electronically via appropriate software, from where it may be manipulated.

**DIC** Digital image correlation. A computer algorithm that subtracts one image from another to highlight the differences.

**DT/Double Torsion** The method of loading a rectangular specimen where a crack is induced lengthways down the specimen by applying a four point bending load to one short edge.

**PBMR** Pebble bed modular reactor. A graphite moderated nuclear reactor design.

**R-Curve** Curve describing the crack resistance of a material as a function of crack length.

**SEM** Scanning electron microscope.

**SENB** Single Edge Notched Bend. A fracture mechanics specimen which applies a bending load to a notched beam in order to induce a crack at the notch.

**v-K Curve** Curve relating crack velocity to applied stress intensity factor. This curve is descriptive of slow cracking for all geometries of a given material and in a given environment.

**VDU** Visual display unit

# Summary

This work concerned the design and development of a miniature double torsion (DT) testing rig, for use inside the chamber of a scanning electron microscope, to perform *in situ* loading studies of brittle materials using the DT fracture mechanics specimen. The double torsion method is unique in the study of brittle materials as a constant stress intensity can be generated at the crack tip, which is not possible with other specimens types (SENB, CT, etc). This aids in the control of slow crack growth, as it results in a crack velocity which is *independent* of crack length.

A number of constraints were present as a result of the SEM environment. The 'mini-DT' rig was developed to hold and load the specimen in a symmetrical manner inside the chamber. The materials of construction were 6-series aluminium and stainless steel grade 316, both non-magnetic and conductive. Loading was achieved through a movable crosshead driven by a stepper motor through a 400:1 gear reduction system. The maximum displacement rate of the crosshead was approximately 0.1mm/min, whereas the minimum rate was, for practical purposes, infinite due to the pulse function built into the stepper motor control which allowed for pulses equating to a crosshead displacement of approximately 80nm/pulse.

The peripheral system also included a strain indicator connected to a data acquisition card (DAQ), which enabled the recording of the applied load sequences, and a video capture card, although this feature was not used extensively.

The rig was applied to the study of nuclear graphite, where previously, only macro studies had been performed on nuclear graphite in double torsion. This allowed for real-time observations of damage development in the material on a smaller scale than has been achieved previously.

Nuclear graphite of designation 'S' as provided by PBMR Ltd. was tested in the SEM, using the system. This was an intermediate grained graphite, with maximum grain sizes of $180 - 200\mu$m. Successful observations were made of the cracking behaviour, which confirmed that the weakest areas in a graphite matrix is the filler particle/binder interface. Digital image correlation was performed on some image

sequences, but did not show significantly more information than could be seen in the SEM micrographs.

The *in situ* performance of the system inside the SEM was highly satisfactory, allowing a wide range of x- and y- displacements (necessary to follow a growing crack), while still providing free rotation of the attached stepper motor. Crack growth rates of down to 19nm/s were directly observed in PMMA specimens.

While various issues were identified with the data collection instruments and methods, these systems were peripheral to, and had no effect on, the specimen loading apparatus. Recommendations were, however, made as to how noise and uncertainty could be minimised in these regards.

It was concluded that the technique displayed merit in its ability to contribute to the knowledge base of slow cracking and damage development in brittle materials, with the advantage being that the gearing ratios of the current device resulted in slower specimen loading rates, which were more controlled, than reported previously.

# Table of Contents

# Chapter 1

# Introduction

## 1.1 Subject of this Thesis

This project concerned the development of a miniature Double Torsion testing rig for use *in situ* inside a scanning electron microscope (SEM). The double torsion specimen is a fracture mechanics specimen that is especially useful in the study of controlled slow crack growth in brittle materials. The method and mechanism is expanded upon in Section 1.2.1.

The purpose of an *in situ* mechanical testing rig in the SEM is to perform load tests on specimens, which would otherwise be performed on a larger specimen in a conventional loading machine. By performing such a test on a smaller specimen inside the SEM chamber one can directly observe and correlate the loading response of the specimen to a microstructural event that may be witnessed via the SEM visual display unit, and recorded on a micrograph. This enables a greater understanding of the influence of the microstructure on the general behaviour of the material, which may then be incorporated into behavioural models, etc.

The current research, reported in this thesis, seeks to develop a method of loading DT specimens while being able to observe directly the effect of this loading on the microstructure of the material in question, as well as to try and comment on the suitability of the technique in the context of the macro-work already performed. The particular application of the current work was to nuclear graphite, an integral material in the design of the proposed Pebble Bed Modular Reactor, discussed later.

In summary, the project covers the design and development of the testing rig, and presents insights into the fracture and micro-cracking behaviour of nuclear graphite from observation of the double torsion fracture mechanics specimen under load.

## 1.2 Background

Electricity availability in South Africa is key to the continued development of the country's economy. However, supply is under strain, with the country's electricity provider, ESKOM, seeking alternative power supplies to aid the ageing power stations currently in use [1].

The pebble bed modular reactor (PBMR) is a widely attractive solution based on its proclaimed inherently safe nuclear characteristics and its ability to use multiple coupled reactors to produce a larger output, depending on the perceived demand [2]. It is a high-temperature, graphite-moderated, helium-cooled reactor, the design of which originated with Germany's HTR [3], and is currently being researched in China with their operational HTR-10 reactor [4].

The primary motivation for the current work was the development of a method to investigate the microstructural response of nuclear graphite to loading for the purposes of the PBMR project which was ongoing in South Africa at the time, of which the double torsion technique is a highly suitable method. During the course of this work, however, the PBMR project was suspended. It was for this reason, that while there is still a need to understand the response of nuclear graphite under load for reasons given below, certain parts of the work have been expanded to make comment on the applicability of the method to other brittle and quasi-brittle materials in general.

The double torsion technique will now be described briefly, along with an introduction to nuclear graphite in the PBMR, and why it is of use to understand the slow cracking behaviour in this material.

### 1.2.1 The Double Torsion Technique

The Double Torsion (DT) technique is a valuable method in the fracture mechanics testing of brittle materials due to its ability to sustain a relatively long crack when compared to commonly utilised techniques such as compact tension (CT), or single edge notched bend (SENB) specimens, without fast fracture occurring. This is because its unique configuration produces a stress intensity that is *independent* of crack length, unlike the other conventional fracture mechanics specimens. It comprises a Double Cantilever Beam which has each arm loaded in torsion, as opposed to bending (refer to Figure 1.1). It has been widely used for a number of decades now [5, 6, 7, 8, 9, 10], without any standard method for performing experiments associated with it. Tait, Fry & Garrett [11] performed an extensive review of the method

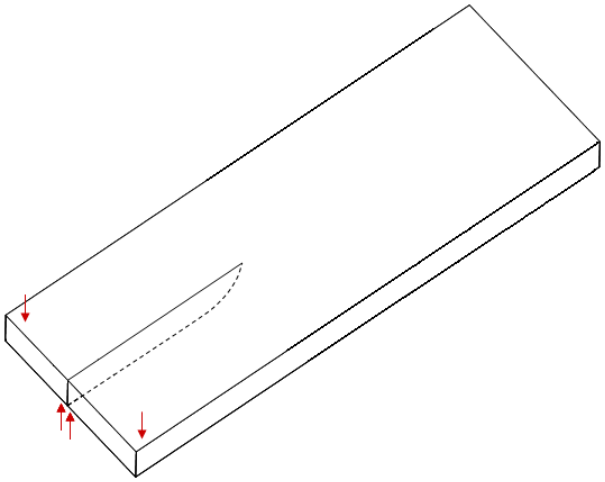

**Figure 1.1:** Double Torsion specimen configuration

in an attempt to provide some direction as to the best approach when analysing the specimen, and this work in standardising the process was continued by Becker in his investigation into the effects of the various techniques and corrections that have been proposed over the years [12, 13].

Using the Double Torsion technique, the various fracture mechanics parameters have been determined for nuclear graphite within a certain degree of confidence [12]. The work now extends to a miniature application of the technique, which may be used to study the effect of the microstructure on the crack propagation behaviour and properties of nuclear graphite. This involves the design and placement of a double torsion rig inside a scanning electron microscope (SEM) and performing the experiments inside the SEM chamber. Because of the presented crack length independent stress intensity factor, or constant crack driving force, the foundation is laid for a more in depth study of the various factors affecting damage development in nuclear graphite and other brittle materials, from a microstructural perspective.



### 1.2.2 The in situ SEM Method

The first attainable references to use of the *in situ* SEM technique are by Higgins & Bailey [14], and Roberts *et al* [15], in 1976, all of whom used a tensile setup in the SEM chamber. In 1977, the first use of a bending rig *in situ* was reported by Akers *et al* [16]. The technique gained popularity in the following decade, which saw the development of a number of tensile, compression, and fatigue loading stages [17, 18, 19, 20, 21, 22, 23, 24].

Perhaps the first report of the double torsion technique being adapted for SEM

use is by Tait & Bohm [21] in 1980, who utilised its suitability to brittle materials to examine fracture in concrete. By 1986, the *in situ* double torsion technique had been developed further [25], and used in the study of cement mortar and cement paste [26].

Various factors must be considered when developing a device for use inside the SEM chamber, as the particular environment is demanding in terms of vacuum integrity and electromagnetic interference, amongst others. With non-commercial devices, modifications to the chamber are often necessary, and it is incumbent upon the designer to devise solutions without compromising the conditions which the SEM relies on to function. Chapter 3 describes these factors in detail, while Chapter 4 explores previous solutions to the various issues.

In terms of the fracture mechanics theory behind the introduction and propagation of cracks in a material, the following section introduces the main concepts, while Chapter 2 explores them in detail.



### 1.2.3 Sub-critical Crack Growth

'Critical crack growth' is the term used to describe fast fracture, which occurs at or above a certain value of stress intensity, known as the fracture toughness, $K_{Ic}$.

Sub-critical crack growth, as the name suggests, is crack propagation which occurs below the material fracture toughness. One of the more commonly known mechanisms of sub-critical crack growth is fatigue, or load cycle dependent crack propagation. This occurs predominantly in ductile materials, which can develop a relatively large zone of plasticity at the crack tip when compared to brittle materials.

In brittle materials, a mechanism known as sustained load fracture is more often observed, which is characterised by *time*-dependent slow crack propagation. Causes for this occurance in structures can range from stress corrosion cracking to hydrogen embrittlement, or creep crack growth [27].

In nuclear graphite structures such as those in the PBMR, which withstand large sustained loads without operational variation, it is reasonable to assume that slow, sustained load cracking is the predominant method of sub-critical crack growth. This is enabled by brittle grain boundary separation and binder cleavage, observed previously is brittle materials [21, 26, 28]. The exact behaviour in nuclear graphite, however, remains unknown due to lack of observation of the material response to loading at the microstructural level.

### 1.2.4 The PBMR and Nuclear Graphite

Graphite has two nuclear functions in the reactor unit of the PBMR. The first is as a moderator in the core, where it is used to slow down neutrons in order to improve their reaction cross-section (i.e. their probability of intersection with another particle). The second function is as a reflector, which, amongst other functions, prevents neutron leakage to the outer reactor vessel, as well as returning escaped neutrons to the core. This minimises the amount of fissionable material needed to produce a self-sustaining nuclear chain reaction. Both the fuel particles (pebbles) and the inner core structures are constructed using nuclear graphite.

A reflector structure might consist of 36 columns of graphite blocks [29], arranged inside the outer steel pressure vessel which has a diameter of approximately 6.2m and a height of 27m. The graphite lining is 1m thick [12]. A simple calculation shows that the mass of graphite alone produces a force of approximately 1.9MN at the lower end of the reactor. However, as a further consideration, the graphite blocks are keyed to one another to hold them in place [29], and the keyways provide an added stress concentration from which cracks may initiate and propagate into the structure. It is this initiation and its subsequent mechanisms of propagation which is of interest in the current research.

There are various factors which affect the properties of graphite and hence influence the functionality of the graphite in both a nuclear and structural sense. These include irradiation, oxidation, temperature, and environmental effects, amongst others. The effect of these factors on the nuclear functioning of graphite has been covered by various researchers [30, 31, 32], and for the structural part there have been many attempts at mechanical testing on various forms of virgin, irradiated and oxidised graphite [33, 34, 35, 36, 37] in order to understand the implications of these factors. These effects will be discussed in more detail in a later section.

The goal of the multiplicity of testing that is being conducted is to gain a sound understanding of the material performance parameters and to understand the effects of the aforementioned factors on these parameters, so that the information may be used in concurrence with failure models. Various models have been put forward, such as the statistical Weibull and Batdorf models [38], as well as various finite element models [4, 39, 40] amongst others. An alternative method for the assessment of the structural integrity of graphite components is fracture mechanics, and it has been given notable attention by Tucker [41] and Burchell [42], with much work being put into the understanding of the graphite microstructure [36, 43, 44, 45].

From a fracture mechanics point of view, the stress intensity parameter is a useful

method of characterising potential for damage, and of performing life predictions when equipped with a thorough understanding of the behaviour of the material and the mechanisms involved in such damage propagation. The issue is that with most fracture mechanics test specimens being used in the various studies mentioned, the stress intensity (i.e. "driving force" behind crack growth) is dependent on crack length. This has the result of exponential crack growth, resulting in fast fracture within a short length, which is not conducive to studying the slow cracking behaviour of the material. This, as explained earlier, is the strength behind the concept of performing fracture mechanics tests using the double torsion method, where the driving force is regarded as constant.

## 1.3 Objectives

Given the previous work done by T. Becker within the UCT nuclear graphite research group, and the technique for double torsion testing which was developed and optimised, the objectives of this project were both to extend the method to a microstructural testing level, and to qualify the results of the macro-work by investigating the crack propagation behaviour in the nuclear graphite provided. An additional objective was to have the designed solution be adaptable to different materials over a suitable range of fracture toughnesses. Delineated, these objectives were therefore to:

- Develop a miniature double torsion test rig that is compatible with the chamber of a scanning electron microscope, in congruence with previous literature on the subject. Design for a suitable range of fracture toughness so as to ensure adaptability;
- Use the aforementioned rig to perform fracture mechanics tests, *in situ* in the SEM, on specimens of nuclear graphite provided by PBMR, using the recommendations of T. Becker [12];
- Gain an understanding of the results of the macro-DT testing in nuclear graphite, and the influence of the microstructure on the results of these tests;
- Investigate the slow crack propagation behaviour of the nuclear graphite using this method;
- Discuss the findings and make recommendations for both the experimental technique used, as well as

- Discuss any implications for the study of nuclear graphite arising out of the observations made during material testing.

## 1.4 Scope of this Project

This project covers both the *design and construction* of a miniature fracture mechanics Double Torsion test rig, as well as the *testing* of the supplied nuclear graphite by means of this rig inside a scanning electron microscope (SEM). Analysis of the visual output of the SEM as well as electronic monitoring of applied loading are the two tools which were used to evaluate and interpret the behaviour of the tested material. Image analysis included computational investigation of the SEM imagery through the digital image correlation (DIC) technique, but this is the limit to which computational techniques were used to evaluate the test material. That is, this was a purely **experimental** investigation, and no modelling by means of the finite element method or other such techniques was undertaken.



## 1.5 Plan of Development

This report covers two distinct areas of work. The first, predominant, part refers to the design and development of a working miniature double torsion test rig for use inside a scanning electron microscope, while the second part deals with its use in investigating the microstructural and crack propagation behaviour of brittle materials, specifically nuclear graphite, under load.

Chapter 2 gives a background to the relevant fracture mechanics theory which applies to this project; this foundation is necessary in order to understand the double torsion concept fully, and is also required for the design of the device which makes use of these principles. An overview of the current understanding of the fracture behaviour of brittle materials, nuclear graphite, and the factors which affect these, is also presented in this chapter. This provides a reference from which to draw in the experimental phase of the project.

Chapter 3 provides information on the various practical elements involved in the design portion of this project. It reviews the double torsion method in brief, and describes the various elements to consider when adapting a macro test method for use inside a SEM chamber, which is sensitive to interference of various kinds. It also provides examples of previous devices which have been produced for this purpose.

Chapter 4 then explains the design process and provides technical details of

the final product. Chapter 5 consists of the methodology and results of an initial system evaluation, conducted before the rig was installed inside the scanning electron microscope. In Chapter 6, the method used in, and results from, the material testing phase are presented. Chapter 7 discusses the performance of the miniature double torsion system in its entirety, while Chapter 8 gives conclusions on, and recommendations for, the work performed.

# Chapter 2

# Fracture Mechanics and Graphite

The predominant methods which are used in the analysis of nuclear graphite are statistical, due to the large scatter in strength and non-linear response exhibited by the material, with the Weibull method often being reported [38, 39, 46].

While statistical methods are respresentative of the average behaviour of large populations, they have a disadvantage in that they are unable to predict the failure probability of a single item where the state of damage is explicitly known, or easily determined. Nemeth and Bratton [38] performed an in-depth review of existing statistical models and concluded that a certain subset that were in use "appear to be reasonably robust in that they can be applied to materials that display distributed damage, provided that the level of disorder in the material is not too large." This shows that the strongest of the statistical models (in the opinion of those authors) is unable to account for individual flaws which may have propagated past the level of background damage.

With the rise of fitness-for-purpose techniques, it has been accepted that flaws are unavoidable in most cases and may be tolerated, provided the behaviour of the material containing that flaw may be predicted. This is the strength of fracture mechanics, in that it has definite means to deal with existing flaws which lead to the prediction of the remaining life time of the flawed component. In certain studies performed on nuclear graphite, researchers have concluded that statistical methods do not provide the best correlation to experimental data. In these cases they have found that fracture mechanics assessments provide a better description of the actual behaviour of the material [33, 41, 42]. Burchell commented, in a previous review done of several graphite failure theories, that a combination of fracture mechanics coupled with microstructural criteria provided the approach best able to encompass structural failure in graphite [42].

This chapter seeks to provide a background into fracture mechanics theory in general; a commentary on crack behaviour in brittle materials; and a more specific discussion of factors which might affect this behaviour, with a certain emphasis on nuclear graphite.

## 2.1 Overview of Fracture Mechanics

Fracture mechanics, as the name suggests, covers the analysis of structures that fail by fracture, as opposed to general yielding. Because yielding is so well understood, structures rarely fail by this mechanism, and it is realistic to say that most structural failures fall into the realm of fracture mechanics.

Fracture mechanics is the study of the initiation and propagation of cracks, and the behaviour of a material undergoing cracking may be described by various parameters. The most common are the elastic strain energy release rate, the crack resistance, and the stress intensity factor (also known as the stress intensity). These are discussed in the following sections, along with two mechanisms of crack growth, namely fatigue and sustained load fracture.

The majority of the explanations that follow, and further reading, may be found in books by Ewalds and Wanhill [27] and Broek [47].

### 2.1.1 Strain Energy Release Rate, $G$, and Crack Resistance, $R$

To explain where these two parameters come from, consider the total energy in a loaded plate that undergoes some cracking. The plate has unit thickness, infinite width, $W$, and a crack of length $2a$. The total energy may then be described as:

$$U = U_0 + U_a + U_\gamma - F \tag{2.1}$$

where:

$U_0$ is the elastic energy contained in the loaded (uncracked) plate;

$U_a$ is the change in elastic energy caused by cracking;

$U_\gamma$ is the change in elastic surface energy caused by the creation of two new surfaces;

$F$ is the work performed by external loading.

The elastic energy in the uncracked plate remains a constant in the expression, regardless of crack length, as it is a material property. The other terms may be seen

to either provide or absorb potential energy in the cracking mechanism. Assuming the external work is zero, the rate at which the total energy changes with changing crack length is given by the expression:

$$\frac{dU}{da} = \frac{d}{da}\left(U_a + U_\gamma\right) \tag{2.2}$$

The expressions for the two energy terms on the right side of equation 2.2 are:

$$\begin{aligned} U_a &= \frac{-\pi\sigma^2 a^2}{E'} \\ U_\gamma &= 2(2a\gamma_e) \end{aligned}$$

where for this and all subsequent equations:

$E' = E$ for plane strain, and

$E' = {}^{E}/_{(1-\nu^2)}$ for plane stress.

Therefore, the result of equation 2.2 becomes:

$$\frac{dU}{da} = -\frac{2\pi\sigma^2 a}{E'} + 4\gamma_e \tag{2.3}$$

In the initial stages of cracking the rate at which energy is given to the crack propagation process is less than the rate at which the energy is absorbed by the process, resulting in stable crack growth. At some stage the energy release rate becomes higher than the surface energy absorption rate, and the crack propagates unstably. This turning point happens when the two aforementioned rates are equal, i.e. ${}^{dU}/_{da} = 0$.

$$\therefore \frac{\pi\sigma^2 a}{E'} = 2\gamma_e \tag{2.4}$$

This process is illustrated in Figure 2.1. The left hand side of equation 2.4 is known as the elastic strain energy release rate, $G$, and the right hand side is called the crack resistance, $R$. Unstable crack propagation occurs when $G > R$.

Equation 2.4 is the expression for materials which have a linear elastic response, and are under plane strain conditions. In this case the value of $R$ is a constant with crack extension and therefore one can design for a critical value of $G$, denoted $G_c$. However, in materials which do not exhibit a linear response (e.g. in ductile materials or materials with a non-linearity inducing process zone at the crack tip), the value of $R$ is not a constant and so the concept of an *R-curve* is introduced. As a crack propagates in such a material the resistance to cracking also grows, with the consequence that at a certain level of stress a crack will propagate slowly and then

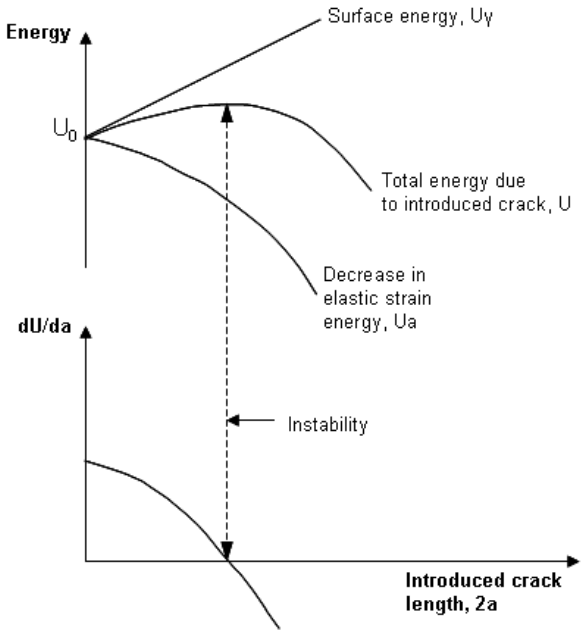


**Figure 2.1:** Energy balance for crack in infinite width plate. Reproduced from Ewalds & Wanhill [27]



arrest due to the fact that $R$ increases above the current value of $G(\sigma)$. The crack will only continue to propagate once a higher stress is applied, bringing $G$ above the increased $R$ value once more.

Although graphite is a generally brittle material, research has shown that nuclear graphite exhibits $R$-curve behaviour. Notable mention must be made of the work of Ouagne *et al* [35] who performed a number of tests for non-linear fracture mechanics parameters such as $R$, $J_R$ & $K_R$. They found that both fine and coarser grained graphites exhibited rising $R$-curve behaviour for a certain crack length before reaching a constant plateau region (as also found by Becker [12]), and then decreasing towards the end of the test. Their explanation is that energy dissipation processes in cracking contributed to the increasing fracture toughness in the first region of initial cracking. These dissipation processes include crack bridging by dislocated particles for a certain length of the crack wake region, as well as friction effects caused by the tortuosity of the crack path. During the plateau region the toughening effect is at equilibrium with the weakening effect of the process zone extending ahead of the crack tip. The decrease in $R$ values in the final stages of cracking are attributed again to the frontal process zone, this time coming into contact with and overlapping the end face of the test specimen. This process zone will be discussed in detail in Section 2.2.2.

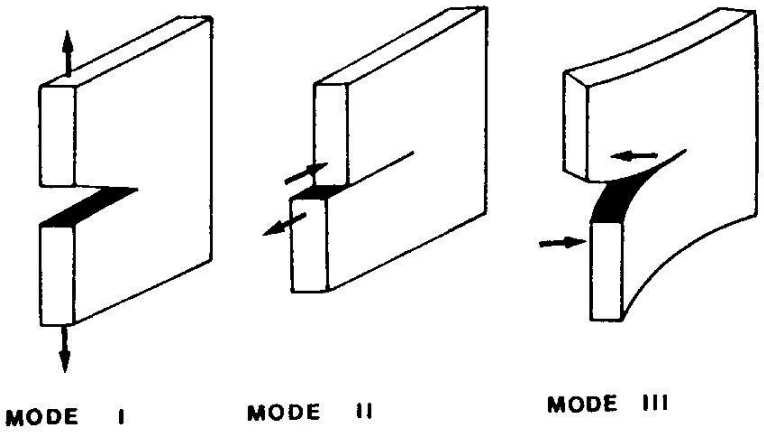


**Figure 2.2:** Modes I, II, and III fracture, in Broek [47]

There is much room in the current and future work to examine in real-time the events inferred in the above study, and to verify the exact mechanisms involved in the observed macro-behaviour.

### 2.1.2 Stress Intensity Factor, $K$

The stress intensity factor is a geometric combination of stress and flaw size, and is a measure of the magnitude of the elastic stress field immediately in front of a crack tip. For our purposes it is denoted by $K_{\mathrm{I}}$, referring to mode I crack propagation, i.e. tensile mode, as this is the most common stress state encountered in fracture problems [27]. For completeness, the two other recognised modes of fracture are mode II: in-plane shearing, and mode III: torsion, or out-of-plane shear. A representation of all three is given in Figure 2.2.

Mode I stress intensity is generally given by the formula:

$$K_{\mathrm{I}} = Y\sigma\sqrt{\pi a} \tag{2.5}$$

where:

$Y$ is a geometry correction factor, accounting for the shape of the crack and of the cracked specimen,

$\sigma$ is the remote stress experienced in the material, i.e. not the local crack tip stress,

$a$ is the characteristic size of the flaw, e.g. radius, or crack length.

The stress intensity may be seen as the "driving force" behind crack growth. The higher the stress intensity for a given stress state, the faster a crack will propagate

in a material. At a critical level of this parameter, unstable crack growth occurs. This critical value is known as the fracture toughness, and is denoted by $K_{\mathrm{Ic}}$.

The stress intensity concept has many applications, most notably fatigue and stress corrosion cases.

### 2.1.3 Fatigue

Fatigue is characterised by subcritical crack growth, which is defined as cracking that occurs under stresses far below the critical stress level that would produce fast fracture. It is incremental crack growth at alternating loads far below the yield or tensile strength of a material, and may be classed according to a variety of mechanisms, e.g. loading, thermal, or corrosion fatigue. Stress intensity, as mentioned, is the driving force behind the fatigue crack growth rate. In this particular case, though, one refers to the cyclic stress intensity amplitude, defined as:

$$\triangle K = K_{\max} - K_{\min}$$

which is a result of the cyclic stress $\triangle\sigma = \sigma_{\max} - \sigma_{\min}$ that the structure experiences.

The cyclic stress intensity of a fatigue crack may be determined by Equation 2.5, substituting for cyclic stress, and plotted against the incremental crack growth rate, $^{da}/_{dN}$. A plot throughout the lifetime of a material is represented in Figure 2.3, and is known as a Paris curve. Region II of this curve is described by Equation 2.6:

$$\frac{da}{dN} = C(\triangle K)^m \tag{2.6}$$

where:

$^{da}/_{dN}$ is the crack increment per single loading cycle,

$C$ is a constant describing the position of the curve on the axes,

$\triangle K$ is the cyclic stress intensity, and

$m$ is a constant describing the slope of the curve.

The first region of the curve is a threshold region, where a crack grows slowly but accelerates quickly. To the left of this curve the stress intensity range is too low to propagate a crack by fatigue, although not all materials exhibit this threshold value. The middle region is characterised by a fairly linear relationship between crack velocity (cycle-based) and stress intensity range. A crack will often spend the majority of its life in this region, which, as mentioned, is described by Equation 2.6

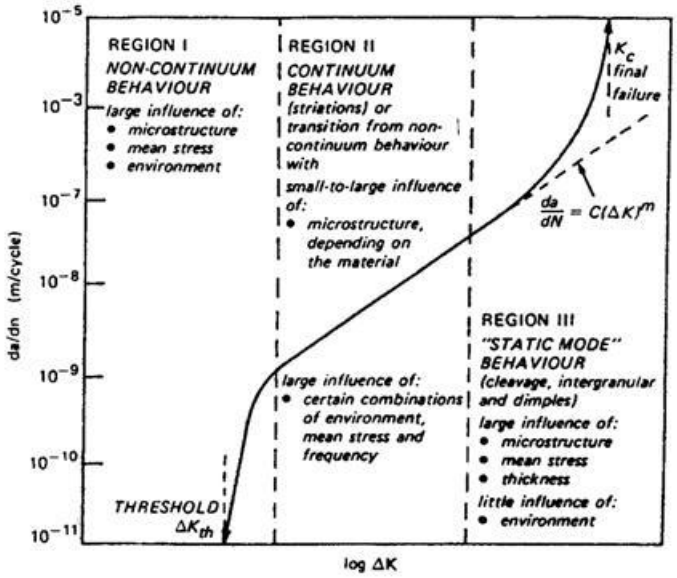


**Figure 2.3:** Typical Paris curve describing fatigue crack growth rate [27].

above. The final region is where the relationship becomes non-linear once more, and the fracture toughness is reached, where fast fracture occurs.

The usefulness of such a curve is that it may be determined for a well-known geometry in the laboratory, for a particular temperature and environment, and directly applied to any structure of the same material. That is, the constants $C$ and $m$ are material properties, which do not change with geometry or stress state, although there is a dependence on environment and temperature. Knowing this, such curves may be used predictively to estimate the remaining lifetime of a structure containing a flaw. This is done by rearranging Equation 2.6 and integrating with respect to flaw size, to which one gains the remaining load cycles until failure:

$$N = \frac{1}{C\left(Y\triangle\sigma\sqrt{\pi}\right)^m} \cdot \frac{2}{2-m}\left[a_c^{\frac{2-m}{2}} - a_i^{\frac{2-m}{2}}\right] \tag{2.7}$$

where:

$N$ is the number of cycles until fast fracture occurs,

$a_c$ is the critical crack length at which fast fracture occurs, which may be determined using Equation 2.5, and

$a_i$ is some starting crack length, which may refer to the current crack length if determining the remaining cycles to failure, or the largest detectable inherent flaw if determining total lifetime of a new structure.

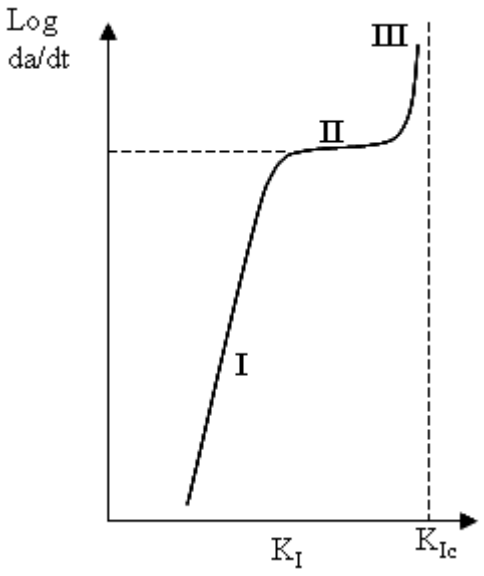


**Figure 2.4:** Typical v-K curve describing stress corrosion crack growth.



### 2.1.4 Sustained Load Fracture

Sustained load fracture is also characterised by subcritical crack growth. As the name suggests, it does not have to occur under cyclic loading as in fatigue, although sometimes these two mechanisms act in conjunction in a single scenario.

Many circumstances may bring about subcritical crack growth, and these include dissolution, diffusion, ion exchange, or microplasticity [12], but perhaps the most widely understood is stress corrosion. This occurs in a susceptible material with the right combination of applied stress and corrosive environment. It should be noted that air is often a suitably corrosive environment, as is anything carrying oxidising material. This applies in the case of the helium coolant in the reactor carrying gaseous impurities and material from the heat transfer and propulsion equipment.

Analogously to Equation 2.6, subcritical crack growth may be described by:

$$\frac{da}{dt} = AK^n \tag{2.8}$$

where:

$A$, $n$ are constants describing the position and slope of the curve. Analogous to $C$, $m$.

Similarly to a fatigue crack, the growth behaviour of an environmental crack exhibits three regions, as shown in Figure 2.4.

Region I is marked by the presence of a threshold at the lower end of the linear

relationship presented in Figure 2.4, although this may not be present in some materials. The crack velocity (time-based) in this region is highly dependent on stress intensity level and is the region where Equation 2.8 holds, while in Region II there is virtually no dependence on stress intensity at all. This is where the environmental conditions exert the most influence. In Region III the stress intensity becomes dominant again, leading to fast fracture, as in the fatigue case. A crack propagating in a structure will spend most of its lifetime in Region I.

### 2.1.5 Comment

Cracking in a material is often governed by either mechanism described above, or by a combination of both. *Macro*cracking in brittle materials such as graphite is mostly controlled by stress corrosion or another subcritical crack growth mechanism, and less often by fatigue. Thus it is of interest when studying the cracking likely to develop from the stress concentrations around keyways and control rod insertion holes, etc. to focus on the subcritical crack growth parameters, $A$ and $n$, and determine which factors affect these values. Factors mentioned by Becker [12] that are known to have an effect include: the stress intensity factor, temperature, activity of corrosive species, pressure, residual stress, and microstructure. Concerning the microstructure, it is reported that an increase in grain size decreases the value of $n$, meaning larger grained material becomes more susceptible to stress corrosion cracking at lower levels of stress intensity [48].

## 2.2 Crack Growth Behaviour in Brittle Materials

This section provides a general overview of the mechanisms involved in crack extension in brittle materials. This includes a discussion on toughening mechanisms, and provides a background to what behaviours may be observed during *in situ* experiments with brittle materials.

### 2.2.1 Crack Extension

Crack extension in brittle materials is commonly characterised by cleavage fractures, and may be further categorised as inter- or trangranular extension of a macrocrack. Intergranular extension is where the crack propagates by separation of grain boundaries. It is the lower energy form of growth, and signifies a point of weakness in the material. It is recognisable on a macro scale as a crack which follows closely

alongside grain boundaries. Transgranular extension, on the other hand, requires more energy as the crack propagates by cleavage of atomic bonds in a crystal lattice plane. On a macro scale, a crack is seen to propagate through grains, and across grain boundaries [27].

A further mechanism of growth is present in certain materials. Microcrack formation ahead of the macro crack tip has been recognised in various polycrystalline materials, commonly of the more porous variety, such as concrete [49], cement mortar [26], and graphite [36, 45]. Linking of microcracks, which then link up with the main crack, is a further method of crack propagation. The microcracks themselves may form by either inter- or transgranular cracking, as discussed above, and observation of their formation under load is necessary in order to ascertain the mode associated with a particular material. This knowledge enables one to characterise the energies associated with damage nucleation in the material.

### 2.2.2 Toughening Mechanisms

Material toughening is associated with a dissipation of crack-driving energy (e.g. due to applied forces). In cases where there is little dissipation, all available energy goes towards crack extension. Common forms of energy dissipation in brittle material include:

#### Bridging

In the case of brittle materials, bridging occurs mainly when a particle of material dislodges in the wake of a crack, resulting in a contact point should the crack close. This changes the stress state at the crack tip, as the loading pivot point has shifted from the tip to the contact point. A different form of 'bridging' may occur where there is a tortuous crack path, with large angles of crack diversion. Upon further opening of the existing crack, some faces may remain in contact with each other, disspating energy in the form of friction/heat as the two sides displace. Figure 2.5 shows examples of both mechanisms described here.

#### Branching

This is where a propagating crack divides, resulting in the available energy being shared between multiple crack tips. Effectively, the propagation rate is divided by the number of branches stemming from one original crack. See Figure 2.6 for an example in cement mortar.

(a) 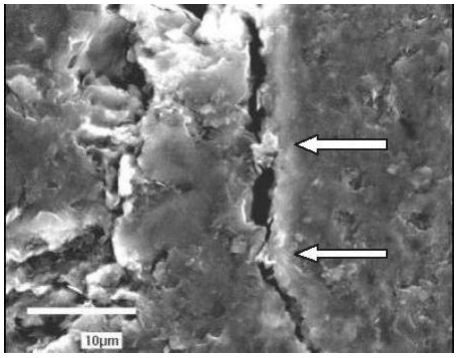

(b) 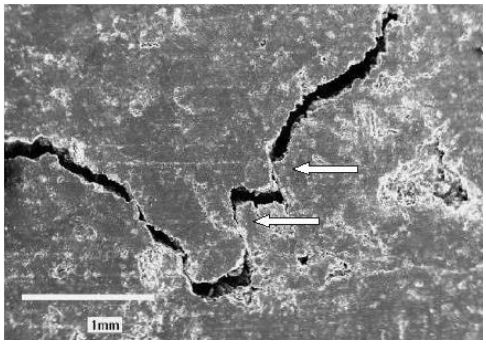


**Figure 2.5:** (a) Bridging particles in the wake of a crack. (b) Frictional contact points due to crack path tortuosity. [35]



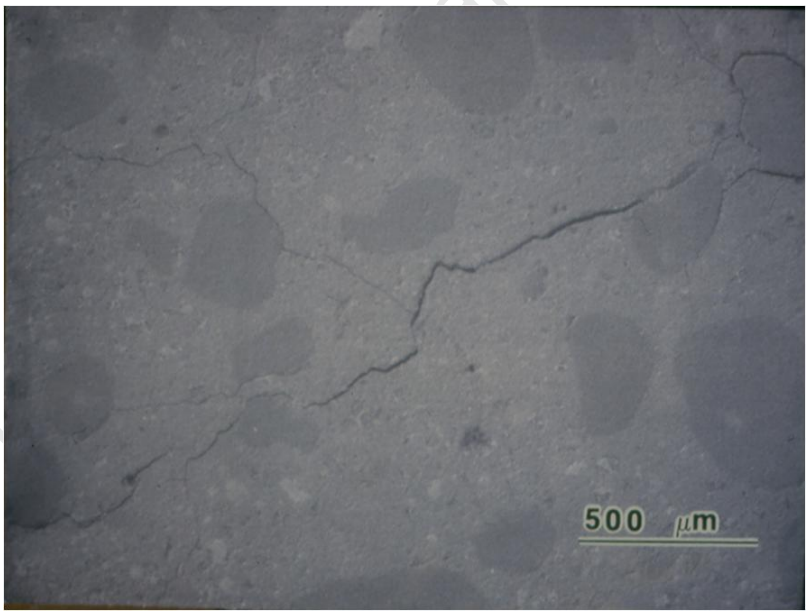


**Figure 2.6:** Crack branching. Note the single original crack growing from the right, branching out once in the middle of the image, and again on the lower branch. Evidence of crack jumping is also presented, to the lower left, where the crack seems to arrest and restart nearby. [50]

### Jumping

The appearance of jumping, seen in Figure 2.6 is characterised by the arrest and restart of a crack nearby. This is often caused by sub-surface continuation of the crack around embedded grains, which does not break the material on the surface. Another cause in polycrystalline brittle material may be the interaction of the applied stress field with the grain structure, causing cracks to initiate at new points of weakness which require less energy to propagate than a crack which exists in a local region of toughness.

### Tortuosity and Surface Roughness

Referring again to Figure 2.5(b), Crack diversion (at large angles) slows the rate at which a crack propagates from one face of a material to another. i.e. Where a given amount of energy would result in a crack propagating away from a surface for 2mm, a diversion could mean the crack tip ends up only 1mm away from the surface, in absolute terms. This can extend the life of a part, if a crack takes that much longer to propagate through the thickness, due to diversion.

A more common result, however, is that the direction of the crack runs more parallel to the direction of opening. This, together with the tortuous nature of the crack edges, results in a shear opening mode (mode II, Figure 2.2). The energy required for the crack to open in this fashion is higher than the frictionless tensile opening mode I, and overcoming this friction absorbs much of the applied energy which would otherwise be given over to crack propagation.

### Microcracking and Fracture Process Zone

Microcracks can contribute to toughening of a materal, despite also contributing to crack propagation. This happens if a given amount of energy is expended in the formation of multiple microcracks, as opposed to the propagation of a single main crack. Ortiz [28] described a situation in which microcracks form at available grain boundaries, until all available sites are cracked, whereby there is a net reduction in the local stiffness ahead of the crack tip. This increased compliance redistributes load, reducing the crack tip stress and slowing propagation. As such, materials which have a greater propensity for microcracking may experience an overall toughening effect, as opposed to materials which exhibit little microcracking behaviour.

Following on from this is the idea that the size of the process zone ahead of the main crack, i.e. the region of microcracking, must affect the toughening behaviour;

in a larger process zone, more microcracks can develop, and there is a greater capacity for energy dispersion. To restate in other words: the more nucleation sites a material has in the process zone, the more microcracks are able to develop. There will, however, be a critical microcrack density at which point other mechanisms of crack propagation take over, such as microcrack linking, etc. Therefore, the *larger* the process zone (in area terms), the more microcracks are able to develop before reaching that critical density, allowing more energy dispersion to take place. Becker, in experimental work on nuclear graphite, has confirmed this idea [5]. He discovered that different sample configurations of the same material give different fracture toughness values, and that this correlated to different sized process zones developing in the different geometries. Specimens which manifested smaller process zones gave smaller values for fracture toughness than those which developed larger process zones.

## 2.3 Factors Affecting Fracture Behaviour

The graphite used in a nuclear reactor is subject to many influences which change the behaviour of the material on both a nuclear and structural level, as mentioned in Section 1.2.4. This section covers some of the previous knowledge regarding crack behaviour in nuclear graphite. Some of the more important factors which must be considered when analysing nuclear graphite include: irradiation, oxidation, temperature, porosity and grain size, strain rate, and process zone. These are discussed in the following sections.

### 2.3.1 Irradiation

The main structural effect that neutron irradiation has on nuclear graphite is a volume change. This volume change is characterised by a shrinkage in the basal plane and an expansion in the perpendicular c-axis direction of the crystal lattice. This expansion is initially taken up by the pores and microcracks inherent in the graphite, and so there is first observed an overall shrinkage as the c-axis expansion is accommodated and the basal plane shrinkage is not. This also results in densification. Subject to further neutron irradiation, the pores will at some point not be able to accommodate any more expansion and an overall volume expansion is observed [4], as shown in the experiments conducted by Ishiyama *et al* (Figure 2.7) [34].

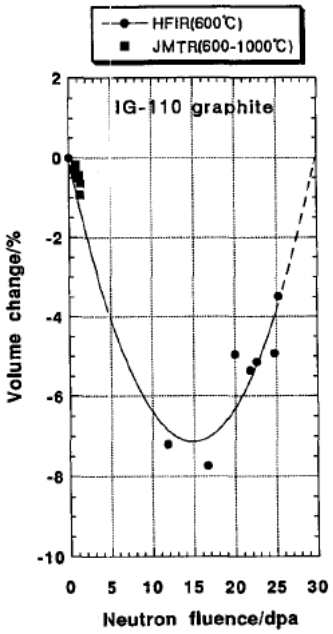


**Figure 2.7:** Effect of neutron fluence on graphite bulk volume [34]

The effect this has on the structure is to increase the level of internal stress experienced in the graphite, which raises its susceptibility to stress corrosion cracking. Young's modulus is also affected by this neutron irradiation, showing an increase at lower neutron doses before decreasing after turnaround. This eventual decrease has been attributed to microcracking associated with the induced volume expansion which is thought to occur between filler/binder interfaces [51]. Both of these effects are compounded with increasing temperatures, which will be discussed shortly.

### 2.3.2 Oxidation

Oxidation can be classed into two categories: thermal and radiolytic. It occurs primarily in $CO_2$ cooled reactors where the gas is decomposed either by the temperature or radiation into reactive species [4], which can contribute to slow crack damage. However, even in helium cooled reactors there is potential for oxidation damage as there exists a low level of impurities such as water vapour, carbon dioxide, carbon monoxide, hydrogen and methane [30, 31].

Oxidation produces molecules which react with the carbon in graphite to form carbon monoxide, breaking down the structure of the graphite blocks. The result is a more porous material, producing a decrease in both the bulk tensile strength and elastic modulus of the material [39]. These changes in turn affect crack propagation

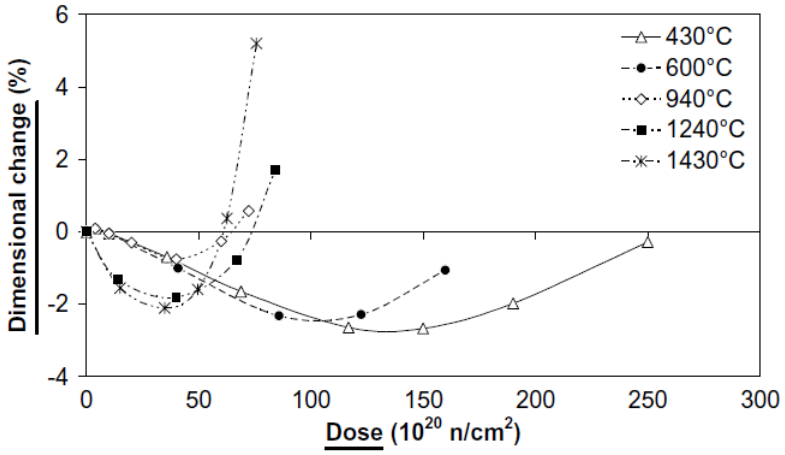


**Figure 2.8:** Volume change vs neutron fluence at different temperatures [51]

behaviour.

The thermal oxidation contribution to the total increases with temperature, discussed next, and it is reported to have a greater effect on the material properties. Its effect is highly dependent on temperature gradient, whereas radiolytic oxidation occurs uniformly throughout the material [39].

### 2.3.3 Temperature

Temperature, apart from its contribution to volume expansion of graphite, also has further reaching effects on the behaviour of the factors already mentioned, namely irradiation and oxidation, amongst others.

Hacker *et al* [32] conducted a study on two different moderator graphites in use, GCMB and PGA. They found that the isotropic GCMB (round filler particles) showed far more expansion under temperature than the anisotropic PGA (needle filler particles), although the coefficient of thermal expansion itself showed little variance over the temperature range $20° - 600°$C, and to levels of oxidation up to $50 - 60\%$.

With regards to irradiation, temperature has a contribution to the total expansion. This results in expansion at lower levels of irradiation with less shrinkage at increased temperature, and it also increases the rate of change of the volume and Young's modulus values. These effects are clearly shown in Figures 2.8 and 2.9, up to a temperature of 1430°C [51].

Oxidation occurs in three rate regimes, with temperature the influencing factor as to which regime is controlling the oxidation rate. These three regimes are the

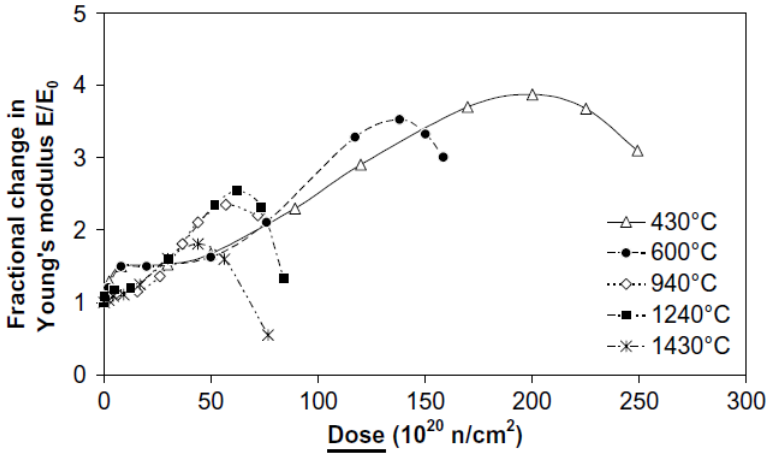


**Figure 2.9:** Young's modulus vs neutron dose at different temperatures [51]

chemical regime ($< 500$°C), the in-pore diffusion controlled regime ($500 - 900$°C), and the boundary layer controlled regime ($> 900$°C), although the temperatures given may differ slightly based on various conditions, such as flow rate. In the lower temperature region, the chemical reaction rate is slow and the gas has time to diffuse deep into the graphite, resulting in uniform oxidation. In the higher temperature regime, the reaction rate is so fast that there is no time for diffusion and the outer surface of the graphite is attacked, leaving the inside relatively untouched. The mid-temperature region is a combination of both, depending on the actual temperature. It may then be inferred that the higher temperatures result in a greater overall volume change, with rates that may be determined by experiment, as has been done by Xiaowei *et al* [31].

### 2.3.4 Porosity and Grain Size

The size and nature of the pores in a particular grade of nuclear graphite, as well as the overall percentage of porosity in a structure made from such a grade, has been shown to have a large impact on the cracking behaviour observed in nuclear graphite.

Burchell [42] discusses in his well-known work how the shape of pores, related to the manufacturing process, may increase the level of cracking found in a graphite specimen. Needle-shaped pores, which are associated with extrusion methods and may be compared to microcracks (see Section 2.2.2), provide sites of larger stress concentration from which cracks may initiate. These stress raising sites may also serve to draw existing cracks, serving to bridge and elongate a growing crack. How-

ever, Burchell also makes the comment that these same type of pores may arrest crack growth if oriented or located in an unfavourable manner.

Ortiz [28] adds to the study with his analytical approach to microcracking in brittle materials, and concludes that the grain size of the material has a large effect on whether the overall effect of microcracking is toughening, or embrittlement. He states that the model he developed shows that in material with a smaller average grain size, which exhibits less microcracking, the effect is one of net toughening, whereas materials with a larger average grain size experience net embrittlement. This may seem to disagree with the idea mentioned in Section 2.2.2, where it was put forward that more microcracking made for tougher material. However, the toughening mechanism mentioned therein applies only up to a certain level of microcracking, a critical level, before the material is weakened sufficiently for macrocracks to propagate. The effects mentioned in this paragraph are assuming this critical level is surpassed.

Ouagne *et al* [35] performed a study on two grades of nuclear graphite: a coarser structured PGA grade (grain size of "several millimetres" [35]), and a relatively finer IM1-24 grade (grain size ~0.5mm [35]). Their results for the Linear Elastic Fracture Mechanics parameters show that the PGA graphite exhibits a lower fracture toughness ($K_{\mathrm{Ic}}$) than the IM1-24, which is in agreement with the conclusions of Ortiz, mentioned above. The results also show that despite the decreased fracture toughness, the coarser grade graphite developed a higher "work-of-fracture", meaning the energy used to propagate a crack in the material was higher than in the finer grade graphite. This they attribute to a higher degree of irreversible energy dissipation processes (e.g. micro-cracking), in the coarser material, which is also in agreement with the findings made by Ortiz.



### 2.3.5 Strain Rate

The effect has been seen in previous experiments of crack propagation in brittle materials which exhibits intergranular behaviour at low loading rates, which then switches to transgranular behaviour at higher loading rates [52]. This is in agreement with the observation that intergranular cracking is a lower energy mode of crack propagation. What is interesting is that this phenomenon can be seen in instances where the loading rate does not change, as in Tait's experiments with cement mortar, shown in Figure 2.10.

In these experiments, where load was applied under double torsion, the load was increased in order to propagate the crack, but loading *rate* was kept constant, in

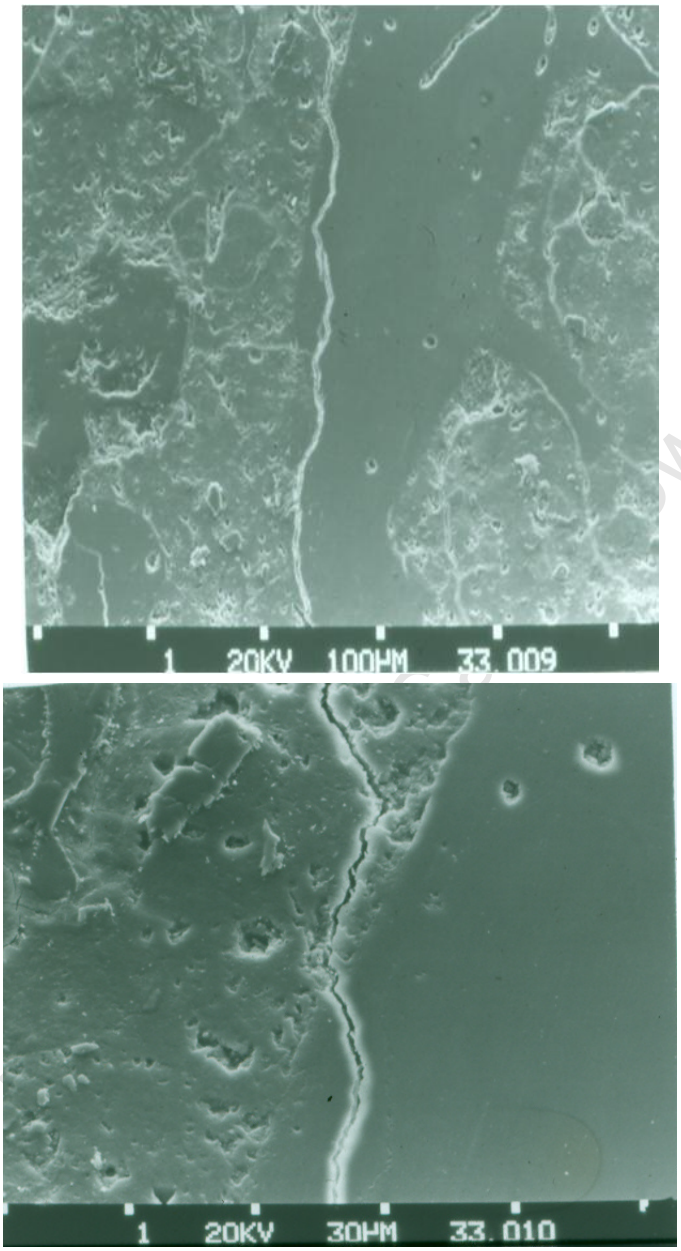


**Figure 2.10:** Image of a crack propagating upwards along a grain boundary in cement mortar, then jumping the boundary with no increase in loading rate. This test was performed using the double torsion configuration. [50]

line with the conventional DT method put forth by Evans [53]. In the DT method, an increase in load increases the stress intensity factor associated with a crack tip, and under that method, it is the *only* variable that affects the stress intensity during a test. This suggests that a better way to characterise the jump from inter- to trangranular behaviour is in terms of all forms of energy available to the crack, as opposed to just the strain rate. In the case of certain specimens, they amount to the same effect, but from the DT experiments, it is clearly not specifically strain rate that is the direct cause of the change in behaviour.

The previous sections show the many different factors that have an effect on the fracture behaviour of brittle materials in general, and nuclear graphite in particular. It is therefore seen as a necessity that there is a technique with which to examine the actual effect of these factors on the loading response in graphite.

The miniaturised Double Torsion method proposed in this project is seen as an elegant solution, in that loading studies may be performed *in situ* inside a scanning electron microscope, and the response of the microstructure directly observed. A particularly attractive feature is that the effect of some of the factors mentioned above may be observed in a single test via the 'changeover' method used in previous work by Tait & Garrett [26], where environmental properties are changed during an experiment on a single specimen. Used by Tait & Garrett to quantify a change in v-K behaviour, it may also be used in a more qualitative sense by noting any changes in crack propagation behaviour on SEM micrographs. This method would be suitable for reproducing factors such as temperature change, strain rate change, environmental effects (depending on the SEM being used), and also simulation of neutron irradiation by electron irradiation using the SEM electron beam.

The following chapter provides background on the DT method, as well as other experimental considerations in this project, namely the SEM environment and factors involved in miniaturising a technology such as this.

# Chapter 3

# Topics of Experimental Relevance

This chapter provides background into the various experimental concepts that are involved in the current work. A review of the double torsion method is provided so as to familiarise the reader with the particular methods of analysing the specimen, as well as the considerations attached to such an analysis. An understanding of these was required in order to design a rig which would adequately accommodate such considerations. Further to this project, an understanding of the requirements of designing a fracture mechanics rig for use *in situ* inside a scanning electron microscope (SEM) was required, and a breakdown of these requirements is presented, as well as various solutions from literature.



## 3.1 The Double Torsion Method

### 3.1.1 What is Double Torsion?

The Double Torsion (DT) method is a fracture mechanics method involving the double torsion specimen, which is a rectangular specimen loaded in four point bending on one short end. This bending configuration has the effect of placing the rest of the specimen, that lying behind the loading points, in torsion. A simple representation is shown in Figure 3.1.

The basic principle of the DT specimen is that it operates as two independent bars being simultaneously twisted, while being partially connected to each other. A crack propagates down the centre of the specimen, separating the two torsional ligaments. If ones recalls from basic mechanics of solids theory that the torsion present in a beam is constant along its length, one can understand how the applied stress would remain constant for the length of the specimen. This explanation does

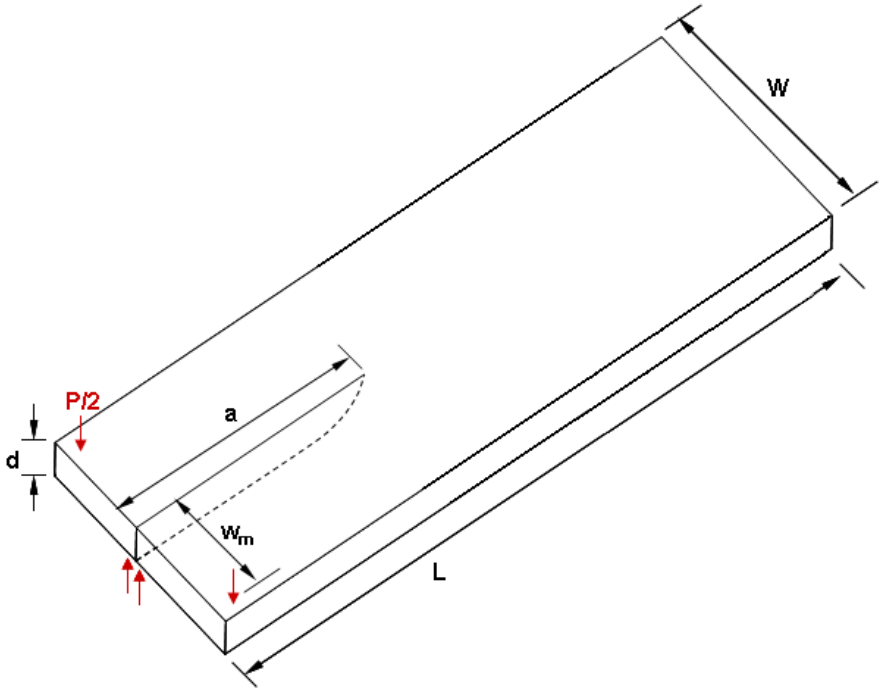


**Figure 3.1:** Double torsion specimen geometry dimensions and loading points

however have a certain reliance on some assumptions, and these will be discussed later in Section 3.1.4.

To place a certain amount of context, other better known fracture mechanics specimens include the compact tension (CT) and single edge notched bend (SENB) specimens, shown in Figure 3.2. The CT specimen places a combined tensile and bending load over a propagating crack, while the SENB specimen places a bending load across a propagating crack.

The two well-known specimens, the CT and SENB specimens, are used to investigate cracking behaviour in especially ductile materials. Fatigue is one such mechanism by which cracks propagate, and subjecting these specimens to fatigue type loading allows one to observe the behaviour of the resulting crack, as the small incremental crack growth per cycle is stable. As explained in Section 2, in these specimens, both the stress and the amount of incremental crack growth per load cycle increases with an increase in crack length, until the critical combination of stress and flaw size is reached, whenceforth fast fracture occurs.

Brittle materials, however, are less likely to exhibit stable cracking under load. The fracture toughness of brittle materials such as graphite or other ceramics is low compared to that of ductile materials such as mild steel, or aluminium. It is therefore difficult to gain a significant amount of data relating to the crack growth behaviour

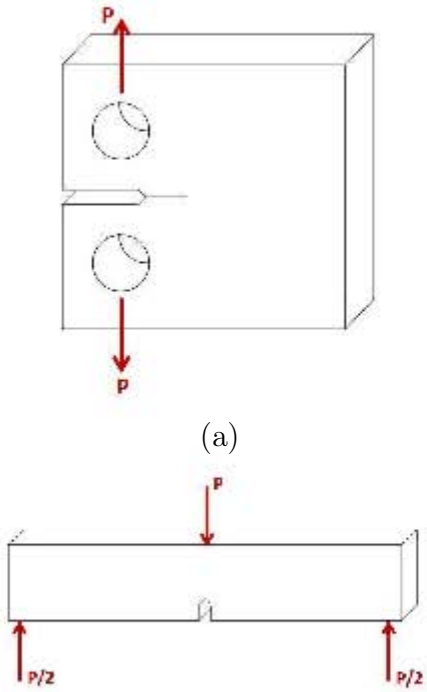


**Figure 3.2:** (a) Compact tension and (b) single edge notched bend specimens

of the material when using specimen configurations such as those mentioned above. Attempts to generate slow crack data such as v-K curves (Figure 2.4) are fraught by the fact that only a small cracked length may be observed before the increasing crack length dependent stress intensity reaches the low critical fracture toughness value, upon which the specimen cracks through uncontrollably and no data may be gathered. Previously, researchers have attempted to circumvent this issue in graphite by sandwiching a SENB specimen between two steel plates, in an attempt to more evenly control the stress distribution surrounding the specimen notch tip [37]. This method was met with some success in determining the fracture toughness, but issues surrounding the contact between the plates and the test specimen were identified by the authors. This, as well as the fact that a stress intensity correction for the plates had to be determined by finite element analysis, suggests that a different geometry might provide for a simpler experimental procedure.

The DT specimen offers a solution to these problems, as it purports to present a region of crack length *independent* stress intensity along its length, as opposed to the dependence suggested by Equation 2.5, even though mode I stress intensity is still assumed for this specimen. In the independent region, the stress intensity is assumed to be purely reliant on the dimensions of the specimen, and the applied

load. As will be discussed later, it is because of this factor that crack growth may be induced at a controlled rate in the specimen by incremental variation of applied load only. This is highly advantageous as it allows both the quantitative determination of fracture behaviour in brittle materials, as well as direct observation of the crack growth, along with its associated mechanisms of propagation. This would not be possible with a specimen with a higher, uncontrollable propagation rate.

### 3.1.2 Previous Double Torsion Research

The DT method was introduced in 1966 and 1969 independently by Gerry [6], and Kies and Clark [7], but was developed into its current recognizable form by Evans and colleagues [53]. It has since been reviewed by many authors [11, 13, 53, 54, 55], with corrections being suggested where certain assumptions were found to be lacking [8, 53, 56, 57, 58]. Despite this, the method has to date not been standardized, although there is a large body of literature regarding the dimensions and methodology which give suitable results. These will be discussed more fully under subsequent headings.

Although there are a number of reviews of this method in the literature, three main works were examined here in order to gauge the progress of the method over the four decades since its conception. The first was an evaluations and review by Tait, Fry & Garrett in 1987 [11], whose review was based on literature as well as experiential evidence. They made a number of recommendations concerning the most useful specimen ratios, the use of grooves to guide straight crack growth, and the importance of specimen and loading point alignment.

The second review was done by Shyam & Lara-Curzio in 2006 [54], and was purely based on available literature. While the recommendations based on this review did not deviate from those given by Tait *et al* in their paper, there was additional information presented about corrections which had been suggested in the intervening time between the two reviews, although the authors did not make any conclusions about these corrections or their effect on the method.

Perhaps the most comprehensive review work seen to date is the evaluation and review by Becker, Marrow and Tait in 2010 [13]. In this paper the authors evaluate the assumptions, identified issues, and proposed corrections from previous years through a combination of experimentation, finite element analyses, and observations by means of digital image correlation. Their conclusions about the method suggest that a small amount of work is yet needed before the method is standardized, but provides valid suggestions for doing so.

The three works identified here are by no means the extent of the review work

that has been done on this method; these papers were, however, selected for their broadness and representivity of the state of the method at their given points in time.

### 3.1.3 DT Specimen Analysis

The reader is referred again to Figure 3.1. As mentioned in the previous section, the double torsion specimen may be regarded as a rectangular beam loaded in four point bending at one of short sides, over a starter notch. The complementary loads on either side of the notch serve to 'twist' each half, applying a torsional load through the independent ligaments. This torsion in each half in turn results in a tensile load (mode I) at the notch end on one of the faces of the specimen, with the opposing face in complementary compression. This tensile load is purely dependent on the torsion being passed through each independent beam, and as torsion is constant along a beam, the tensile load is reliant only on the twisting load applied at the front of the specimen, and not on the propagating crack length.

In order to gain an expression for stress intensity for the DT specimen, Evans took the linear elastic relationship between stress intensity and strain energy release rate, $G$:

$$K = \sqrt{EG}$$

and defined $G$ over the cracked area to gain:

$$\begin{aligned} G &= -\frac{dU}{dA} \\ &= \frac{P^2}{2d}\frac{dC}{da} \\ &= \frac{w_m^2 P^2}{2\mu W d^4 \psi} \end{aligned} \tag{3.1}$$

The classical relation between stress intensity and applied load, formulated by Evans [53], is hence presented both for the plane strain and plane stress cases:

$$K_{\mathrm{I}} = P\sqrt{\frac{3w_m^2}{Wd^4(1-\nu)\psi(d,W)}} \tag{3.2}$$

$$K_{\mathrm{I}} = P\sqrt{\frac{3w_m^2(1+\nu)}{Wd^4\psi(d,W)}} \tag{3.3}$$

Where:

$K_{\mathrm{I}}$ is the mode I stress intensity factor;

$P$ is the applied load;

$w_m$ is the moment arm from the centre of the specimen notch to the load application point (see Figure 3.1);

$W$, $d$ are specimen dimensions as shown in Figure 3.1;

$\nu$ is the Poisson's ratio of the specimen material; and

$\psi$ is a thickness correction factor (added subsequent to Evans' work, but considered essential - discussed later).

Note the absence of the crack length, $a$, in the above expressions; this gives the crack length independent stress intensity. However, an important concept in DT analysis is that of the specimen compliance. It was said previously that the *resultant load* at the crack tip was reliant only upon the applied load, and not the crack length. While this is true, the phenomenon of compliance means that the *applied load* at the crack tip is a function of crack length. As a crack propagates along the specimen for a given applied load $P$, the stiffness in each specimen arm decreases as the arms become longer. Due to this relaxation, the applied load becomes less, resulting in a differential quantity, $\frac{dP}{dt}$, which is related to the velocity, $\frac{da}{dt}$, at which the crack propagates. This is useful in slow crack growth investigations, when one cannot measure the crack velocity, but can measure the load output of the system. The two quantities are related through an assumed linear crack length $a$ vs compliance $C$ calibration curve which should be generated for any new material being investigated through this method.

An important point to note is that Equations 3.2 and 3.3 are only valid within a certain region of the specimen; that is, they are valid along a percentage of the crack path, corresponding to the middle portion of the specimen. A common generalization is to say that the middle half of the specimen exhibits the crack length independent stress intensity described by the equations [11]. Figure 3.3 shows the deviation from independence for the length of the specimen. Higher values occuring near the beginning of the specimen are attributed to the crack front having not fully conformed to its distinct curvilinear profile yet, while weakness of the decreasing ligament thickness is regarded as responsible for lower values near the end of the specimen [11, 13]. Both of these effects stem from the crack not having a uniform profile and through the complete material thickness.

Aside from the distance along the crack path, validity of the data is also governed by the skewness of the propagated crack, designated by $a_{off}$, the distance a crack deviates from the centreline of the specimen. With an increase in $a_{off}$, one arm of the specimen becomes narrower than the other, and therefore less stiff. This further turns the crack towards the narrower arm. The result is that this one arm

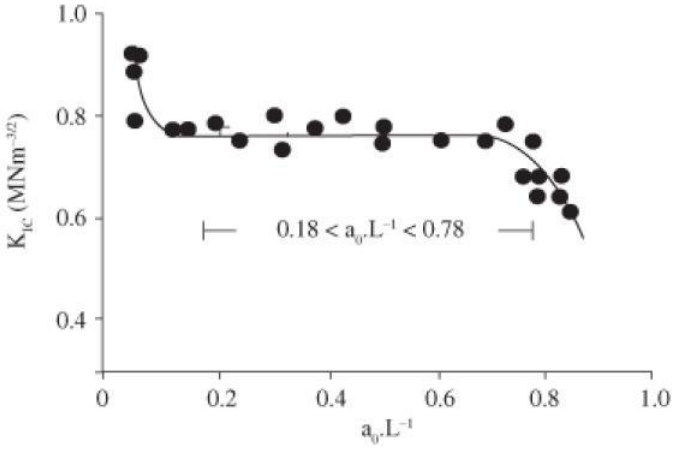


**Figure 3.3:** Stress intensity profile along the length of a DT specimen. This particular data set is from tests performed in toluene on soda-lime-silicate glass slides [59].

is less resistant to cracking than the thicker arm, and decreases the specimen's overall resistance to applied stress intensity, producing erroneous v-K results. The recommended allowable deviation of a crack tip for Equations 3.2 and 3.3 to remain valid is $a_{off} < {}^{W}/_{8}$ [13], and this condition applies to the relevant portion of the specimen, namely the middle third. It should be noted that as fracture toughness tests are conducted at only one point in the specimen, and the result is determined from the highest load recorded, the deviation does not affect these tests as much as it does v-K data.

#### 3.1.3.1 Generating Slow Crack Data

There are three methods for generating slow crack/v-K data in a double torsion specimen, each with its own advantages and disadvantages. It is therefore left to the researcher to decide which method best suits his/her application. Two of the methods rely on the aforementioned compliance calibration curve which takes the form:

$$C(a) = \frac{y}{P} = Ba + D \tag{3.4}$$

Where $B$ and $D$ refer to the slope and intercept, respectively, of the linear calibration relationship. These are constants, independent of $a$ for a large part of the relationship. It has been assumed in the past that the value of $D$ is negligible, as the compliance in a specimen with no crack should, theoretically, be zero. However, in Becker's work on the DT method, this value was shown to be a considerable fraction of the slope value, $B$, indicating that the specimens testing were not completely

stiff, and could deform somewhat before crack growth commenced [13]. It therefore cannot be ignored, and must be accounted for via initial compliance-crack length determination. The additional relation to crosshead displacement $y$ and applied load $P$ may be used to determine crack length without needing to directly observe the crack.

### Load Relaxation Method

This method works on the principle that if one loads a specimen to a particular value, $P_i$, and then halts the loading process, any subsequent decrease in applied load must be, through compliance, a direct result of crack extension in the specimen. The relationship between crack velocity, $v$, and the loading conditions is expressed through the following relationship:

$$v = \frac{-P_i}{P^2}\left(a_i + \frac{D}{B}\right)\frac{dP}{dt} \tag{3.5}$$

Where:

$P_i$ is the original load value applied;

$P$ is the instantaneous load at any point in time after the halting of the machine crosshead;

$a_i$is the crack length at the start of the relaxation process, i.e. at peak load $P$;

$D$, $B$ are the compliance constants referred to in Equation 3.4.

Note that this technique requires knowledge of the crack length $a_i$, which may be directly measured, or gained from the compliance relationship. This method is advantageous in that the entire v-K curve can be generated in a single experiment, although this is subject to some limitations, a significant one being that machine load cell compliance is coupled with the result. This can be accounted for, though, by generating a compliance relationship based on the *combination* of load cell and material, as opposed to just material compliance alone. It would require compliance test results to be obtained using the actual loading setup to be used for material testing, as opposed to using a different machine/load cell combination to attain this relationship. A further reported limitation is that this technique is generally only suitable for high loading or crack growth rates, as for slower rates there is a temperature effect on loading [54]. It seems to this author, however, that any slow crack growth rate would be affected by a significant temperature change, as the material properties shift accordingly, and this effect should not be limited to this method only.

### Constant Load Technique

This technique operates on the fact that for a particular constant applied load there will be a distinct constant resultant velocity. That average velocity, however, needs to be determined visually by measuring a change in crack length over time. The advantages of this system include the fact that load cell compliance is automatically accounted for, and it is suitable for slow crack growth rates. However, there is a limitation in the responsiveness of the loading system; one would need a high feedback rate between the load reading and load application devices. The main disadvantage though is that only one data point on the v-K curve can be obtained. It has been suggested that either this or the following method, which share the aforementioned disadvantage, be used in conjunction with the Load Relaxation Method in order to verify that method's results. i.e. One can generate the entire v-K curve using load relaxation, but the curve should be verified in certain places by the use of a complimentary method such as the constant load technique [54].

### Constant Displacement Technique

In this technique, the crosshead is lowered at a constant displacement rate. As this happens, the crack velocity increases until it is such that any further increase in load is exactly balanced by the increase in compliance from the lengthening crack. i.e. The rate of loading and the rate of compliance increase are equal. This is exhibited by a "plateau" of the load-displacement plot, at which point the crack velocity can be determined using Equation 3.6:

$$\frac{d\triangle}{dt} = BPv \tag{3.6}$$

Where:
$\frac{d\triangle}{dt}$ is the crosshead displacement rate;
$B$ is the slope constant from the compliance relation;
$P$ is the value of the load "plateau", and
$v$ is the attribute crack velocity.

Again, only one data point on the v-K curve can be obtained, however this method is still slightly simpler than the constant load technique in that crack length measurement is not required in order to determine the velocity. This makes it the method best suited for application in an environment where crack length is not easily measured, e.g. with opaque materials, or inside a SEM. A combination of this technique and the load relaxation technique has been developed, which allows

one to generate a portion of the v-K curve with one test. In this version, a load relaxation test is carried out immediately following a constant displacement test, using the load plateau value as the initial relaxation load.

#### 3.1.3.2 Generating Fracture Toughness and Fatigue Data

Generating fracture toughness data is simply achieved by applying load at a high rate to a pre-cracked specimen, and measuring the load at which the specimen fractures. One can repeat this a few times at ever higher loading rates, until it can safely be determined that the fracture load does not change significantly with loading rate. Referring back to Figure 2.4, achieving this condition would signify having reached the rightmost asymptote of the v-K curve, the fracture toughness. It is necessary for this method to be able to deliver a suitably high loading rate. Care should be taken to ensure the specimen is sufficiently pre-cracked, as during the pre-cracking stage the crack front has not fully developed, and the through-cracked area at this time will not be constant for a given change in crack length. i.e. $dA$ will continue to change for a given $da$ before pre-cracking has finished.

Tait *et al* [11] commented that it is possible to conduct fatigue tests using the DT technique, but there is a need again for a highly responsive feedback and loading system. If the cyclic frequency is high enough, there is no need to analyse the fatigue case with respect to load relaxation or compliance, as the primary mechanism of crack growth in this case is now fatigue as opposed to slow crack growth. In Section 2.1.2 it is stated that crack growth is governed by either or both mechanisms, and this ratio is governed by the combination of material and loading conditions. For a high enough frequency of loading, one would work out $\triangle K$ from the load amplitude $\triangle P$ using Equation 3.2 or 3.3 as appropriate. Depending on the material and the rate of relaxation in the system, however, lower frequencies could be affected by undesired behaviour in the applied load pattern. Care should be taken to analyse the load behaviour of a DT system at lower frequencies before undertaking such experiments.

### 3.1.4 Assumptions and Corrections

There are various assumptions which are made about the behaviour of the specimen when using the Double Torsion method, some referred to already. These assumptions are used in the derivation of the stress intensity equations 3.2 and 3.3. Many of these assumptions are only valid within a certain range, and some require results gained from the DT technique to be analysed with correction factors in order to remain

true. The assumptions are presented here, with a comment as to the validity of the assumption with reference to current knowledge.

- **The two cracked halves are independent and do not interact with each other in any way**: This assumption only holds true for thinner specimens. For most specimens, though, there is a degree of interaction between the two halves on the compressive face, which increases the thicker the specimen. The introduction of a groove on the compressive face in order to alleviate this effect was commented on by Tait *et al* [11], but for numerous reasons the use of grooves for any reason has been consistently discouraged in DT reviews to date [11, 13, 54]. Fuller [55] suggested a correction factor to account for the interaction, which is expounded on in the next section.

- **Only the cracked arms deform under loading, i.e. there is no other deformation of the specimen in the uncracked region**: The analysis of the DT specimen assumes that there is pure torsional deformation of the cracked arms, and that the rest of the specimen does not displace or deform in any way. Following from this is the conclusion that any increase in compliance must be entirely due to crack growth. This assumption has recently been proved incorrect by Becker *et al* [13], whose experimental work with digital image correlation shows distinct out-of-plane displacements of the uncracked portion of a brittle graphite specimen. This suggests a contribution to specimen compliance by the uncracked portion, contrary to the assumption used in the derivation of the velocity relations given in Section 3.1.3.

- **Any increase in compliance is entirely due to crack growth**: It was discussed previously that out-of-plane deformation of the uncracked portion of the specimen contributes to specimen compliance, so for that reason alone this assumption is rendered invalid. Further to this however, the actual machine setup has a measure of compliance, and this does contribute as well to the overall compliance exhibited during testing. The implication of this is that velocity equations which are dependent on a compliance term need to have a correction imposed to account for the effect of machine relaxation and specimen deformation.

- **The compliance-crack length relationship is linear**: The importance of this assumed linearity is that the crack length independent stress intensity relationship is formulated on this assumption [13], and it is based on the previous two assumptions mentioned - all compliance change must come from

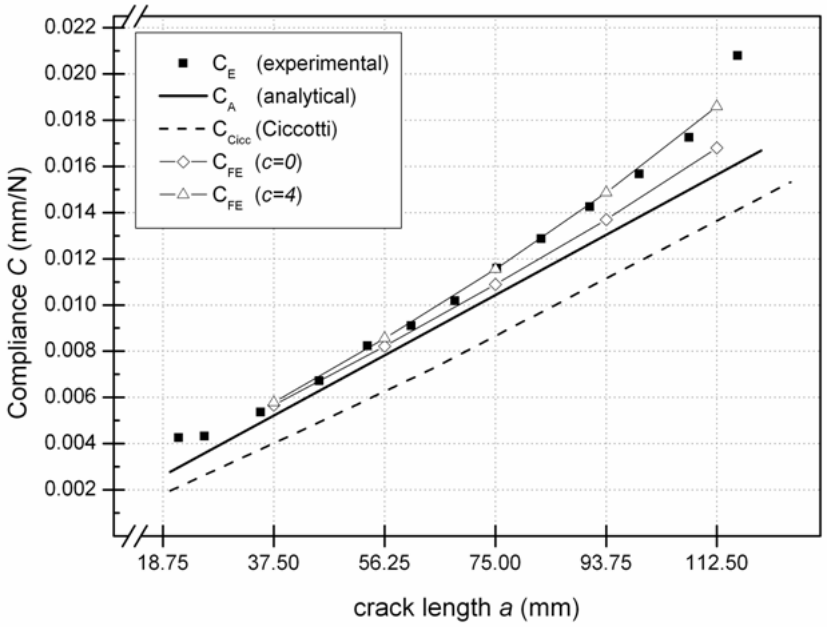


**Figure 3.4:** Compliance-crack length relationship for PMMA specimens from experiments conducted by Becker. That work also examined the effect of various proposed corrections to Evans' conventional methodology, which aimed to provide a linear relationship [13].



crack extension, and all deformation is due to rotation of the cracked arms. Reasons for the deviation from linearity near the beginning and end of the specimens have already been discussed, but concerns have been reported by a number of researchers that there is a more pronounced dependence of the stress intensity relationship on crack length, which calls further into question the linearity assumption. Ciccotti *et al*, for example, reported as much as a 40% experimental deviation from the value of $G$ given by Evans' analytical solution, and they attribute this to the non-linearity of the compliance relationship [58]. Figure 3.4, from compliance tests conducted by Becker on PMMA specimens, show an upward curve in the compliance - crack length relationship. These results are consistent between experimental and FE results [13].

- **The moment arm, $w_m$, remains constant**: The moment arm is defined as the distance between the advancing crack tip and the point of applied loading and, from the original definition of strain energy release rate given in Equation 3.1, is assumed to be constant throughout. This is necessary in order to maintain the crack length independent stress intensity formula. This is not

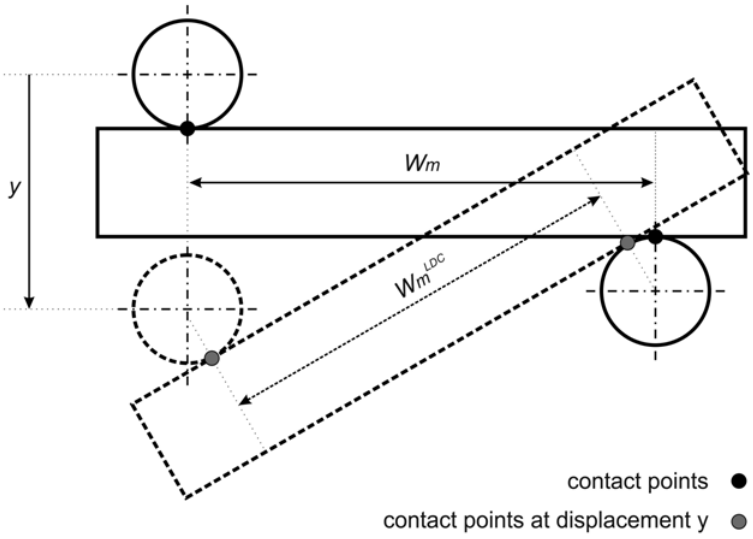


**Figure 3.5:** Moment arm decrease as the specimen deforms under loading. Reprinted from [13]



true, however, as this moment arm distance decreases as the specimen arms rotate downwards. This behaviour is illustrated in Figure 3.5. This decrease cannot be assumed to be small, with Becker *et al* reporting a 1.5mm change in a 4mm thick specimen [13]. The effect of this decrease has been shown to be substantial, with a possible error of up to 25% being introduced in the $K_{\mathrm{I}}$ value. Leevers [57] suggested a correction for this large deflection, which Becker *et al* have concluded is essential in order to correct the error value quoted above [13].

- **The fracture mode is pure Mode I**: There has been commentary in the past that this assumption is incorrect in that there might be a mode III contribution to stress at the crack tip. Tait *et al* [11] recommended that the assumption may be treated as valid providing the material in question had a suitably high mode III fracture toughness. Remaining with Becker's work, a finite element analysis was done which was shown to correlate well with experimental data. This analysis was probed for the stress states at the crack tip, and revealed that there is a mode III contribution to the overall stress in this region, but that the ratio of this contribution to that of mode I loading was approximately 2% [13].

- **Fracture is in plane strain**: This assumption has not been tested or val-

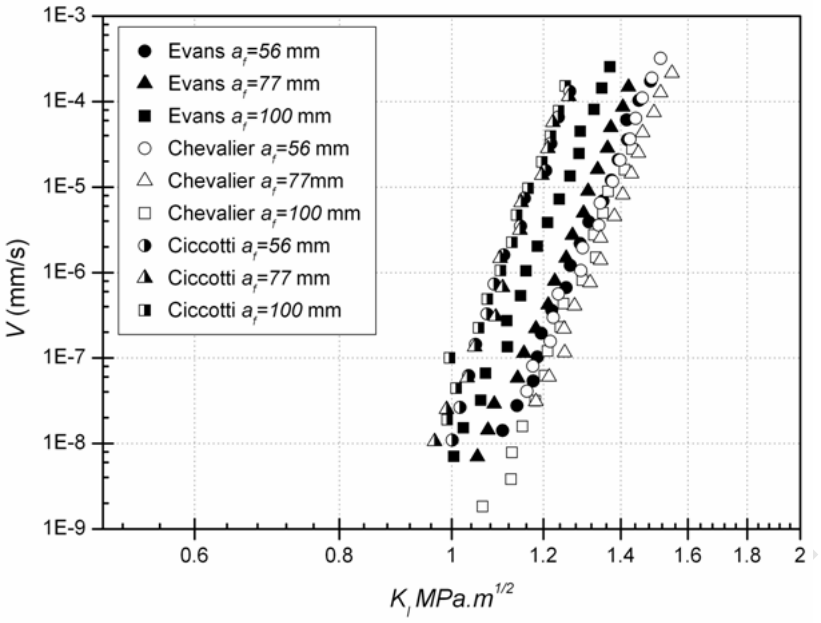


**Figure 3.6:** v-K data generated at different crack lengths in PMMA by Becker *et al.* Note the clear shift in the curve between different starting crack lengths for the classic Evans solution. [13]

idated to date. Previously, it was justified with the use of brittle materials, as they do not deform enough to produce a plane strain effect. It has been reported though that researchers have started using the plane strain case in some instances [54]. For the current work it is deemed the accepted practice should remain, and stress intensity will be analysed according to the plane strain case.

Due to the fact that many of the above assumptions are, for practical purposes, invalid, the crack length independence of the stress intensity factor of the double torsion specimen is called into question. The dependence can be seen in graphs of v-K data undertaken at different crack lengths, such as in Figure 3.6. Theoretically, if the relationship between the two values were truly independent, one could generate points on a v-K curve starting with any crack length, but Figure 3.6 shows that this does not happen. The factors which are thought to contribute the most are the shortening of the moment arm, the fact that not all compliance is due to crack growth, and the fact that the relationship between crack length and compliance is not linear.

There have been a number of proposed corrections in order to induce an independent relationship between the two values. Two oft-reported corrections by

Chevalier and co-workers [8], and Ciccotti and co-workers [58], both aim to provide independence by adding a factor to the compliance relationship which accounts for the non-linearity present. It should be noted that, necessarily, these factors all require knowledge of the crack length which is independent from the compliance relationship. Becker investigated the effect of these corrections, and concluded that for the purposes of generating v-K curves, only Chevalier's correction showed good reproducability, even though both corrections produced a crack length independent SIF relationship [13].

A further interesting comment made by Becker *et al* was that the effect of the deformation of the unbroken portion of the specimen was to deflect the 'linear' compliance curve upwards at larger crack lengths, whereas the effect of the moment arm decrease was to deflect the curve downwards. The authors suggest the two effects could be paired to cancel each other out in a specimen with optimal dimensions, to which they recommend proportions according to the $d : W : L$ ratio of DT specimens to be $3W : W : 0.08W$ as an initial estimate [13]. The next section describes geometry effects in more detail.



### 3.1.5 Specimen Geometry

Dimensions commonly used in literature, and recommended by Tait *et al* [11], are for specimen ratios of $1/6 - 1/15 : 1 : 3$. There are a few reasons for this. With regard to the length of the specimen, it has been reported that there is only a region of independent stress intensity along its length. Tait *et al* suggest this region is between $5 - 85\%$ of the length of a specimen with a width to length ratio of $1 : 3$, with this region decreasing for specimens with a small ratio, i.e. 'stubbier' specimens. Shyam & Lara-Curzio agree with this trend, although their review suggests that only about 60% of a 1:3 specimen is crack length independent, with a 1:2 specimen exhibiting independence along only 40% of its length [54].

The thickness however, is reported to have a greater effect on the applicability of Evans' classic equations. The essential problem is that, as discussed earlier, the two independent halves of the specimen may interact on the compressive side of the specimen. This would have an effect on the stress intensity produced throughout the specimen, and to account for this, there is a thickness correction factor, $\psi$, suggested by Fuller [55] which is automatically included in the classical expressions for stress intensity (Equations 3.2 and 3.3). The value for $\psi$ is given by:

$$\psi(d, W) = 1 - 0.6302\tau + 1.2\tau \cdot e^{-\pi/\tau} \tag{3.7}$$

Where:

$\tau = \frac{2d}{W}$, and

$d$, $W$ are specimen dimensions as shown in Figure 3.1. Tait *et al* state that this factor becomes more significant for thicker specimens, with Shyam & Lara-Curzio reporting that a thickness of more than $W/6$ presents distinct problems in this regard [11, 54]. The validity of this thickness correction factor is reported by Becker *et al*, who comment on work done in glass ceramics [13].

A further thickness consideration is raised by Albuquerque and Rodrigues [60], who tested the effect on various fracture properties of specimen thickness in relation to average material grain size. Their thickness to grain size ratios under consideration were 3:1 and 5:1. They concluded that the thinner specimens produced valid results for certain behaviour, namely R-curve *shape*, compliance curves, critical crack length, and load vs displacement curves. However, R-curve *values* and work-of-fracture values showed a thickness dependency.

Becker *et al*'s comments on thickness have already been touched on. Further to this it should be mentioned that they found that thinner specimens produced more reliable behaviour, as in the following cases:

- Non-linearity of the compliance relationship at larger crack lengths proved more pronounced in thicker specimens, which followed on to produce a greater dependence on crack length of the stress intensity factor, $K$;
- Thicker specimens showed greater out-of-plane deformations, again negating the compliance linearity;
- Uncorrected thicker specimens showed greater scatter in the v-K results, although it was found that this could be corrected via Chevalier's correction;
- Thicker and 'stubbier' specimens showed greater deviation in stress intensity values for a given applied load [13].

The research mentioned shows the importance of attempting to balance the dimensions of the DT specimen in order to achieve the least variance in stress intensity results. As reported above, there is possibly an optimum specimen dimension that could cancel the effects of the various sources of error, but this should be investigated in a dedicated parameter-variation experiment. In the absence of such understanding it suffices to say that specimens should be kept as close to a $3W : W$ relationship, with a thickness in line with the recommendations above, while also taking cognisance of the grain size of the material in question.

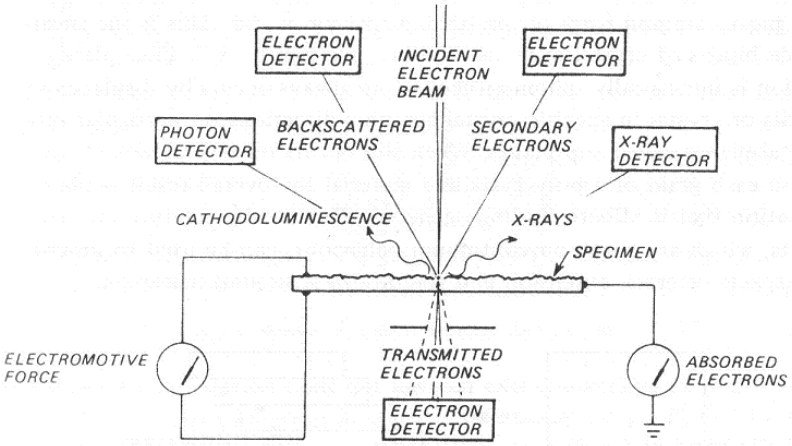


**Figure 3.7:** Various signals emitted from a sample undergoing electron impingement [27]

Now that there is an understanding of the theory of the DT specimen, the following sections focus on the more practical aspects of using the DT method inside a scanning electron microscope. There is however, a need for a description of the principles by which the scanning electron microscope operates, and the next section covers this briefly.

## 3.2 The Scanning Electron Microscope

The scanning electron microscope (SEM) may be compared to a regular optical microscope, but differs in that the mechanism of image transmission is electron reflection, as opposed to light reflection. The main working principle is that electrons are tunneled towards the specimen in question via an electron beam; a portion of electrons escapes through the material to earth, while another portion reflects off the material and is picked up by a 'backscatter' electron detector (as in the case of the optical microscope, where the human eye or camera is the light detector), while yet another portion impinges on the material, displacing existing material electrons, which then emit various forms of radiation which are picked up by other detectors. The signals from these detectors are processed to form a digital image based on the density and energy of scattered electrons. Figure 3.7 shows a diagram of the types of radiation signals that are emitted from a material being impinged upon by electrons.

The fact that the image is formed based on electron activity on the specimen is suggestive of the need for a specimen to be conductive. Non-conductive specimens do

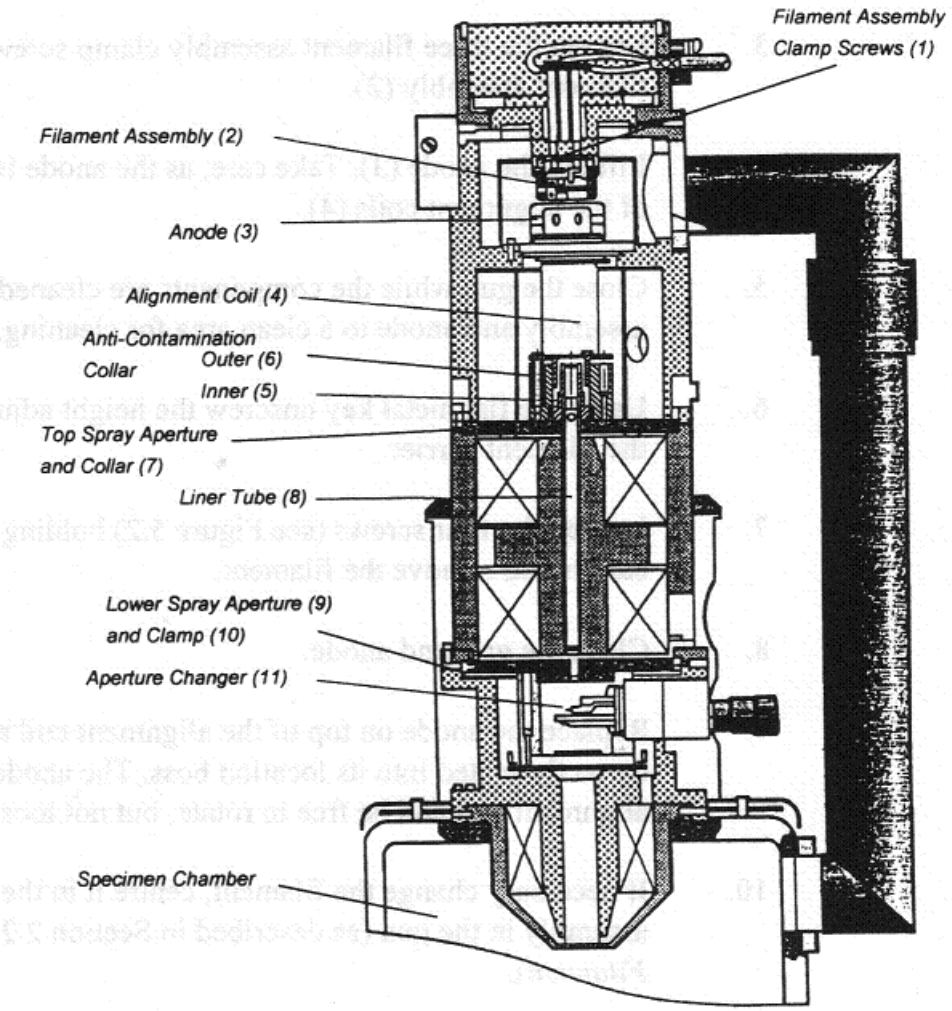


**Figure 3.8:** Diagram of the internal structure of the LEO S440 electron microscope [62]

not provide a leakage path to earth, and as such none of the electrons which impinge on the surface are absorbed. All are therefore given to the production of the various emissions shown in Figure 3.7, which may be picked up by the SEM detectors. This oversaturation then renders the processed image bright and featureless, and ultimately unusable. Naturally nonconducting materials are generally coated with carbon or some other conductive substance on the surface of interest. This surface is then grounded via the specimen mounting or connecting wire [61].

Figure 3.8 shows a diagram of the internal workings of an electron microscope. It can be seen that the electrons are transferred through several stages in their journey from the thermionic emitter filament at the top of the column, to the specimen housed in the chamber at the bottom. The total path of the electrons may be as

much as a metre, and as such a high vacuum is required in the column and the chamber in order to provide as great a mean free path for the electrons as possible. It is desirable to have the theoretical mean free path longer than the length of the column [61], and in order to achieve this, values of the order of $\tilde{}10^{-7}$mBar and $\tilde{}10^{-5}$mBar are necessary in the column and chamber, respectively.

Alongside the conductivity of the specimen, the integrity of the vacuum is one of the most important factors in the correct operation of the SEM. Not only do air molecules interfere with the electron beam, a good vacuum also serves to preserve the filament.

The final important point relevant to the project at hand is that the specimens are mounted on a stage which has various degrees of freedom associated with it. Base stage movement is in the x- and y-directions, while an additional assembly provides height, rotation, and tilt control. This is necessary as it is not possible to focus the beam in a particular direction, so the point of interest on a given specimen is moved to locate directly underneath the beam, which emerges from the top of the specimen chamber.



## 3.3 In situ Testing Rigs For Use Inside the SEM

The use of *in situ* fracture mechanics experiments inside a scanning electron microscope (SEM) has increased in recent years in the research community. Commonly when performing fracture mechanics tests, a specimen will be examined in a SEM post-fracture, and the surface analysed for clues as to the fracture mechanism. The ability to perform experiments inside the SEM chamber, and therefore observe in real time the response mechanisms of the specimen, allows researchers to determine the microstructural behaviour under load of a variety of materials and specimen shapes, a concept which is useful in the study of crack propagation in brittle materials.

With some models of scanning electron microscope there are available loading stages capable of standard uniaxial tensile and bending tests, such as the HITACHI S-570 used in the work of Ding *et al* [52], and Xu *et al* [63], and the Cambridge S-180 used by Tait & Garrett [26]. Other researchers make use of commercially designed tension/compression SEM rigs, such as the Shimadzu Ltd. rig used in work by Wang *et al* (2005) [49] and Wang *et al* (2008) [64].

Without these facilities, or if the desired test is more complicated than simple tension or bending, it is necessary to design an in-house testing rig that may be placed inside a conventional, unequipped SEM chamber, on a standard specimen

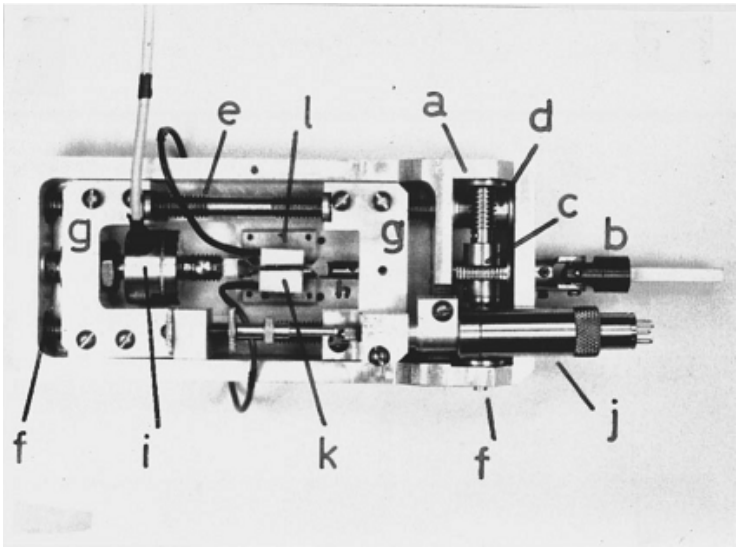


**Figure 3.9:** Miniature tensile tester constructed by Yawny *et al* [66]

stage. Special purpose-built rigs have been utilised by Tait & Garrett [26], as mentioned, and Vekinis *et al* [9], in double torsion. More recently, devices by Ghisleni *et al* [65] in nano-indentation procedures; Yawny *et al* [66] in tensile and thermal fatigue (shown in Figure 3.9); and Sørensen *et al* [67] in double cantilever loading, have been designed and used.

The following sections will take the reader briefly through the capabilities and previous uses of this type of technology, before considering the requirements and constraints involved in designing a device to operate in this particular environment.

### 3.3.1 Capabilities of the *in situ* Testing Technique

The purpose of this section is to demonstrate briefly the advantages of being able to perform loading experiments of some kind *in situ* inside a SEM chamber. This is done by reviewing examples of previous work performed for a variety of applications, with reference to how the *in situ* method contributed to the success of the work.

Straightforward tensile tests were performed on tin and tin/lead solder alloys by Ding Ying *et al* [52] with a commercially designed rig. The tests were used to determine the effect of loading rate on the damage nucleation behaviour of these materials. The deformation mechanism was shown to differ between the single and dual phase materials, but in both cases fracture remained intergranular for low displacement rates. As well in both cases, the fracture mechanism changed to transgranular at higher loading rates. This is interesting from the point of view of the discussion in Chapter 2 on the effect of available energy on this kind of behaviour.

Fatigue studies as well as uniaxal tensile studies were carried out on the struts of medical stent assemblies by Frotscher *et al* [68], also using a commercial rig, in an attempt to determine their response to the natural loading conditions which might be expected in service in the human body. Using this method they were able to identify microcrack nucleation as the primary cause of fast fracture initiation, where said microcracks were seen to develop from surface notches and flaws. This may have implications in the surface preparation standards for such devices.

Fatigue and uniaxial compression studies were carried out on concrete samples by Wang, Wu & Wang [49] in order to investigate the microcracking behaviour present, but this time at differing temperatures. They were able to conclude that temperature played a significant role in the microcracking behaviour of concrete structures. These tests were also carried out on a commercially developed SEM loading rig.

Perhaps less commonly, Ghisleni *et al* used the technique to investigate the behaviour of a material undergoing nano-indentation procedures [65]. Using an in-house SEM nano-indentation rig, they were able to determine the behaviours affecting the complex stress state that needs to be analysed when using indentation to determine material properties. These behaviours include 'pile up' and 'sink in' of the material due to plastic deformation, and together with a load-displacement recording, the researchers were able to account for these effects during the evaluation of material properties. They developed rigs for both SEM and TEM (transmission electron microscopy) techniques; their SEM rig is shown in Figure 3.10.

Lastly, and similarly to the current research, Sørensen *et al* used an in-house developed double cantilever rig to examine the R-curve behaviour of cubic-phase yttria-stabilized zirconia, a brittle material [67]. Shown in Figure 3.11, the device applies load to specimens similar in dimension to the DT specimen, but 'bends' the two arms, as opposed to twisting them. i.e. Each independent arm is treated as a cantilever, not a torsion bar. The advantages are similar to the DT method, in that there is a region of constant stress intensity, and the authors suggest that for R-curve determination, this method might be more suitable, as the crack profile developed is uniform, as opposed to curvlinear.

Attention is now focused on drawing together the various considerations which the aforementioned researchers (and others) were confronted with in the design or operation of their miniature loading units.

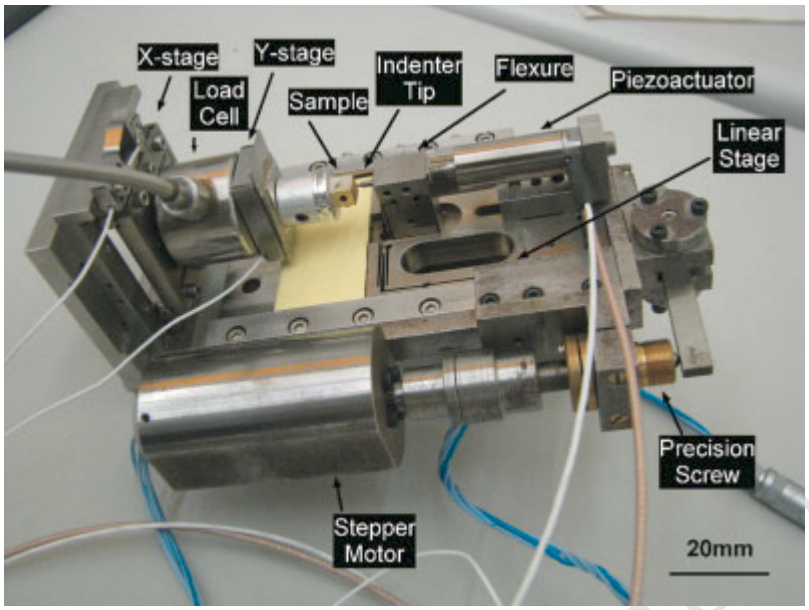


**Figure 3.10:** In situ indenter, developed by Ghisleni *et al* [65]

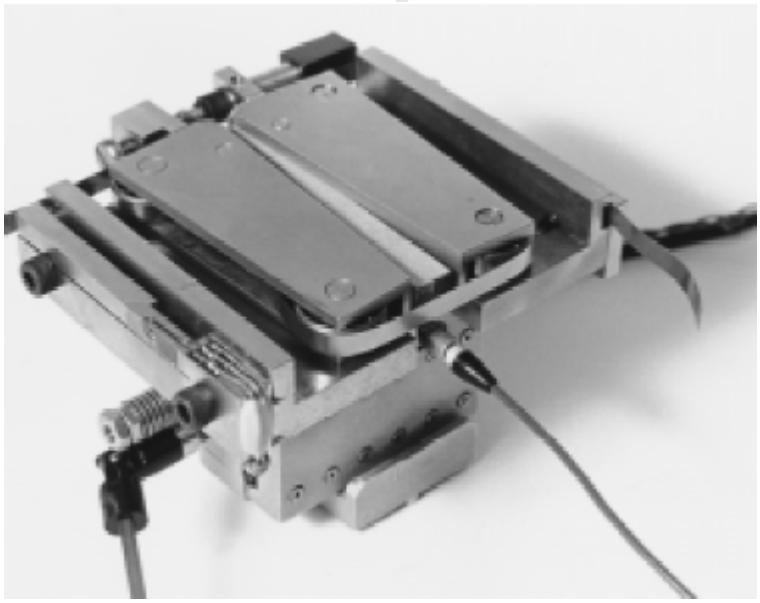

**Figure 3.11:** Double cantilever beam rig developed by Sørensen *et al* in order to perform loading studies on brittle materials, with a focus on R-curve behaviour determination [67]

### 3.3.2 Designing an in situ SEM rig

The design of a testing rig that can be placed inside a conventional SEM chamber without modification to the chamber structure itself, and perform fracture mechanics experiments, requires a number of considerations due to the size and specialized environment (i.e. vacuum) of the chamber. Load must be applied to the specimen and this load must be recorded in order to facilitate interpretation of crack advancement and damage behaviour. In some cases displacement must also be measured, as when performing fracture toughness tests.

Aside from these "rig in SEM" considerations, there are also a number of "specimen in rig" considerations which arise mainly due to the small field of view of the specimen during testing, which do not necessarily occur in macro-testing.

The following section gives comment to these considerations in their various categories.

#### 3.3.2.1 Size

Within a SEM, the complete size of the rig is limited by the size of the chamber, taking into account the intended freedom of movement of the conventional loading stage. That is, if the rig is to be placed on a conventional stage, the dimensions of the rig must not limit the vertical or horizontal movement of the stage, as these limits are difficult to monitor once an experiment is in progress. The specific size requirements depend on the SEM the rig is being designed for, but it is prudent to have a smaller design which may then be employed in a larger chamber if necessary, such as that designed by Yawny *et al* [66] for the small chamber of the Philips 515 SEM.

#### 3.3.2.2 Load Input

With the size limitation comes the problem of applying load to the specimen in question. This is commonly done through the actuation of mini-crossheads by a DC motor, subject to required gear reductions in the process [66, 67].

Adequate space may allow for a motor to be installed on the rig, which results in a self-contained unit inside the chamber. This may be seen incorporated into the rig shown in Figure 3.12, which was mounted onto the door of the SEM at the University of Purdue.

When there is limited space or concern over interference, one may have to mount the motor outside the chamber, in which case a method of transmitting the torque

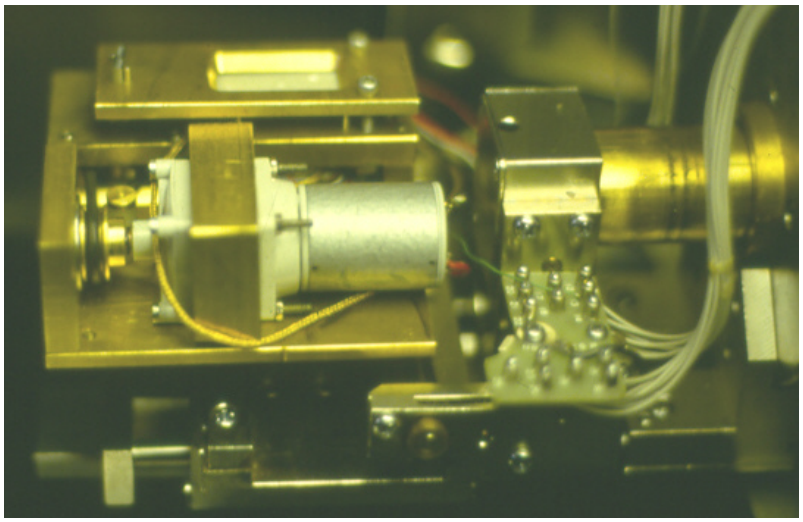

**Figure 3.12:** Miniature Double Torsion rig fit to the door of the SEM at the University of Purdue [50]

from the motor to the rig, while maintaining high vacuum, must be designed. Tait & Garrett [26] and Yawny *et al* [66] have used this method. In the case of Yawny's rig, two universal joints were employed. One joint was connected to the input shaft mounted on the rig (marked 'b' in Figure 3.9), and the other was connected to a special port mounted in the chamber wall which housed the motor on the outside. This port is shown in Figure 3.13 and the universal joint may be seen, marked 'a'. Between the two joints was connected a flexible cable to help absorb any vibration. An external view of Tait's stepper motor drive and port is shown in Figure 3.14.

If this latter method of mounting the motor outside the SEM is used, care must be taken to ensure proper sealing, as the vacuum inside the chamber must be maintained [61, 66].

#### 3.3.2.3 Data Output

In order to extract the value of the load applied, and if necessary, the displacement experienced, the rig must incorporate sensing devices such as load and displacement transducers.

The most simple data extraction device is the strain gauge, and in Tait & Garrett's work [26] a three-pronged strain gauge layout was calibrated to extract both load and displacement data (Figure 3.15). Sørensen *et al* [67] also used strain gauges to extract their load data, coupled to a half-bridge Wheatstone Bridge strain recorder.

Commercially available pre-built solutions are also available, and many researchers

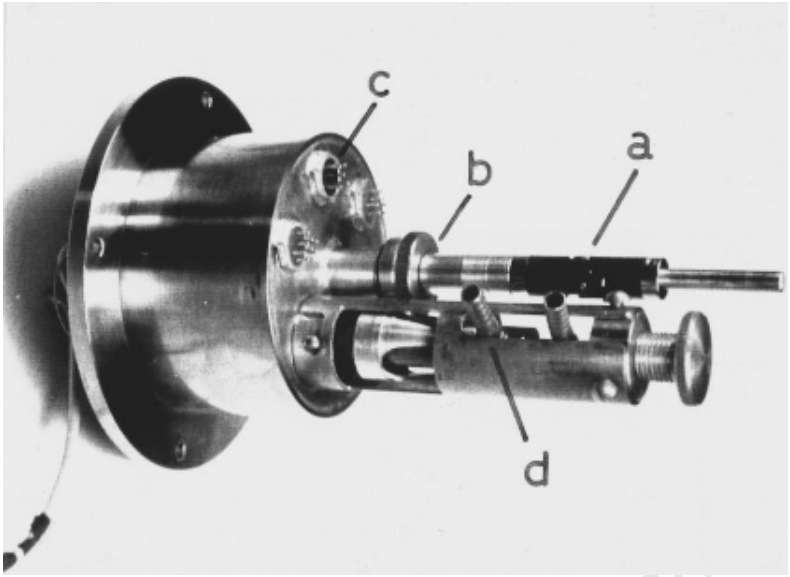


**Figure 3.13:** Vacuum port devised for use with Yawny *et al*'s tensile tester. Note the features: (a) Universal joint to transmit input motion; (b) O-ring seal to maintain vacuum integrity; (c) Electrical connectors; (d) Cooling jacket circulation ports. [66]

**Figure 3.14:** External motor drive arrangement used by Tait in previous work [50]

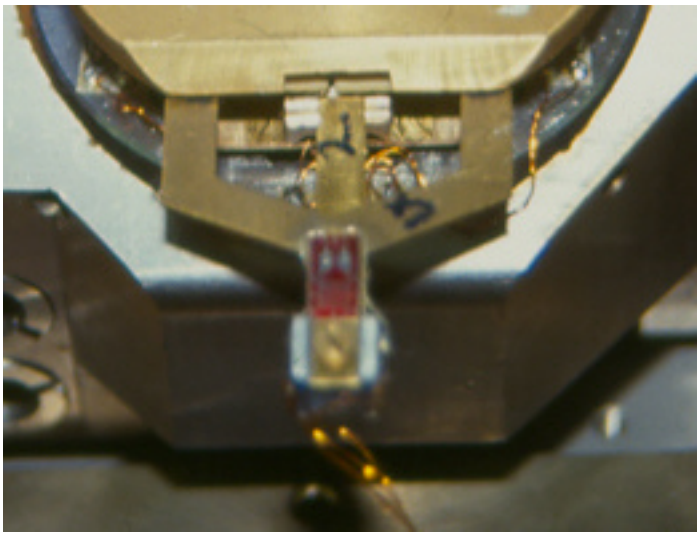

**Figure 3.15:** Strain gauge arrangement in order to gain load and displacement data, used by Tait [50]

make use of the linear variable differential transducer (LVDT) to extract displacement data [66, 67], and load cells of a suitable range to extract the value of the applied load [65, 66].

The aforementioned devices all have an electrical output, which must be powered and connected to recording equipment capable of interpreting the signal. Consideration must be made of the error inherent in such a setup. If the strain gauges are located far from the recorder, the resistance of the connecting wires alone may exceed that of some smaller strain gauge outputs, a problem made worse by heating of the wires. Quarter-bridges are also susceptible to drift due to temperature variations of the system, but may be remedied by the use of a second working gauge in a half bridge configuration. There are other additions which may be incorporated to try and cancel out some of the errors in the system, such as incorporating a three-wire connection, or the use of a full strain gauge bridge [69, 70]. A good review of the measures that may be taken is provided by the National Instruments Corporation [70].

#### 3.3.2.4 Electrostatic Considerations

Unlike an optical microscope which uses a light source, a scanning electron microscope uses an electron beam source to generate images. An electron beam is directed towards the sample being analysed, causing electrons to penetrate the surface of the material. These electrons interact with the atoms of the material and displace what are known as "secondary electrons" from the material. It is these secondary elec-

trons (as well as other emissions) which are collected by a detector and converted to a signal which generates the images on the visual display unit [61, 71].

If the materials inside the chamber are not conductive, electron buildup on the surface produces a charge buildup on the material surface, resulting in a high detection rate. This results in a distorted image which appears very bright, making details of the sample surface difficult to discern. Non-conductive materials require thin coating with an electrically conductive material before viewing. For the reason above the whole setup inside the chamber must also be grounded so as to provide an electrical path for the additional charge to dissipate.

In at least one study, however, the electrostatic buildup effect proved helpful to the researchers. Tait & Garrett [26] found that when performing slow crack studies on coated samples of cement mortar and cement paste, new cracks which opened up were easily visible due to the ungrounded subsurface having a brighter, electrostatically charged appearance. This is especially useful in characteristically "rough" materials, which have many features that serve to hide atomically sharp crack growth.



#### 3.3.2.5 Electromagnetic Considerations

For stability of the image being generated, no sources of electromagnetic interference should be present inside the chamber. If this is unavoidable, adequate shielding should take place [61]. Electromagnetic interference distorts the electron beam, resulting in the distortion of the final image. This consideration is easily accommodated with the physical structure of the loading device, as in the case of Sørensen *et al* [67] who manufactured their testing rig of entirely non-magnetic materials. Ghisleni *et al* [65] also imposed a design limitation on their nano-indentation device in that all equipment attached to the rig should have a low electromagnetic disturbance. This is especially important in the selection of a DC motor when the design puts the motor inside the chamber.

The signal output from the strain recording devices is also susceptible to electromagnetic interference. Particularly because the signal voltage generated is so small, background interference may have a large effect on the output reading. If there is a sufficient amount of interference around the equipment, the wires should be shielded [69].

#### 3.3.2.6 Vacuum Environment

The pressure in the SEM chamber is very low, as air molecules interfere with the mean-free-path of the electrons, and result in image distortion. Specimens and components used in the rig should be able to operate in a near-vacuum environment, and not "out-gas", which is the term for the release of entrained gas or vapours from the material under load or vacuum. This precludes analysis of specimens containing water, as the water evaporates in the low pressure. Such experiments require the use of an environmental SEM (E-SEM), which is beyond the scope of the current research.

As a further related consideration, cleanliness is of great importance inside the chamber due to the need to ensure the longevity of the vacuum pump and filter. This limitation means that loading stage assemblies should not require significant lubrication, as loose or out-gassing grease particles will clog up the filter [61].

#### 3.3.2.7 Loading Symmetry

While loading symmetry is of great importance in the double torsion beam technique [11, 12], it is made even more critical when the loading is applied within a SEM environment. Commonly in the literature, rigs are built to impart equal displacements on either side of the specimen concerned [65, 66, 67]. For example, in the tensile rig shown in Figure 3.9, two crossheads are driven by being mounted on the same threaded rod, with opposite-handed threads for each crosshead. This ensures that for each turn of the driving rod, the crossheads will move an equal distance in the opposite direction. Unsymmetrical loading results in drift of the specimen relative to the electron beam, therefore these measures are taken to ensure the specimen area in focus remains within the small field of view provided by the SEM image.

The symmetric loading of a specimen in a tensile type test can be ensured by the method described above. However, the four-point loading required in a double torsion test requires the load to be perfectly balanced on either side of the specimen. Careful machining notwithstanding, this may be achieved by a self-aligning mechanism such as was used in the macro-scale rig of [12], shown in Figure 3.16.

Tied in with this is the importance of accurate specimen alignment. The double torsion method relies on perfect symmetry to propagate a straight crack, with the load being applied at equal distances from the centre line; even a mild misalignment of the specimen may cause the crack to grow off-centre, and wander out of the acceptable $W/8$ limit either side of the specimen centre. Tait *et al* have evaluated the use of grooves to guide cracking, as has been done by other researchers for different

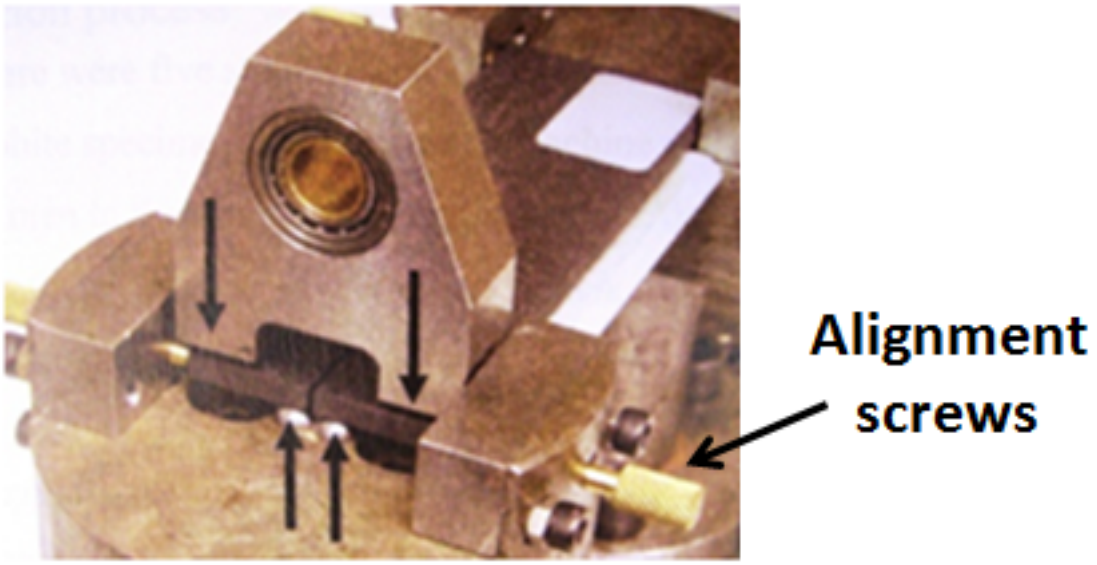


**Figure 3.16:** Self-aligning load applicator [12]

specimens [67], but have concluded that ungrooved, carefully aligned specimens provide the best results [11]. Alignment may be ensured by placing physical location points on the rig, although this may prove a hindrance if specimens themselves are not perfectly machined and aligned. It also limits the rig to only test specimens of a certain dimension. An alternative employed by Becker is to align the specimens by eye according to some background reference, with fine tuning being performed by a series of locating screws protruding from the testing rig which may be seen in Figure 3.16 [12].

#### 3.3.2.8 Loading Precision

Not only the symmetry of the load, but also the precision of the load and loading rate, is of paramount importance in fracture mechanics testing on this small scale. Microstructural rigs must be able to apply extremely small loads, which are reliant on extremely small displacements of the various crossheads. Yawny *et al* report that for one turn of the DC motor output shaft the relative displacement between the two crossheads of their tensile tester was $1.8 - 1.9\mu$m [66], while Sørensen *et al* report that they had loading rate control of down to $1\mu$m/s [67]. In brittle materials the loading rate plays an important role in ensuring stable crack propagation, and Tait [50] has managed to achieved crack propagation increments in glass of the order of a micron with a well-manufactured miniature double torsion system, Figure 3.17.

The displacement rate, and hence loading precision, of the system depends on the

**Figure 3.17:** Crack propagation in glass at different loading stages; glass etched with hydrofluoric acid as a viewing aid. Crack propagating from top left, in series, to bottom right. The neck of the etch pit highlighted in the second image is of the order of a micron, shown by the micron bar. [50]

type of torque transmission elements used. High ratio reductions can be achieved with a worm gear arrangement between the input shaft and the loading mechanism (e.g. lead screw) [66]. Using a stepper motor in place of a continuous DC motor may also increase the level of precision gained.

A further consideration regarding load is that a smaller system may be more susceptible to frictional effects than a larger system, where these would otherwise be negligible. Intelligent placement of strain recording devices will ensure that any friction inherent in the system will not contribute to the load and displacement data acquired, i.e. placing devices as close as possible to the specimen being tested so that any strain measured is as a direct result of the load being applied, with no friction-causing mechanisms in between.

## 3.4 Digital Image Correlation

It is useful to be able to extract further data out of the SEM micrographs than just topographical observations. In the macro-DT work previously mentioned [12], the Electronic Speckle Pattern Interferometry (ESPI) technique was used to subtract successive images from each other in real time, resulting in an output which showed displacement fringes using the previous load step as a reference. These displacement fringes are useful for showing areas of increased activity, such as the process zone of nuclear graphite.

ESPI and other related techniques, such as the digital speckle correlation method (DSCM) are difficult to perform inside a scanning electron microscope, as they require the installation (and modification) to the SEM of equipment specific to the technique (e.g. laser emitters, further detection equipment). Not only is this difficult in what is a crowded specimen chamber, the additional ports required also compromise the integrity of the chamber vacuum.

Alternative methods include the performance of an analysis on the micrographs extracted from the SEM software. This involves the process of Digital Image Correlation (DIC), which is much the same as an ESPI technique. The difference is that in ESPI the pattern on the material is generated by some sort of diffraction technique (e.g. laser beam), whereas with DIC the pattern is physically applied to the specimen using paint or some other marking technique [72].

Another method is the use of stereophotogrammetry, which has been used in the past in attempts to visualise the microcracking process zone in brittle materials [73, 74]. The basic principle involves using two micrographs taken of the material

surface in different strain states, and using a device that coordinates the eye/brain to differentiate the areas that have undergone deformation. Recent developments have been able to automate this procedure to computationally analyse the various images, producing deformation and strain profiles throughout the observed region [75].

Both of the methods presented above report a reasonable accuracy when considering possible use with the double torsion method and nuclear graphite. The DIC method is able to determine displacements of approximately 1$\mu$m, while the stereophotogrammetry method reports analysis over every fourth pixel. In the local SEM, this may correlate to a resolution of under 0.4$\mu$m.

## 3.5 Summary

This chapter has dealt with the practical topics which are relevant to the development of a system which can perform *in situ* double torsion experiments inside the chamber of a scanning electron microscope, as well as retrieve a variety of outputs.

The history and applications of the double torsion technique have been covered, complete with the assumptions that the method is based on, which give an idea of the limitations which may be encountered in the interpretation of experimental results. The environment of the SEM has been explored, and previous *in situ* devices employed in this way have been described. The method of digital image correlation was researched so as to provide a background on the technique for future experimental reference.

Drawing heavily on the information presented in this chapter, the following chapter deals with the actual design of the mini-DT rig used in the current work.

# Chapter 4

# Design Process

This chapter presents the final design solution for the miniature Double Torsion (DT) rig, and covers the process undertaken in its design and construction.

The goal of this chapter is to take the reader through the design process, with special focus on the constraints of the operational environment of the rig on the design solution, as explained in Section 3.3.2. The overall design and the features thereof are presented as a solution to the problem and the particular constraints mentioned.



## 4.1 Problem Definition

The problem that was defined covered the design of a miniature DT rig capable of conducting fracture mechanics tests on suitably sized brittle material specimens inside a scanning electron microscope, specifically the LEO S440 housed within the Electron Microscope Unit at the University of Cape Town, and the provision of means to observe and record directly the live events during such a test.

The problem can in essence be reduced to three requirements, in that the system is required to:

- hold a test specimen;
- load a test specimen; and
- output relevant data.

#### The Specimen

The DT specimen in question, based on the recommendation in the work of Tait, Fry & Garrett [11], was dimensioned according to a $3 : 1 : 0.1$ scale. The result,

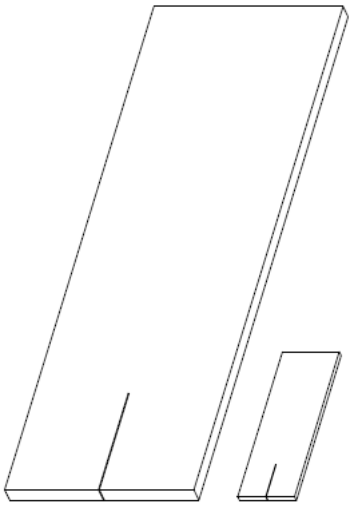

**Figure 4.1:** Size comparison of the macro and miniature DT specimens.

shown in Figure 4.1, is a DT specimen of dimensions 45 x 15 x 1.5mm. The length-to-breadth ratio is identical to that of the macro-specimens used in previous work done by Becker [12], whereas the thickness ratio is slightly greater.

The elements of the problem are further delineated by means of the performance requirements set out in Table 4.1, and explained in the subsequent sections. Constraints defined in the problem are specifically discussed with reference to the particular equipment available.

### 4.1.1 Holding the Specimen

This section further explains the problems defined in terms of the location and seating of the specimen in the rig. That is, the specimen had to be housed in a device that facilitated testing in the environment of a scanning electron microscope, as well as being held symmetrically for analytical purposes.

#### 4.1.1.1 Holding the Specimen Inside the SEM

The environment that the specimens were to be tested in was the vacuum chamber of the LEO S440 SEM. The testing rig therefore had to be designed in such a way as to function properly inside the chamber in line with the size, vacuum, motion, and electrostatic constraints inherent in this environment.

**Size** The chamber is of a limited size, which imposed width, length, and height constraints for the physical rig. Figure 4.2 shows a photograph of the inside of the

**Table 4.1:** Performance Requirements for *in situ* DT system

| **Functional Requirements** | | | | **Performance Requirements** |
|---|---|---|---|---|
| *Requirement* | *Sub-requirements* | | *Possible solution* | *Required Value* |
| **Hold Specimen** | | | | |
| ↪ | Symmetry | | Locating mechanism | |
| ↪ | Inside SEM | | | |
| | ↪ | Size limit | | 100x150x75 |
| | ↪ | Vacuum compat. | | ~10^-5 mBar |
| | ↪ | Stage width | | 162mm |
| | ↪ | Spec motion \|\| to stage motion | | |
| **Load Specimen** | | | Moving crosshead<br>Pivotal lever arm | Up to 200N |
| ↪ | Symmetry | | Bearing<br>Immovable level surface<br>Guide rods | |
| ↪ | Motor | | | |
| | ↪ | Outside | DC stepper motor | |
| ↪ | Applicator | | | $1\,{}^{\mu m}/_{\mathrm{s}}$ |
| | ↪ | Reduction | Worm gearing [66] | |
| | ↪ | Lead screws | | |
| | ↪ | No lubrication | Teflon bushes<br>Sealed bearings | |
| Read Data | | | | |
| ↪ | Load data | | | |
| | ↪ | Capacity | | Variable. (Graphite: <100N) |
| | ↪ | Sensitivity | Commercial load cell<br>4-gauge strain bridge | $500\,\mu$strain |
| | ↪ | Response time | | >0.1s |
| ↪ | Video | | | |


**Figure 4.2:** Photograph showing the interior of the SEM specimen chamber. The electron beam aperture (1) protrudes from the ceiling centre, with the secondary electron detector (2) protruding from the back wall. The stage arrangement, which is fitted to the open door, is just visible in the bottom left (3).

chamber. As one can see in the figure, the head space is restricted by detector equipment protruding from the upper portion of the chamber walls and ceiling.

As a guide to the size limit imposed, with reference to Figure 4.3, it was decided that in terms of length, no part of the new device should protrude past the end of the stage (i.e. towards the back wall) at any time in operation. This meant allowance had to be made for the movement of the rig during a specimen test, explained in a following paragraph. In terms of width, the limit was set in consultation with the chief SEM operator as being no wider than a previous device which had been successfully implemented. Head space was measured from the base adapter (Item 3 in Figure 4.2) to the bottom of the electron beam aperture, and approximately 25mm taken from this value in the interests of conservatism. The final limits to the dimensions of the design solution were: Length - 100mm; Width - 150mm; Height - 75mm.

**Vacuum** The chamber operates under high vacuum, at a quoted air pressure value of $10^{-5}$mBar [76], which meant that there could be no liquid content associated with

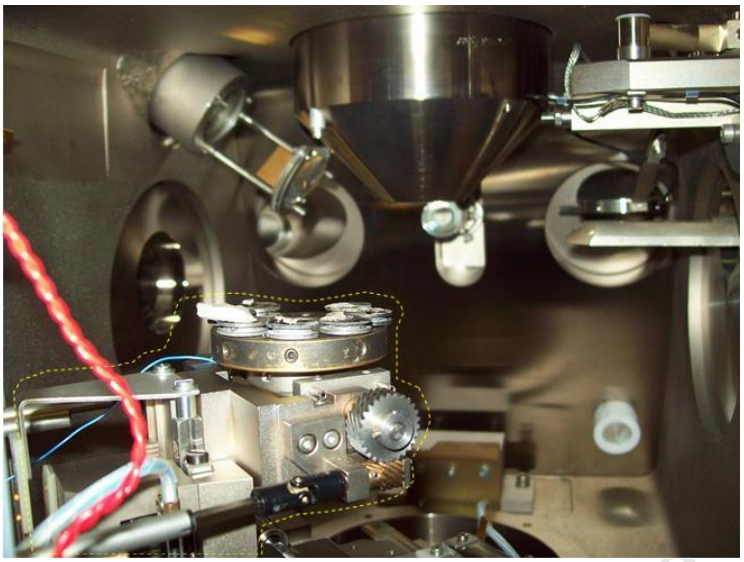

**Figure 4.3:** Photograph showing the SEM stage with the rotation and tilt mechanism in place (highlighted). Due to the height of this setup (note the distance between the specimen stub and the electron beam aperture), the mechanism would have to be removed in order to install a fracture mechanics rig.



either the material being tested, or the testing rig. While traces of liquid may be removed by the vacuum pump, any more than trace amounts tend to block the pump filter elements and put strain on the pump motor, and in some cases, such as with a particularly gaseous specimen, the required vacuum for the beam to operate may not be reached. This precludes the use of lubricants of any sort in the rig structure, including areas with moving parts.

**Motion** Equipment attached to the SEM stage provides 5 degrees of freedom: x- and y- direction control, height, rotation, and tilt. At best the rig had to be able to follow a lengthening crack in the material specimens, with the crack propagation direction parallel to one of the motion directions. The specific configuration of the equipment which provides these capabilities determined how best to incorporate the rig with these functions, and determined which degrees of freedom could be retained, and which had to be sacrificed.

Because of head space constraints, the total height limitation for the rig was measured from the base adapter, mentioned earlier. This measurement therefore was only valid if the rotate and tilt mechanism attached to this base adapter was removed (see Figure 4.3). As this mechanism also controlled the height function, the SEM stage was left with just an x- and y- directional capability, having had the rotation, tilt, and z-adjustment functionality removed. This was considered

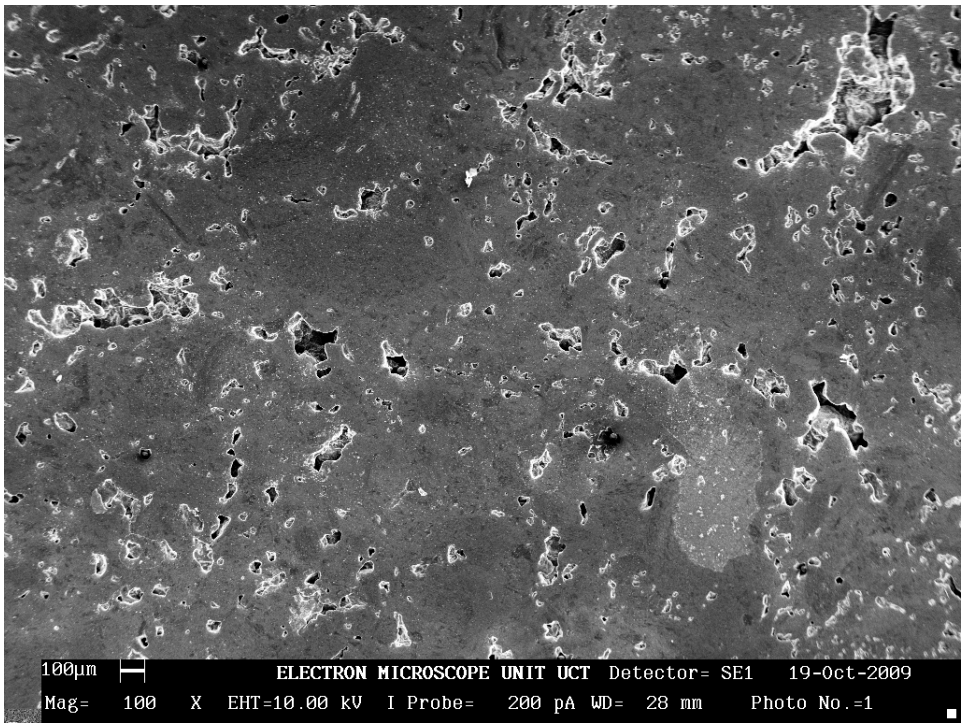


**Figure 4.4:** Sample image of coarse-grained graphite in the SEM. Note the glowing edges around pore features. This is due to electron buildup, as electrons cannot sufficiently escape to ground in these regions [77].



sufficient to satisfy the functional purpose of the rig in holding the specimen, in that it was still capable of following a lengthening crack.

**Electrostatic Buildup** The specimen and rig structure are subject to electron impingement in the SEM, and, if not grounded, produce electrostatic buildup which renders glowing physical features in the process image. Figure 4.4 shows an example of this around the edges of pore features in graphite, where the sharp edges do not provide an adequate path for the charge to disperse over. This effect is also seen in non-naturally conducting materials which have been coated for SEM use. As regions of the material become damaged, new uncoated material is exposed, which also accumulates charge.

For a completely non-conducting, uncoated, or ungrounded material or structure, the glow would encompass the entire image. Care, therefore, had to be taken to ensure that any part of the structure in close proximity or exposed to the electron emission had a leakage path to earth.

#### 4.1.1.2 Holding the Specimen in Symmetry

Equation 3.2 for analysing the stress intensity at the crack tip of a crack induced in a double torsion specimen, assumes the distance between the inner and outer loading points are symmetrical about the crack. This is to uphold the condition that the two halves of the specimen experience the same torsion.

It was therefore necessary to ensure the specimen was held perfectly symmetrically within the rig. With reference to Figure 3.1, this meant primarily that the starter notch and associated axis of symmetry on the specimen was to be aligned midway between the inner loading points on the rig, for the entire length of the specimen.

### 4.1.2 Loading the Specimen

The solutions to be found concerning the loading of the specimen were identified as: devising a mechanism to transfer load to the specimen in minute load increments; providing an actuation means for the load transference mechanism; and, similarly to the previous section, ensuring the load application was perfectly symmetric. The upper load requirement on the specimen is calculated according to Equation 3.2, using the aforementioned specimen dimensions and a fracture toughness value of $10\text{MPa}\sqrt{\text{m}}$ [1] to be $\sim 194$N. Nuclear graphite requires only $\sim 50$N, having a reported fracture toughness of $2.2\,\text{MPa}\sqrt{\text{m}}$ [12]. See Section C.1 in Appendix C for sample calculations.

#### 4.1.2.1 Loading Mechanism

Point loads must be applied to the specimen according to Figure 3.1. Since a commonly recommended method for applying a point load is through the use of loading spheres [11, 54], it was decided *a priori* that this method would be used. The remaining design would be concerned with the device in which the spheres would be mounted.

Regardless of the final design of the load transference structure, it was clear that a reduction would have to take place between an actuation device and the final load applicator. This was deduced from similar work done by other authors, who found that application speeds of as little as $1^{\mu m}/_{s}$ were necessary for work conducted inside a SEM [66]. This value was taken as a guideline for the load application speed of the miniature Double Torsion specimen.

[1] In line with common experience of the upper values of standard brittle materials

#### 4.1.2.2 Load Actuation

The motor chosen for this application had to be able to provide minute control within a certain range, factoring in that any motion would be able to be geared down to some extent.

A major constraint in this was that the motor would have to be mounted on the outside of the SEM structure, so as to minimize electromagnetic as well as vibrational interference. This necessitated the use of a vacuum port such as the one used in the work of Yawny *et al* [66]. Fortuitously, there exist two spare vacuum ports on the University of Cape Town SEM, which were investigated for suitability of use in this regard.

#### 4.1.2.3 Load Symmetry

Similarly to what was explained in Paragraph 4.1.1.2, the specimen loading must be completely symmetrical for the length of the specimen in order to keep Equation 3.2 valid. Not only this, but asymmetrical loading causes the crack in a double torsion specimen to deviate from the intended longitudinal path, which is only acceptable within the range mentioned in Section 3.1. Aside from the mathematical validity of a deviated crack, such an occurrence while testing inside the SEM chamber would necessitate perpendicular readjustment of the SEM stage to keep the crack tip inside the field of view of the SEM electron beam.

### 4.1.3 Data Output

This section describes the various outputs required in order to sufficiently analyse the behaviour of a specimen subject to DT loading.

#### 4.1.3.1 Load Output

From Equation 3.2 it can be seen that to calculate the stress intensity factor, $K$, for the DT specimen, one merely needs the value of the applied load, as well as the dimensions of the specimen. This is, of course, the advantage of the DT specimen, in that the stress intensity does not rely on the crack length.

The constraints in the current application again fell to size limitations and precision concerns. Whether commercial or in-house built, the load cell used would have to be fitted to a small device, and therefore its physical size was important.

Sensitivity was also a concern. In-house knowledge dictated that a strain sensitivity of $\pm 1000\,\mu$strain at maximum load was an appropriate value for a strain-based

load cell, given the working loads required.

#### 4.1.3.2 Displacement Output

Usually in fracture toughness work the two sets of fundamental data required are load and displacement. This data is used to determine properties such as stress values or Young's Modulus, where as the purpose of the DT method is to investigate slow cracking behaviour. As explained above, this is quantified in terms of v-K behaviour, and it is therefore important to note that crosshead displacement data is not explicitly needed in order to analyse a DT specimen, as it is not required in order to determine the stress intensity.

What is useful however, especially if one uses the "Constant Displacement Rate" technique discussed in the previous chapter, is the crosshead displacement *rate*. This may be gained either through the use of a strain gauged item where displacement could be analytically determined via simple beam theory or calibration, or inference may be made from the input drive speed, knowing the reductions and conversions that occur in the drive train.

#### 4.1.3.3 Video Output

Velocity of the crack may also need to be determined visually; this is needed especially if one makes use of the "Constant Load" technique. This lead to the conclusion that dynamic video footage was required, not only for the above mentioned consideration, but also for the recording of the dynamic events involved in crack growth in brittle material.

Constraints included the mechanism of image production in the SEM - i.e. the microscope does not operate using light as with an optical microscope, but rather forms an image based on the reflection of electrons impinging on the material. For this and other reasons it was impossible to mount an optical video camera (e.g. web cam, etc.) inside the chamber; to get the image one needed the camera would have physically interfered with the electron beam aperture structure. Additionally, it would have subject the beam to electromagnetic interference, distorting the image produced, which also holds for any light source installed to aid the optical imaging process.

What was available was a *HyperConverter*$^{TM}$ image splitter which takes its feed from the SEM visual display unit (VDU). Aside from the input port to the VDU, the processor also had s-video and PAL/NTSC outputs, all shown in Figure 4.5.


**Figure 4.5:** Output ports on SEM image processing unit. Note the input from the VDU in the centre, as well as the analogue coaxial output and digital s-video.

## 4.2 Conceptual Solutions

In this section, potential solutions to some of the aforementioned problem statements are discussed in terms of their advantages and disadvantages, with relevance to the constraints presented. Some items from the problem statement were not thought to require conceptual design, and so are not discussed here.

### 4.2.1 Solutions to Holding the Specimen

The most important concern regarding holding the specimen was the ability to position it symmetrically about the loading supports. This raised the question of whether it would be better to have fixed specimen guides, which then meant no specimen alignment was required (or possible), or to mount the specimen loosely, and have some alignment procedure which would have to be performed each time a specimen was loaded.

**Location Pins** Figure 4.6 shows the concept of locating pins, spaced exactly the width of a specimen apart, between which specimens would be placed with the assurance that there is no room for human misalignment. This is similar to the idea used in a previous work where the specimen was housed between the rig walls, shown in Figure 4.7.

The advantages of the idea include the fact that no special alignment is necessary with this design; the specimen is repeatedly located in the same position with respect to the load applicator. There is also no possibility that the specimen may become misaligned while adjusting other portions of the rig, or closing the SEM door, etc.

However, there is no room for adjusting the alignment in the case of the specimen having an off-centre notch; neither is their space for accommodating specimens which have a larger width than the guide pins, i.e. the pins limit the rig to use only with

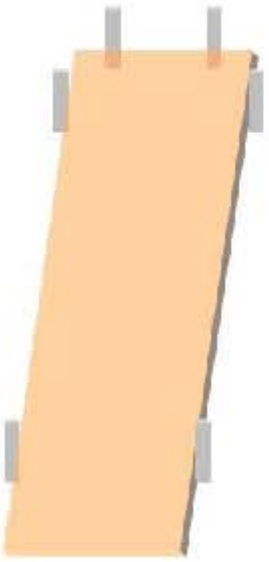

**Figure 4.6:** Guide pin concept for holding the specimen in the rig

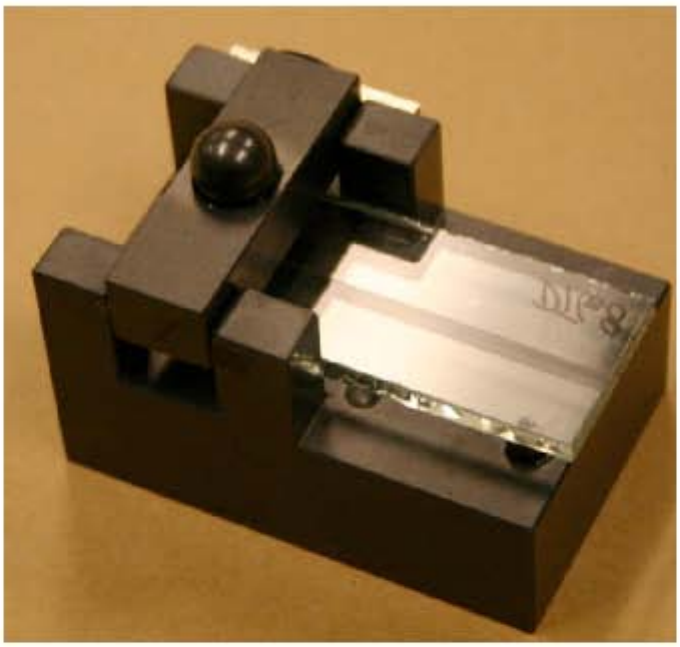

**Figure 4.7:** Previous double torsion rig, housing the specimen rigidly between the rig walls. [10]

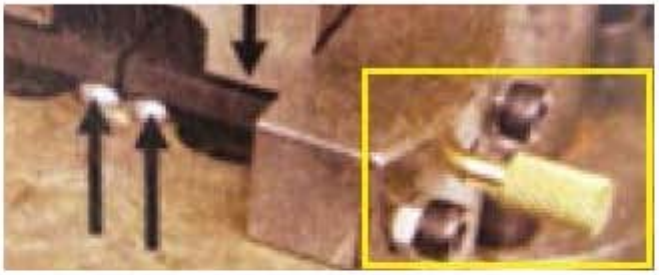

**Figure 4.8:** Example of fine tuning screws, reported in Becker [12]

specimens of a particular width. It is better, in the case of a notch which is shifted to the left or right of centre through machining error, to be able to position the specimen so the notch itself is centred between the loading points, as opposed to aligning with respect to the true middle of the specimen. Furthermore, there is the possibility of interference with the loading of the specimen. If there is friction between the specimen and the pins as the specimen twists under loading, the reaction load would provide an unknown quantity in terms of the analysis of the DT specimen.

**Locating Screws** The locating screw idea (Figure 4.8) provides a method of 'nudging' the specimen away from the screws at a controlled rate, due to the screw displacement being controlled by its pitch. Four screws would be used, one at each corner of the specimen, and would be retracted once the alignment is complete.

This method gives the ability to adjust for inaccuracies in the specimen dimensions, or notch aligment, and the screws do not interfere with the specimen under loading. The specimen is, however, left loose, and so may still misalign with any knocking or jerking of the rig.

### 4.2.2 Solutions to Loading the Specimen

Concerning the loading of the specimen, various points required conceptual design. Ideas are presented here for choice of loading apparatus and drive system.

#### 4.2.2.1 Loading Apparatus

The structure through which load is transferred from the drive system to the specimen is regarded. Previous (macro) DT designs have seen a split between a direct overhead crosshead and a lever arm, or pivotal, design.

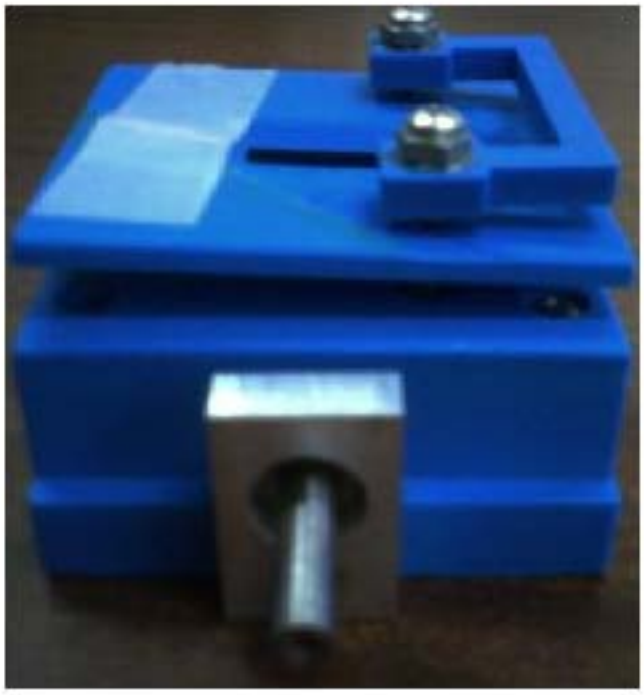

**Figure 4.9:** Full view of a previous pivot-type rig. The top plate rests on the base through a pivot located under the left side of the plate, as seen in this picture. On the right there is a loading arm which is drawn down and depresses the plate on to the specimen resting underneath.

**Overhead Crosshead** Figure 4.7 shows one example of the overhead crosshead design. Load is brought to bear down on the specimen underneath via an external loading apparatus which displaces the beam from above. The advantages of this design, which sees the crosshead mounted between the rig walls, is that there is no need for alignment of the structure. Any alignment with the load applicators (e.g. spherical mounts in the crosshead) is done via specimen adjustment.

The disadvantage is that there may be friction between the contacting sides of the beam and rig walls, and also the possibility that the load applicators are misaligned with respect to the crosshead, i.e. not mounted perfectly about the centre. This, however, can be overcome with lateral specimen alignment if that option is available.

**Lever Arm/Pivot** The lever arm, or pivot design, is characterised by load being applied at the end of an arm which rotates around a joint on the base of the specimen. Previous examples include the various rigs by Tait [26, 50] and Becker [5, 12], and these may be seen in Figures 3.12, 4.9, and 4.10.

The advantage of a pivot over the rigid crosshead is that the load can still be symmetrically applied in the case of some misalignment of the specimen with respect

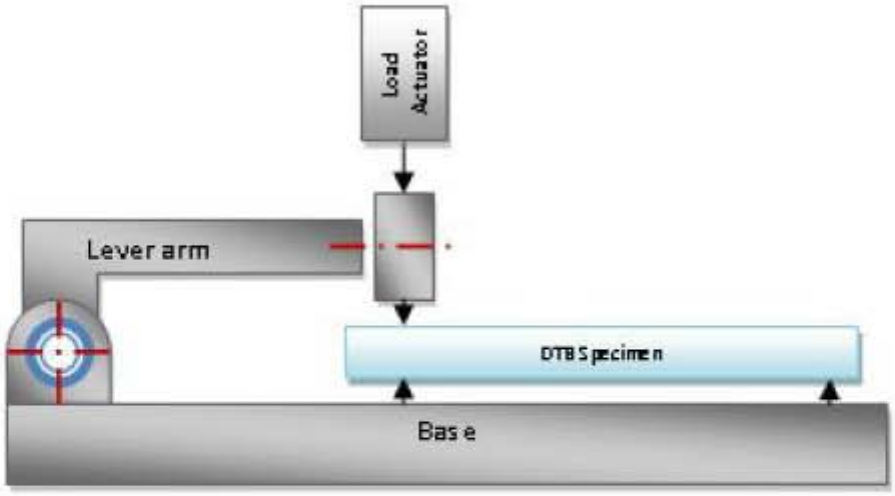


**Figure 4.10:** A representation of the rig used in Becker's early work [12]

to the loading points. That is, the pivot allows the loading arm to rotate on its own axis, in order to ensure load is evenly distributed between the loading points.

Disadvantages include the extra parts to be machined and assembled, but also, considering the load and moment distribution in such a setup, the fact that the entire load experienced by the pivot arm is not transferred to the specimen. While this is not an issue in the case of a load supply external to the system (e.g. a separate tension/compression tester), it becomes a matter of efficiency when the load is supplied by a motor or some actuator integral with the system. Due to size restrictions, the actuator and drive should be kept small, which means that where possible, load should not be lost or shared with parts of the system other than the specimen.

#### 4.2.2.2 Drive System

To achieve an acceptable loading rate, the input speed from the motor had to be reduced drastically. It was decided initially, based on methods in common use, to incorporate a geared drive with rotary-to-linear actuation via lead screws. The concept involves drawing down screws or threaded rods which are attached directly to the load applicator (either crosshead or pivot arm, etc), which in turn applies load to the specimen. This idea may be seen in Figure 4.9. The final solution to this design also had to ensure that some form of symmetry was enforced in the displacement of the applicator. The following concepts work on the idea of a final driven gear in the reduction train having a form of 'nut' inserted, with which to translate motion to a mating threaded rod.

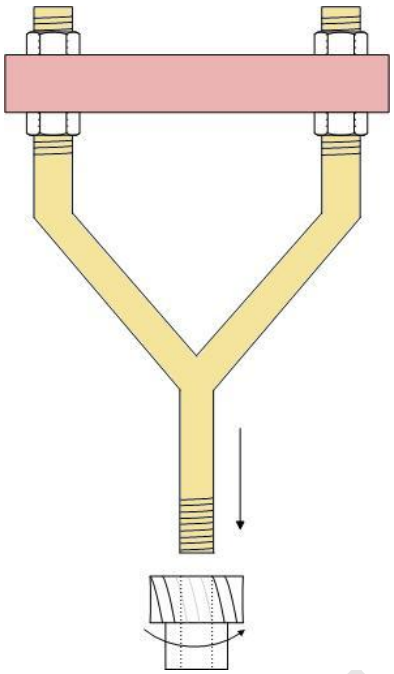

**Figure 4.11:** Single driven rod split into two for even loading. The loading plate, or crosshead, is secured on to the threaded rod arms by nuts, and the whole structure is drawn up or down via the rotation of a geared nut.



**Single Driven Rod, Forked** Figure 4.11 shows the concept of a single 'gearnut' driving a rod which forks into two, and it is on these two arms that the load applicator would be fixed. The advantage of this type of system is there is no possibility of the two arms misaligning with respect to each other, and it also saves space when compared to a system with two separate driven rods (discussed next).

The main disadvantage of this system is the potential instability of the applicator if the rod is loose in the gear, or the gear itself is loose. There is no method of ensuring the loading points remain in the same position on the specimen if any play in the components causes the rod to process around the axis of rotation. A further disadvantage is that this configuration results in the entire applied load being transferred through one point, and any manufacturing or assembly error will result in this load being transferred unevenly to the specimen.

**Double Drive Rods** Figure 4.12 shows the double driven rod configuration, which operates on the same principle as the single rod system described previously, the difference being each side of the load applicator is connected to a rod which is independently driven, as opposed to having a common base.

The advantage this system has over the forked system is that it enables much

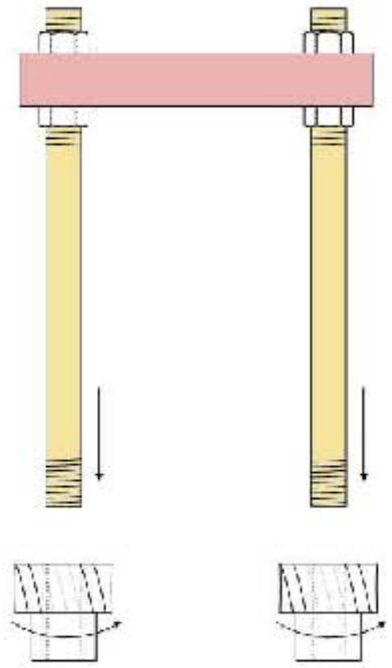

**Figure 4.12:** Independently driven rods displace each half of the load applicator separately.

more even displacement of the load applicator, and hence more even loading of the specimen. If one rod has an eccentric rotation, the second rod can limit this motion. Furthermore, half the total required load is transferred through either rod, and provided each rod 'gearnut' is driven at the same speed, this further ensures even displacement of the applicator. The disadvantage is that this method requires more components in the geared part of the drive, which in turn requires a larger drive housing. This increases the overall size of the rig.

### 4.2.3 Data Output Solutions

There are various options for retrieving load and displacement data from a system such as this. This section describes a few of these options.

#### 4.2.3.1 Load Data

Commercial load cells are available on the market, and obtaining one of these would provide a ready-to-use, pre-calibrated device with no further setup necessary. However, the size limitations imposed by the SEM environment would not necessarily allow for the rig structures to house such a device. An alternative is to place a strain gauged bar somewhere in the loading train, so that any load transferred through it

would result in a deflection of the bar, reflecting as a resistance change in the strain gauges. A bar is capable of being sized and shaped to suit the available layout. A disadvantage would be the additional work required to machine the bar, install the strain gauges, and calibrate the output.

#### 4.2.3.2 Displacement Data

In terms of gaining load applicator displacement, a commercial linear variable differential transformer (LVDT) is a viable option. However, the same comment applies to this as for the commercial load cell option: there is a size limitation, and having a custom method allows one to position components according to the space available.

One such custom method is to use the idea of a strain gauged bar as discussed previously, and calibrate the strain output value from the gauges with a known displacement. The disadvantage of this system is a potential change in the displacement - strain relationship due to creep effects in the bar over time. Using this method would require the bar to be recalibrated at set intervals, or before each course of tests undertaken with the rig, and to monitor the amount by which the relationship changes. Furthermore, the relationship determined would not be completely accurate, as it would only be a reflection of how the bar displaces on its own, without the presence of a specimen in the rig, and other items in the load train. The relaxation inherent in both the specimen and the bar would also call into question the confidence with which one may interpret the displacement data gained using this method.

However, as mentioned in the problem definition, the primary desirable output is displacement *rate*, rather than actual displacement. For this, a more direct method may be used. Provided that the exact reduction between the motorised input and the crosshead is known, the RPM of the drive motor may be monitored and converted to a crosshead displacement rate via the the reduction ratio.



## 4.3 Overall System Solution

Based on the problem definition and the concepts discussed, a model of the final solution for the rig structure is shown in Figure 4.13.

The main rig structure has dimensions $65 \times 90 \times 75\,\text{mm}$, and fulfils the requirements as set out in the preceding sections. The extended system allows for fine speed control over the loading rate, digital recording of the load and displacement rate, and video capture of the SEM VDU display. Additionally, there is space to

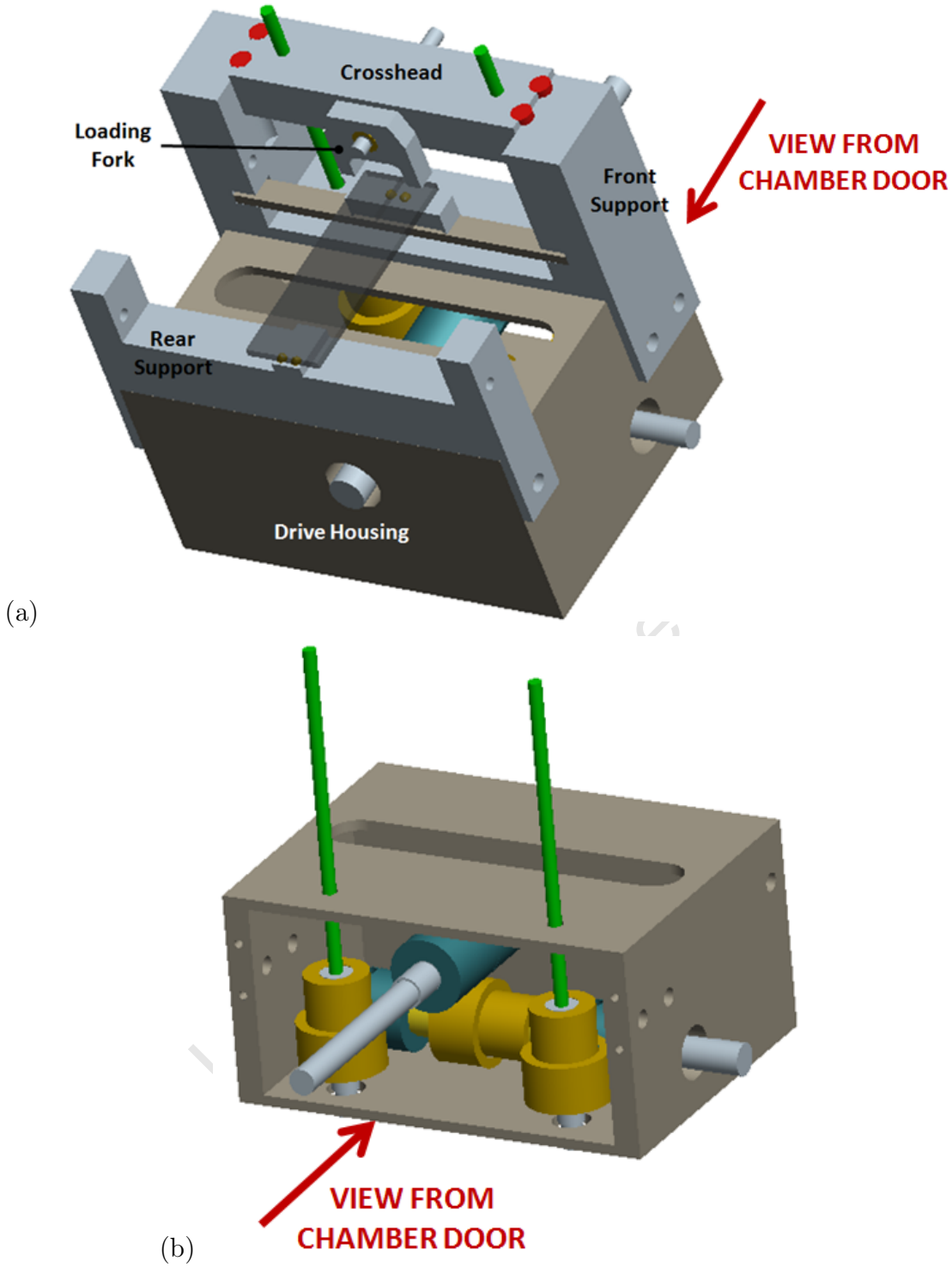


**Figure 4.13:** (a) Rig structure with specimen in place. The drive system shown in (b) draws the crosshead, with load fork attached, downwards, thereby applying load to the upper outer edges of the specimen. The specimen itself is resting on bearing balls located at the lower, inner edges. The input shaft reduction is provided by a series of worms and gears in the drive system.

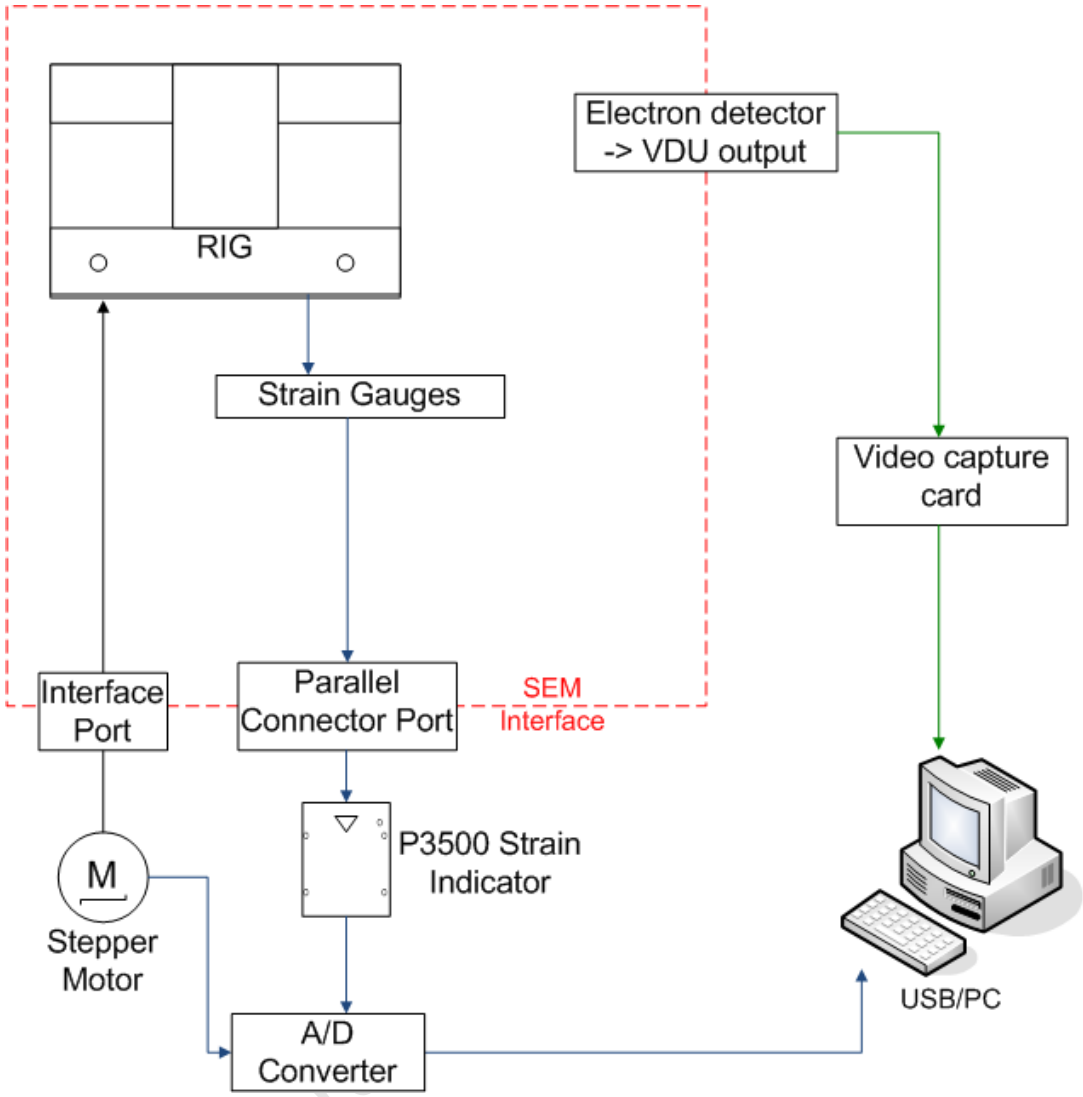


**Figure 4.14:** Schematic of the complete system layout

install a local heating stage below the specimen, should this be required in future work. The following sections describe in detail the various aspects of the design.

A schematic diagram of the entire system is shown in Figure 4.14; for machine drawings, the reader is referred to Appendix A.

The manufacture of the test specimens used is presented in the following sections, as they form an integral part of the system, and were used to evaluate the rig performance, described in the next chapter. Subsequent sections present the features of the rig.

### 4.3.1 Specimen Preparation

Polymethylmethacrylate (PMMA) and nuclear graphite specimens were used with the current system. Specimens from the two types of material were prepared for testing with the system, each having different manufacturing methods. All specimens were manufactured with the same dimensions, nominally 45x15x1.5mm with a 10mm starter notch.

In order to verify that the system worked, PMMA specimens were chosen due to the fact that PMMA has a fracture toughness similar to graphite, and this method has been used with success in the past when testing the macro-system [12]. The transparency of the material also enables one to view the propagating crack with ease, and observe specimen characteristics such as the ability to propagate a straight crack.

Graphite specimens were manufactured from an existing single-edge notched bend (SENB) specimen of grade designation "$S$", as prodvided by the original material supplier. The significance of this designation is unknown, but it has been reported in previous tests using this batch of material that the maximum grain size of this material is in the region of $180 - 200\,\mu$m [78]. The specimens were manufactured from SENB specimen number 123 of the original batch, and as such each DT specimen is referred to as S123_$x$, where $x$ corresponds to the individual specimen number ($x = 1, 2,$ or 3).

The purpose of the graphite specimens was to observe the behaviour of the material under load.

Polycrystalline diamond (PCD) specimens were provided by an outside company in order to use the technology in the current work for their own research purposes. In terms of this project, it was seen as an opportunity to evaluate the system's suitability for use with other materials. The thickness of the specimens, however, meant the load necessary to induce a crack would have been of the order of $\sim$ 400N, which is past the design limits of various parts of the system. Recommended thickness values for PCD specimens having the same general dimensions as used in this work are $0.5 \sim 1$mm.

#### 4.3.1.1 Polymethylmethacrylate (PMMA)

Specimens were cut out of a 1.6mm thick sheet of PMMA, using a $CO_2$ laser cutter. This was all the preparation required for observations done with an optical microscope. For the specimens to be used in the SEM, the surface of this smooth material was degraded slightly in order to produce features, before being coated

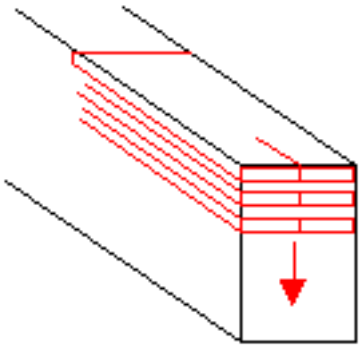

**Figure 4.15:** New specimen configuration within original graphite blocks

with a conductive carbon layer using a Polarin sputter coater with a gold/palladium target.

#### 4.3.1.2 Graphite

Graphite specimens were machined out of an existing SENB specimen, as mentioned, having original dimensions 15x20x100mm. The new specimens had dimensions 15x45x1.5mm and were machined out of the original block in the configuration shown in Figure 4.15.

$CO_2$ cutting was not suitable due to the nature of the particular cutter at UCT. Wire cutting was also attempted, but proved unsuccessful. The specimens were instead carefully machined by hand using a Buehler IsoMet diamond bladed circular saw. One surface was then polished using a 3$\mu$m diamond abrasive polishing pad. As graphite is a conductive material, no further surface preparation was required for use inside the SEM.

### 4.3.2 Specimen Mounting

The specimens are mounted on bearing ball supports at the front and the rear of the rig. These supports are in line with the 'inner' edges of the specimen, i.e. closest to the notch. This was done in order that the tensile face occurred on the top of the specimen. Location screws which screw in each side of the front and rear supports enable one to fine tune the lateral position of the specimen, so as to make sure it is aligned symmetrically with respect to the loading point.

The position of the specimen on the rig is such that the y- movement of the SEM stage is parallel to the crack propagation direction.

### 4.3.3 Load Application

Load is applied to the 'outer' edges of the specimen via a loading fork, which is in turn mounted to a driven crosshead. The crosshead is attached to two M3 threaded guide rods, which are fed through two 'gear nuts' in the drive system below. As the gear nuts rotate, the threaded shaft is drawn down through the gears, which draws the crosshead down. This was considered to be a good amalgamation of the ideas of Salem [10] and Tait [50], presented in Section 4.2.2.1. The independent driven rods were chosen over the single rod concept due to the more even load distribution capability; it was found that the added components did not enlarge the size of the rig to past the dimensional limits given in the problem definition.

Various systems are in place to ensure symmetrical loading. The two M3 rods are located evenly to each side of the loading fork, and the crosshead itself is situated between the two arms of the front support, and slides along guide pins mounted in the support. Added to this, the load fork is mounted on a brass bush, and as such is free to rotate about its own axis, ensuring load is distributed evenly on either side of the specimen.

### 4.3.4 Data Output

Load data is retrieved from the system by means of interchangable strain-gauged bars on which the bottom of the specimen mount rests. A bar is configured such that it is loaded in four point bending, and exhibits a constant moment region between the two centre load points (refer forward to Figures 5.1 and 5.2). The 120Ω strain gauges were wired in a half Wheatstone bridge configuration, and connected to a strain indicator (Vishay Measurements Group P-3500), which displays a strain value in microstrain. As well as the display value, the indicator also outputs a voltage, which was calibrated to register 0.465mV per microstrain. Different "load cell" bars may be configured for materials of different strength. A material with a higher fracture toughness requires a stiffer bar, which is able to minimise deformation under loading, yet still be sensitive to small loading increments. Different thickness bars are a compromise on these two considerations, and for the current work a 4mm thickness bar was used.

This analog output was connected via a 12-bit National Instruments USB-6008 data acquisition card (DAQ) and fed into a PC. The data was read, logged, and processed using National Instruments LabVIEW SignalExpress software. Due to the quasi-static nature of the loading, the raw voltage data was filtered to pass frequencies below 5Hz only. This filtered signal was then converted back to microstrain

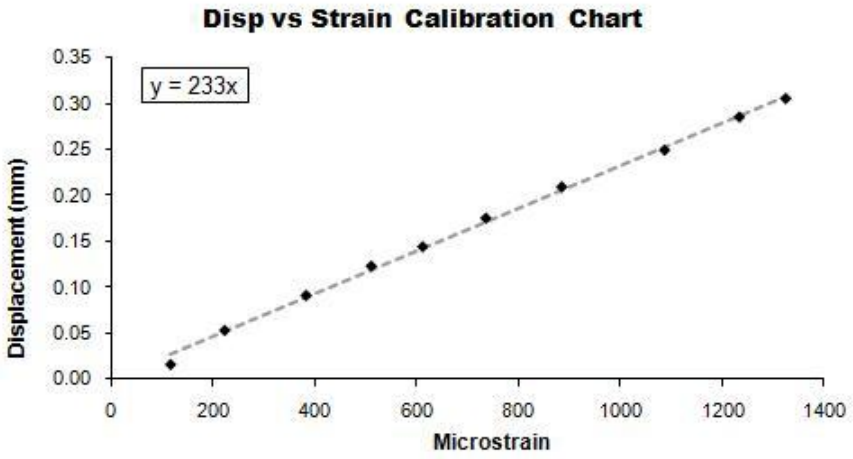


**Figure 4.16:** Calibration relationship between strain and displacement for $t = 4\,\text{mm}$ strain bar.

via the voltage-microstrain calibration relationship, and then further converted to a force reading by means of the strain bar calibration relationship (see Section 5.1).

This setup is also capable of retrieving displacement data via the same strain-bar calibration method, where there is an already established relationship between strain and vertical displacement, shown in Figure 4.16. This relationship was derived via the calibration method discussed in Chapter 5, although for the reasons articulated in Section 4.2.3, it is advised this data be interpreted with caution, and an understanding of the mechanisms at play.

The speed of the motor was gained via tapping a small amount of current from one of the transistors on the stepper motor control board and directing it through the DAQ to a frequency counter function in SignalExpress. Knowing that the stepper motor used has 4 coils, that each coil is energized via a separate transistor switch, and that with the current connection a coil is energized 12 times per revolution, the frequency of the energization cycles of one transistor may be converted to RPM via the following equation:

$$\omega = \frac{60}{12} \cdot f \tag{4.1}$$

where:

$\omega$ is the number of revolutions of the motor per minute, and

$f$ is the frequency of activation of one motor coil transistor.

The connection diagrams for the data inputs to the DAQ are given in Appendix B.

### 4.3.5 Material Choice

Material choice was fairly important in this system, as any materials employed had to be free of magnetic fields. Grade 316 stainless steel and Series 6 aluminium were chosen for this reason. The general structural elements were fabricated from aluminium, in order to keep the rig lightweight. The more 'functional' elements, such as the gear shafts, were manufactured from the stainless steel. Grade 316 was chosen over the less costly Grade 304 as machining could render SS304 magnetic.

The gear shafts were mounted on bearings which were thoroughly degreased before installation in the SEM, due to the vacuum integrity issues mentioned previously. The parts were cleaned in an ethanol solution placed in an ultrasonic bath for one hour. The bush upon which the loading fork is mounted was machined out of brass.

Note that each of these materials is conductive, providing a leakage path to earth. This is especially important for structures close to the desired area of observation, such as the loading fork and the shaft it is mounted on. In a previous iteration of the design which saw Teflon bushes being used instead of bearings, the loading fork bush was kept as brass for this reason. In this previous design, even though Teflon is a non-conductive material, the location of all the components was such that there was still an unbroken leakage path from all areas that would be impinged on by electrons.



### 4.3.6 Drive System

Motion is actuated by a 7.5° stepper motor, which then undergoes a 400:1 speed reduction before being transferred to the 'gear nuts' mentioned earlier.

Figure 4.13 (b) shows the layout of the worms (blue) and gears (gold) inside the drive housing. The final driven gears have a machined insert with a female thread placed inside the bore, into which the M3 threaded rods (green) which drive the crosshead were screwed. When these gears are driven, they draw the threaded rods through the insert, which in turn raises or lowers the attached crosshead.

The input shaft speed is reduced via two 20:1 worm/gear pairings, resulting in the aforementioned 400:1 speed reduction. Additionally, the pitch length of the M3 threaded rods is 0.5mm. This means that for every revolution of the input motor, the crosshead is drawn down 1.25$\mu$m. This distance reduces to $\sim 0.03\mu$m per step if the motor is stepped forward. The relationship between crosshead displacement

$x$ and number of revolutions of the motor $N$ is given as:

$$x = \frac{0.5 \times 10^{-3} \cdot N}{400} \tag{4.2}$$

In this instance, for a 7.5° motor, the above relationship can be divided by 48 to achieve the distance per step.

The 5V, 5Ω stepper motor is driven by a transistor-based control circuit, which energizes each of the four motor coils in sequence. The base current for the transistors and the board is provided by a 9V battery, while the collector current is provided by the 5V USB supply on a PC.

The control circuit has two modes of operation: internal and external. Internal supply rotates the motor continuously, at a speed and direction determined by switch settings on the board. External supply allows for PC control, or an external circuit, and in the current configuration is connected to a timer circuit which provides a clock pulse, enabling one to pulse the motor in a given direction via a push button (Figure B.2). While there is an in-built 'step' function on the original board, it was found that this was highly susceptible to ambient noise; for this reason, the external timer circuit was employed.

The associated circuit diagrams are given in Appendix B.

### 4.3.7 Interfaces

Various sub-systems needed to be connected, in some instances across the 'line' of vacuum integrity within the SEM chamber, as shown in Figure 4.14. The following paragraphs describe the interfaces between the rig/SEM, SEM/motor, strain gauges/indicator, and VDU/capture systems.

#### 4.3.7.1 Rig/SEM

The rig was attached to the SEM stage via the brackets upon which the rotate/tilt mechanism is usually bolted (see item 1 in Figure 4.17). The bolt holes on the underside of the rig were spaced to fit these brackets.

The input shaft on the rig was connected to an existing spare shaft within the door of the SEM (item 2), which is ordinarily attached to a hand control on the exterior side through a vacuum port and universal joint arrangement. The coupling from the spare shaft to the rig input shaft was also via a universal joint, which resulted in a double universal joint arrangement. This allowed for a greater degree of misalignment between the two shafts, while also providing constant velocity motion

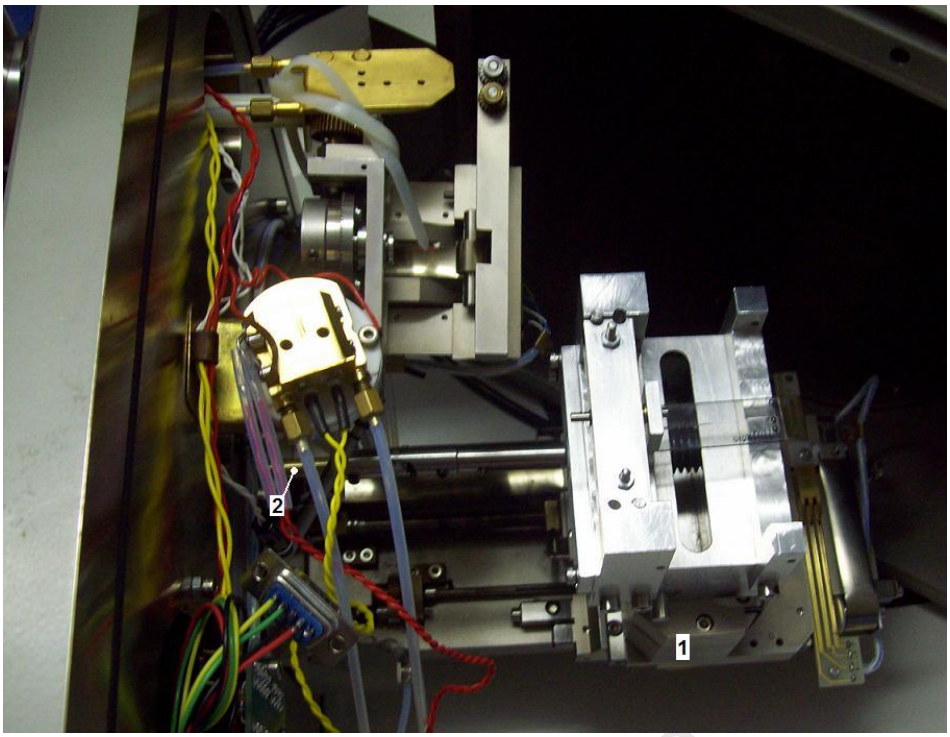


**Figure 4.17:** Interior rig configuration

between the hand control input and the rig input shaft. This was necessary to ensure continued smooth operation when the rig was shifted in the x- and y- directions during operation.

A range of y- motion of the rig was enabled via a telescopic attachment between the universal joint and the input shaft. The current setup allows the rig to position the specimen at its furthest approximately 32mm before the electron beam; this means that on a specimen with an initial notch of 10mm, one can follow a crack for 22mm before running out of travel. This takes the 45mm long specimen to approximately the end of the 'constant $K$' regime of crack growth.

#### 4.3.7.2 SEM/Motor

The motor was coupled to the exterior side of the spare shaft mentioned under the previous heading. After an attempt at a rigid coupling arrangement, it was noted that it is difficult to achieve a good enough alignment between the motor and shaft to prevent excessive play. A one-piece flexible coupling was then installed, but problems with locating the SEM shaft in place against the interior vacuum conditions forced the current solution, shown in Figure 4.18.

In this solution, the original hand dial was kept in place, as it locates the shaft


**Figure 4.18:** SEM-Motor coupling arrangement. An aluminium bracket and brass spacer mount the motor on to the door at the correct distance. Silicon tubing transmits motion between the motor and SEM shafts, both of which have dials attached for shaft location reasons.

and prevents it from being sucked into the chamber under vacuum. A dial of similar size was attached to the motor shaft, and a piece of silicon tubing was mounted between them. The tubing provides a decent amount of flexibility in the case of misalignment between either shaft, while remaining rigid enough to transmit the required torque.

The entire motor assembly was mounted on to an aluminium bracket which bolted onto the SEM door.

#### 4.3.7.3 Strain Gauges/SEM

The strain bar gauge wires were soldered onto a 9-pin D-sub connector (old parallel port connectors) and plugged into the existing 25-pin connector inside the door of the SEM, for which an 9- to 25-pin adapter was made (see Figure 4.17, bottom left). A matching plug was made for the connector outside the door, which had wires leading to the strain indicator. The indicator output connected to the DAQ, via a BNC-type connector on the indicator, and loose positive and negative wires which were fitted to the screw terminals on the DAQ. The DAQ then connected via USB to a PC.

#### 4.3.7.4 VDU/Capture System

Dynamic images were recorded via an external USB EasyCAP capture card, with Ulead VideoStudio software. The capture card received its signal from the image converter attached to the SEM. The PAL output on the converter was used, and a cable with BNC & RCA connectors was used between the two devices.

## 4.4 Summary

This chapter has covered the designed of the mini-DT device to be used *in situ* in the SEM, as well as the development of the peripheral systems involved in motion control, data capture, and video recording.

Before the device was installed in the SEM, an inital evaluation was undertaken in order to assess whether the design and build quality were suitable for the intended application. The following chapter presents the outcome of this evaluation and assessment.

# Chapter 5

# Initial System Evaluation

In terms of the performance requirements set out in Section 4.1, various criteria were defined as being able to show whether the device was performing adequately. The evaluation in this context was limited to testing of the mini-DT rig on the bench, in order to check that the physical device was manufactured and assembled as designed, and that it and any other applicable affiliated systems were performing as required. The methodology and results of that initial evaluation are presented here, with a discussion as to the suitability for use of the rig *in situ*. The results here also contribute to the overall discussion of system performance (Chapter 7), which was compiled after gaining experience with the rig in the SEM.



## 5.1 Strain Gauge Based Load Cells

The calibration of the strain gauge based load cells was done by comparison of actual strain readouts corresponding to known loads. However, before that process is described, a brief description of the theory governing the strain-load relationship in a four point bending beam is presented.

Consider the strain bar in question, having dimensions and applied loads as shown in Figure 5.1. Loading is simple four point bending, with reaction forces equal to loading forces, in concurrence with the theory of a beam in equilibrium.

The moment diagram for a bar in this configuration is shown in Figure 5.2. Note the region of constant moment between the two load application points **B** and **C**. It is this behaviour which enables this bar to serve as a simple load cell. The moment, taken from the left of the bar, is the value of the applied load at **B** acting at a

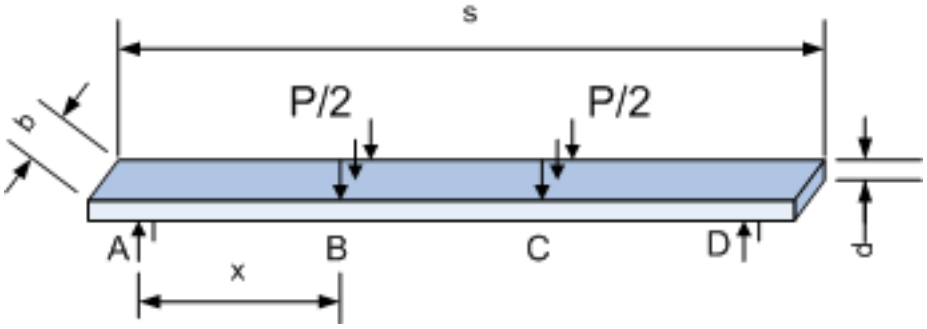


**Figure 5.1:** Strain gauge based load cell

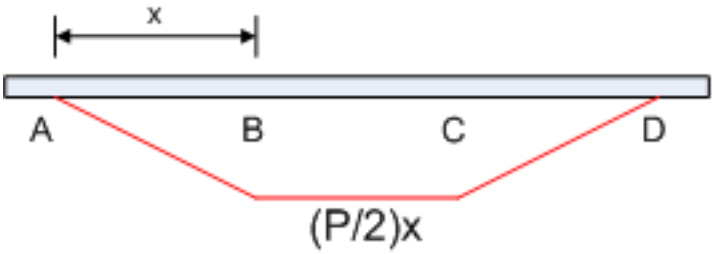


**Figure 5.2:** Moment diagram for strain bar in four point bending

distance from the initial support point, **A**. Mathematically,

$$M_B = (P/2)\, x \tag{5.1}$$

Operating under the assumption that the stress induced in the bar is entirely due to the bending action of the applied moment in Equation 5.1, then the total stress on the surface of the section BC may be given by:

$$\sigma_{BC} = \frac{My}{I} \tag{5.2}$$

Where $y$ and $I$ are values which are dependent on the specimen geometry.

$y$ is the distance from the point of maximum bending stress (i.e. the surface) to the neutral axis of the bar. That is, where the action of the stress changes from tensile to compressive. In this case, the bar being symmetrical, $y$ has a value $d/2$.

$I$ refers to the second moment of area, and for a rectangular cross section this is given by $I = \frac{bd^3}{12}$.

We are also reminded of the relation between stress and strain:

$$\sigma = E\varepsilon \tag{5.3}$$

Therefore, substituting Equations 5.1 and 5.3 into Eq. 5.2, and rearranging, one is left with:

$$\begin{aligned} {}^{P}/_{2} &= \left(\frac{E \cdot \frac{bd^3}{12}}{\frac{d}{2}}\right)\varepsilon \\ P &= \left(\frac{E \cdot bd^2}{3}\right)\varepsilon \end{aligned} \tag{5.4}$$

Equation 5.4 describes the theoretical relationship between load and strain for a bar in four point bending, which is clearly linear. What is important to note however, is that this equation is only valid for elastic deformation of the bar. Also, experimental results have been known to differ from this theoretical prediction due to the assumption made by St Venant's principle, being that the effect of the deformation due to point loading is negligible in the overall analysis of the system, if one considers a point far enough from the point load.

The method for determining the practical limit of elasticity for a bar in four point bending, on a purely theoretical basis, is given thus:

Consider the yield strength of the strain bar material, $\sigma_y$. Taking a conservative value of 75% of yield, and equating this to the expression for stress in the bar, Equation 5.2, gives:

$$0.75\sigma_y = \frac{\frac{P}{2}x \cdot \frac{d}{2}}{\frac{bd^3}{12}}$$

Rearranging for **P**, and designated it $P_{peak}$ as we are regarding the maximum load applicable before plasticity:

$$P_{peak} = 0.25\frac{\sigma_y \cdot bd^2}{x} \tag{5.5}$$

Given the above theoretical relations, their overall validity was determined via experiment.

### 5.1.1 Methodology

The strain-gauged bar of interest was loaded into the miniature DT rig, as if in preparation for actual use, and the gauges were connected to a Vishay Measurement Group P-3500 strain indicator in a half-bridge configuration. Using the ZWICK Universal Tensile Tester housed in the Centre for Materials Engineering (CME) at the University of Cape Town, known loads were applied in suitable increments up to the peak load as determined by Equation 5.5. The setup is shown in Figure 5.3.


**Figure 5.3:** Setup for the evaluation of the strain bars. A cylindrical grip is attached to the crosshead of the Zwick tensile/compression machine, and brought to bear down on the front specimen support through which load is transferred to the strain bar beneath. The bar is just visible resting inside one of its support grooves. Also visible are the wires connecting the gauges to the strain indicator.

The load vs strain data plot was examined for linearity, and deductions were made about the suitability of the bar for material testing.

Two types of load cell bar were constructed for this project, both having dimensions $70 \times 5 \times t\,\text{mm}$, where $t_1 = 2\,\text{mm}$, and $t_2 = 4\,\text{mm}$. The idea behind the load cells was that they are interchangeable, depending on the type of material being tested. For a more compliant specimen with a low fracture toughness, a thinner bar would be used, as opposed to when testing a relatively stiff material with a higher toughness value. There is an attempt to compromise between the range of strain values exhibited over the loading range of the material, and the compliance of the strain bar itself.

The concept identified interchangeable strain gauged bars suitable for use as load cells, measuring the applied load transferred through the specimen. Such bars had to satisfy the following criteria:

- Must present an identifiable relationship between stress and load.
- Must present a large range of strain values within specified material load ranges; in-house wisdom dictates a sensitivity of approximately $1000\mu\varepsilon$ at

**Table 5.1:** Parameters of Strain Bars

| | $s$ | $b$ | $x$ | $d$ | $P_{peak}$ |
|---|---|---|---|---|---|
| $t = 2$mm | 70mm | 5mm | 25mm | 2mm | 62N |
| $t = 4$mm | 70mm | 5mm | 25mm | 4mm | 248N |
| Material: Key Steel, AISI 1055 | | | | | |
| $\sigma_y = 310$MPa, $E = 200$GPa [79, 80] | | | | | |

**Table 5.2:** Calibration Values for Strain Bars

| Thin bar $t = 2\,$mm | | Thick bar (1) $t = 4\,$mm | | Thick bar (2) $t = 4\,$mm | |
|---|---|---|---|---|---|
| Applied Force (N) | Recorded Strain ($\mu\varepsilon$) | Applied Force (N) | Recorded Strain ($\mu\varepsilon$) | Applied Force (N) | Recorded Strain ($\mu\varepsilon$) |
| 2.4 | 87 | 0.5 | 7 | 6.4 | 65 |
| 6.3 | 220 | 12.0 | 126 | 11.5 | 116 |
| 11.6 | 398 | 29.5 | 306 | 22 | 222 |
| 16.7 | 572 | 57.0 | 593 | 38 | 382 |
| 22.4 | 768 | 85.0 | 890 | 50 | 510 |
| 33.7 | 1148 | 100.0 | 1044 | 60 | 611 |
| 38.8 | 1343 | 141.0 | 1490 | 71 | 735 |
| 45.3 | 1573 | 193.0 | 2048 | 85 | 884 |
| 50.2 | 1752 | | | 105 | 1086 |
| 54.75 | 1918 | | | 117 | 1233 |
| 60.8 | 2143 | | | 125 | 1324 |

peak load is suitable.

- Must be able to resist plastic deformation to peak load.

### 5.1.2 Results

The parameters of the load cells tested are given in Table 5.1, where the dimensions refer to Figure 5.1, and the $P_{peak}$ value was calculated according to Equation 5.5.

Two thick strain bar tests were done, as a result of having to reapply strain gauges to the thick bar after the previous gauge wires had snapped. It was considered of value to note the difference between the two sets of results, and present them here, as a way of discerning whether the Force - Strain relationship was highly sensitive to the accurate positioning of the gauges. The testing was done in accordance with the procedure described in the previous section, and the results gained for all three tests are given in Table 5.2.

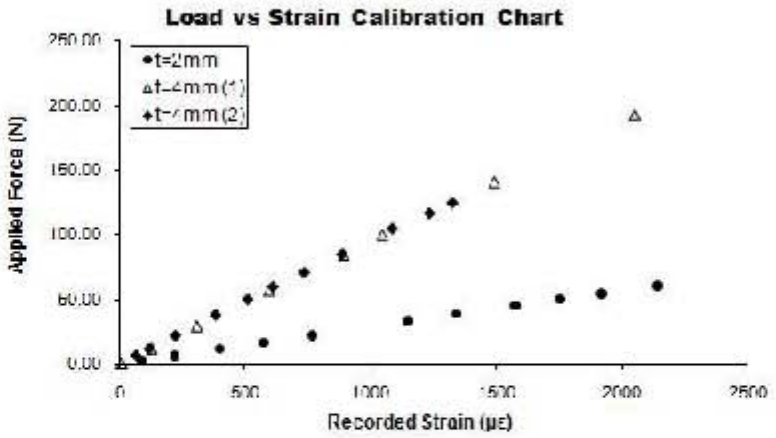


**Figure 5.4:** Comparison of calibration data between different thickness load cells

**Table 5.3:** Calibration relationships for $t = 2\,\text{mm}$ and $t = 4\,\text{mm}$ strain bars

| | $t = 2\,\text{mm}$ | $t = 4\,\text{mm}$ |
|---|---|---|
| Calibration equation | $P = 28483\varepsilon$ | $P = 94480\varepsilon$ |

Figure 5.4 plots the values of Table 5.2 for the three strain bars, alongside the theoretical Force-Strain relationship gained using Equation 5.4.

The figure shows the results of three different strain bars which were made for this rig; the equations for the two distinct results are shown in Table 5.3, calculated from the values set out in Table 5.2.

Both bars exhibited a linear relationship between load and strain, as predicted by Equation 5.4. As is seen in the graph, the 2mm thick bar exhibits a markedly lower stiffness than the 4mm bars, and it was found that the displacement behaviour inherent in this thinner bar contributed to unstable crack growth in test PMMA specimens; a behaviour not seen with the 4mm bar. The reason may be gleaned by examination of the force-displacement relationship in terms of the energy available for crack growth.

Refer again to Figure 5.5. In the figure, a hypothetical load of 50N is imposed on both types of bar. Assuming a crack in a specimen propagates with some velocity at this load, there is then a certain amount of load relaxation as the compliance of the specimen increases with the extending crack. For a specimen load relaxation due to crack propagation of 5N, from 50N - 45N, displacement of the strain bar then decreases by an amount represented by the width of the coloured sections in Figure 5.5, taking the specimen load down past the threshold that would cause crack propa-

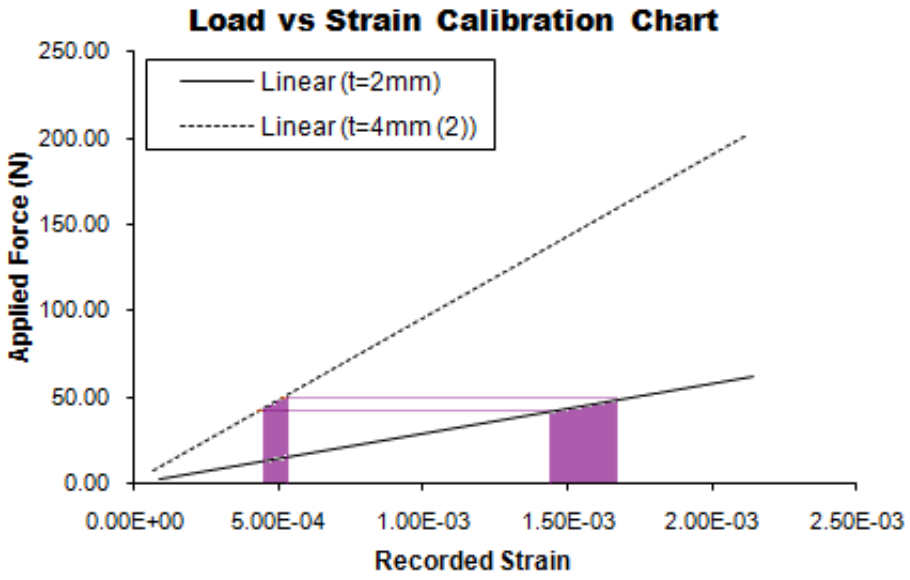


**Figure 5.5:** Examination of force-displacement behaviour in different thickness strain bars. The same amount of specimen relaxation produces markedly different energy reductions in each bar.



gation.[1] The area under the curve between the two displacement points is indicative of the energy transfer in moving the system from one state to the other; potential energy is taken from the load system and partly converted to vertical displacment of the strain bar (the rest being given over to crack propagation), while a decreasing displacement correlates to energy being *released back* to the loading system. Since the loading apparatus is non-compliant when compared to a DT specimen, the decreasing displacement of the strain bars releases energy to the specimen which may be used in the formation of crack growth.

A decrease of 5N in relaxation corresponds to an energy release in the thin bar of the order of approximately 4× that of the thicker bar (see Section C.2.1 for calculations). This added energy, if past the strain limit of the uncracked material, would propagate the crack further, and if enough energy was supplied, the propagation would proceed uncontrolled. This is demonstrated in the following section on the evaluation of the rig structure.

[1] Although the horizontal axis in the figure represents strain values, the strain in a bar undergoing four point bending is directly related to vertical displacement of the loading points. The force - strain plot is therefore representative of the force - displacement relationship and is used here for illustrative purposes.

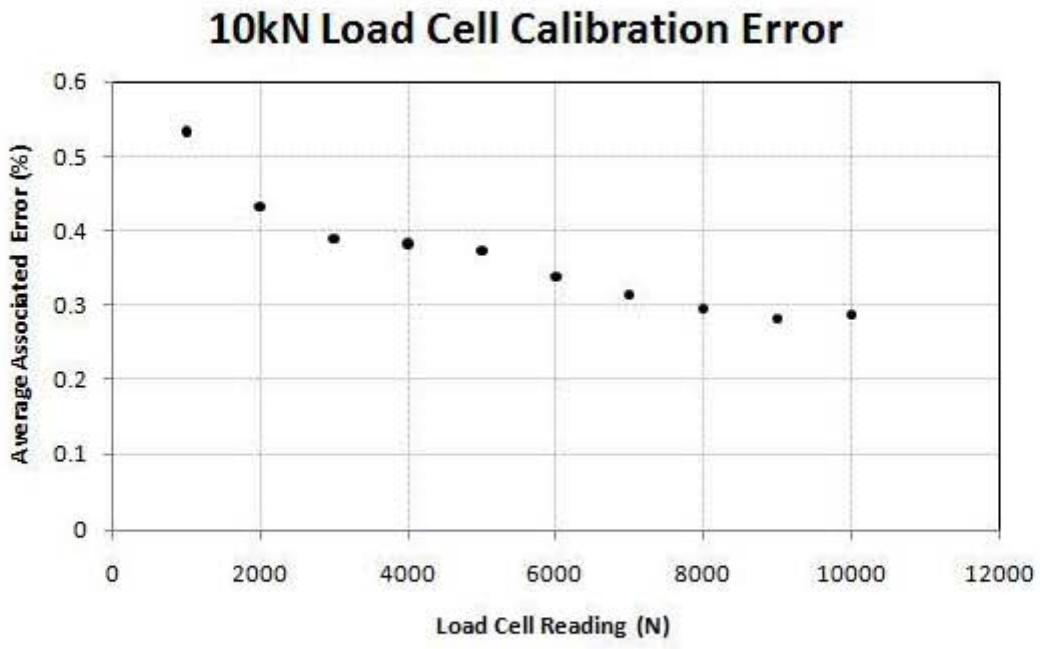


**Figure 5.6:** ZWICK 10kN load cell calibration error, based on data from calibration certificates as provided by CME Metrology cc [81]

### 5.1.3 Discussion

The results in the previous section show a good linear correlation between load input and strain output. This, together with the fact that the calibration was performed in an entirely stable manner, free from intentional hysteresis, would suggest that the curve resulting from the calibration exercise may be used with confidence. However, due to the fact that the ZWICK 10kN load cell (smallest available) was used to assess applied loads within the region of $0 \sim 60$N, the error in this load cell bears analysis. Figure 5.6 shows a plot of the average error associated with the load cell at the last calibration. It can be seen that the error associated with the readings is larger for smaller applied loads. The smallest value available is at 1000N, with an associated error or 0.533%, or 5.33N. Notwithstanding the observation that the error shows an exponential trend at decreasing load levels, and would therefore be higher than the value as quoted at 1000N, an error of $\sim 5$ N is still approximately equivalent to the intervals of load application as seen in Table 5.2.

As the strain bar calibration output was linear and well behaved, it was utilised in further experiments, but readers and other users should apply a certain amount of caution when interpreting load results.

As for the behaviour of the strain bar itself, and its performance during initial

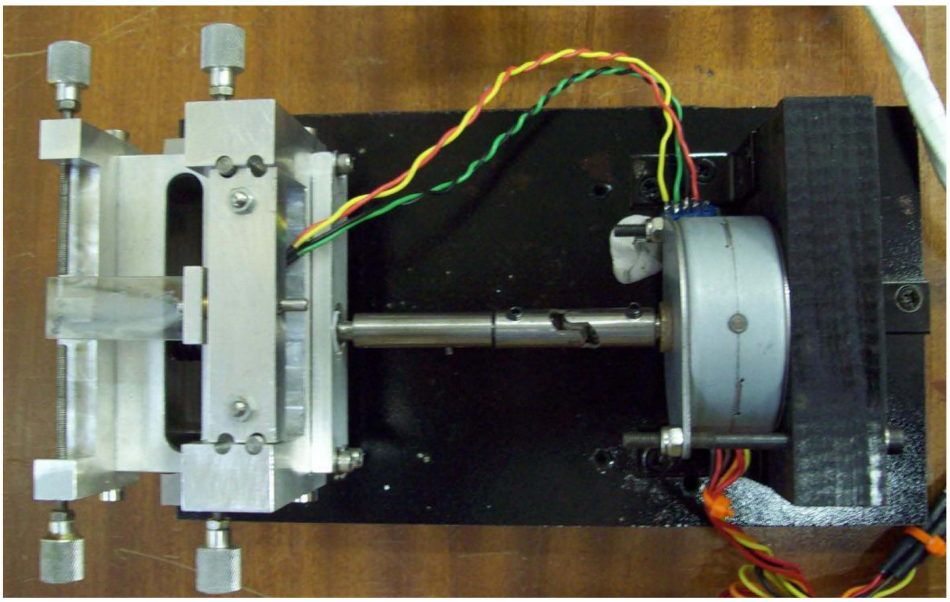

**Figure 5.7:** DT Rig: Bench testing configuration

experimental testing with PMMA, it was discovered that the small thickness made the bar overly compliant. This manifested itself in an inability of the rig to produce stable crack growth in the PMMA specimens (see Sections 5.2.2 & 5.2.4). The thicker bar was used in all subsequent work.

## 5.2 Rig Structure

The PMMA specimens were created to verify the performance of the rig, and its ability to grow a straight crack. As such, the majority of the specimens were subject to bench testing under an optical microscope, with the rig in a 'bench configuration' as shown in Figure 5.7

### 5.2.1 Methodology

The specimens were loaded into the rig, ensuring the notch was located in between the two ball bearing spherical supports at either end of the rig. The motor was driven forward until the upper loading points were just touching the specimen, and at this point any final adjustments to the position of the specimen were made.

The motor was then run forward in set intervals, which were determined by the reading on the strain indicator; every 50 microstrain, the loading was halted and an image taken with the microscope camera. Note that only the strain indicator was

connected at this stage, and recording of the load applied was done by noting the strain output and determining the corresponding load via the relationship derived in the calibration of the load cells. The purpose of this testing was to ascertain whether the rig could successfully propagate a stable crack, and to assess the alignment of the crack produced.

### 5.2.2 Crack Stability

Figure 5.8 shows two images propagated on the 2mm load cell, taken at approximately 50 $\mu\varepsilon$ apart (before relaxation), which corresponds to a load of 1.42 N. Here, the specimen did not develop a crack in the entire microstrain range from 0 - 1050 ($\sim$ 29.9 N), and then suddenly an unstable crack propagated once the load had just passed the 1050 $\mu\varepsilon$ step.

Figure 5.9, on the other hand, shows two images taken at 10$\mu\varepsilon$ steps apart. This test was run with the thicker load cell mounted, and as such the 10 microstrain steps correspond to load intervals of 0.94 N. In the first image, taken at a load of 23.6 N, there is an existing crack which has extended approximately 0.7mm from the notch tip. By the following load step ($\sim$ 24.5 N, from the relevant equation in Table 5.3), it has grown a further 0.3mm in a stable manner. This seems to confirm the statements in the previous section on the behaviour of a more compliant strain bar; the thinner bar in this case could not produce a stable crack in the PMMA specimens, whereas the thicker bar was able to. As PMMA is representative of graphite in terms of fracture toughhness, the thicker bar was used for the graphite SEM testing.



### 5.2.3 Crack Skewness

Three specimens that were cracked under the microscope in bench testing were evaluated in terms of the deviation of the crack from the intended longitudinal path. In each case, taking the final image of the cracked specimen, the centreline was identified, and any deviation of the crack tip from this line was measured.

The recommended limit for crack skewness is that the deviation from the centreline, $a_{off}$, should be no more than $W/8$ at any point within the middle third of the specimen (Section 3.1.3). For a specimen with $W = 15$ mm, $a_{off} = 1.875$ mm.

Figure 5.10 shows three different specimens which have been cracked to approximately 40% of the specimen length. In each case, the centreline of the crack has been indicated, and a dimension marker (scaled to correct specimen dimensions)

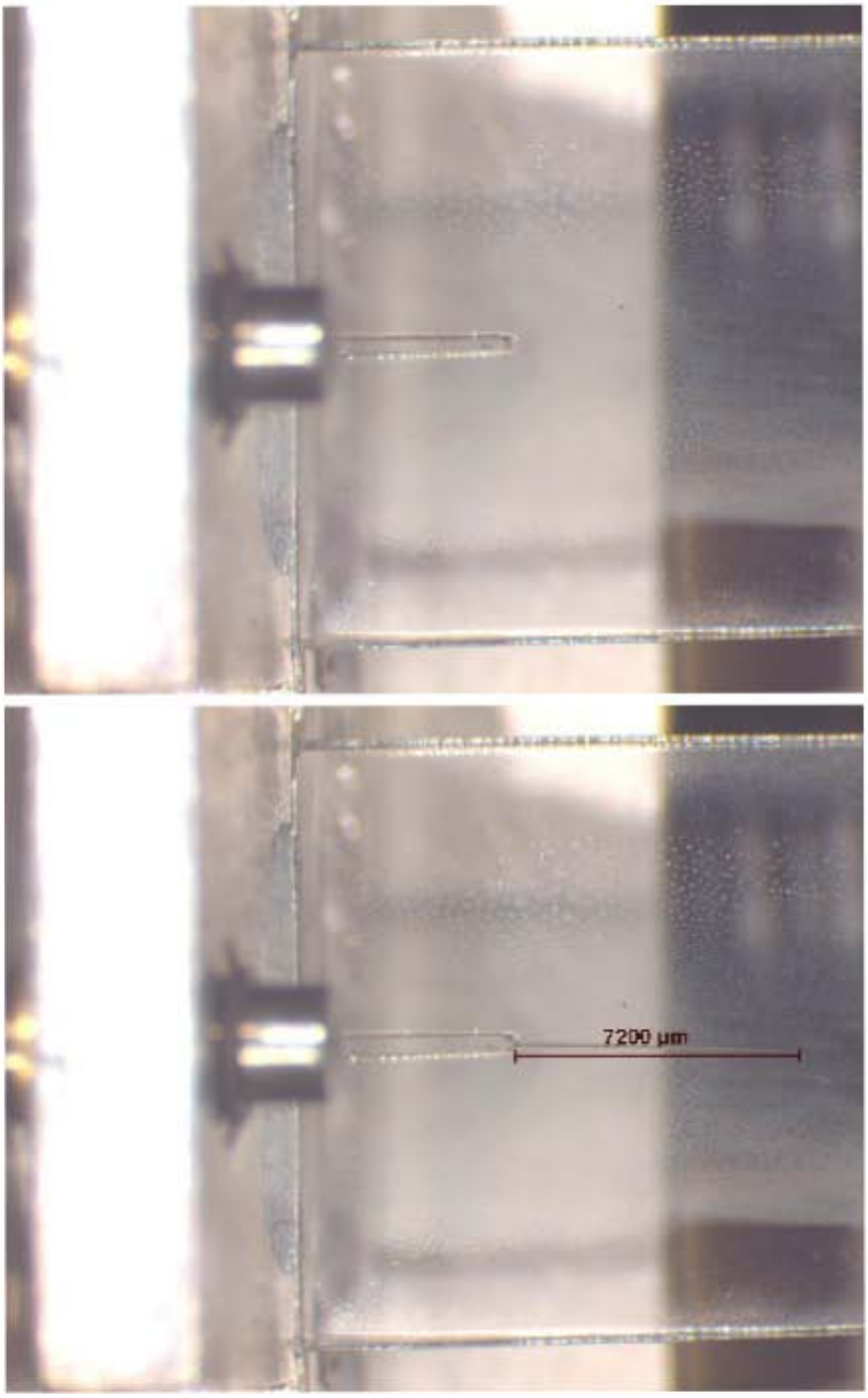


**Figure 5.8:** Optical microscope observation of loading of a PMMA specimen on the $t = 2\,\text{mm}$ strain bar. The load interval between the two images is just under $\sim 1.42\,\text{N}$. Upon application of load to the specimen in the first state, a crack appeared and propagated uncontrollably until the load could be removed. The final crack length of 7.2mm is indicated in the second image.

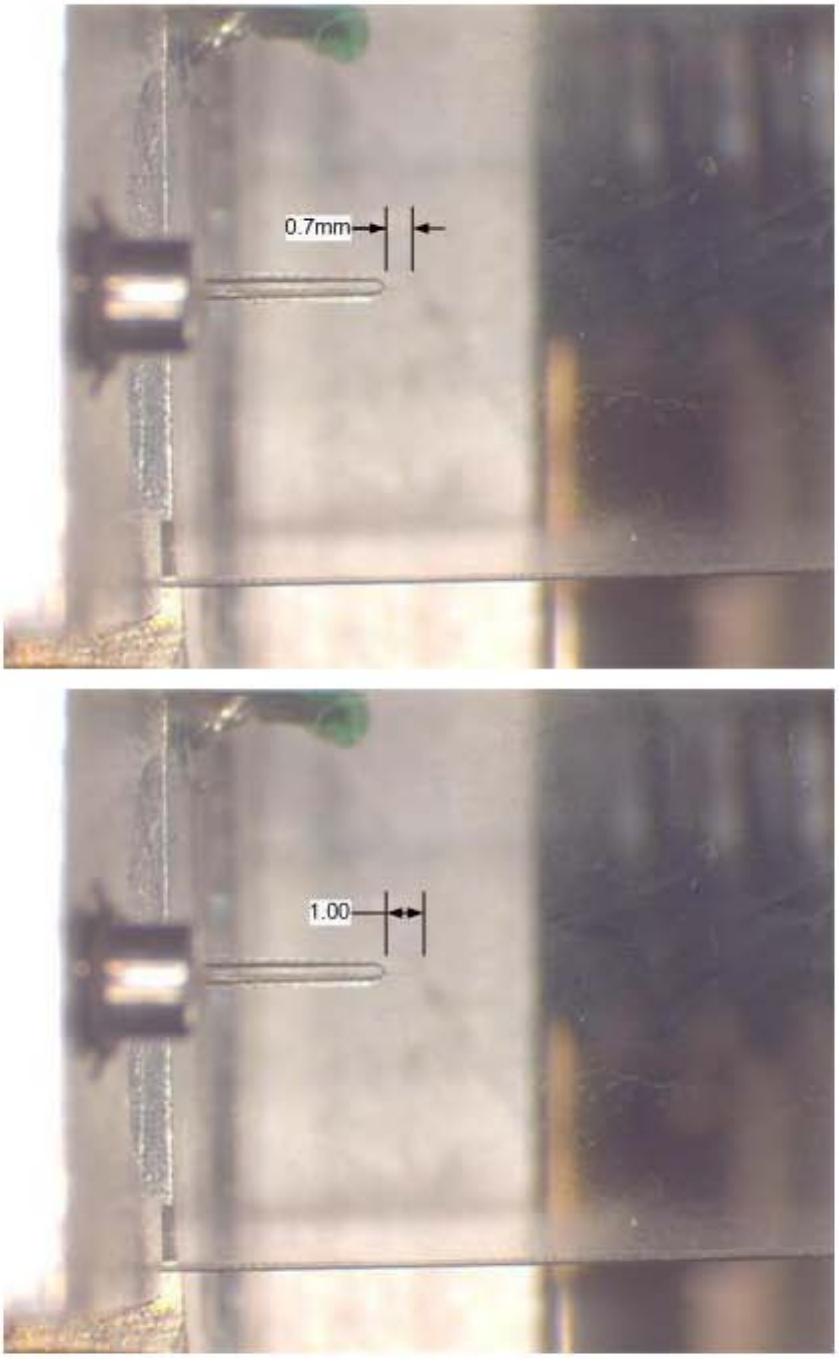


**Figure 5.9:** Optical microscope observation of loading of a PMMA specimen on the $t = 4\,\text{mm}$ strain bar. Load interval between the two images is $\sim 0.94\,\text{N}$.

placed between the crack tip and the centreline. The maximum diversion measured in each specimen was below the 1.875mm limit. This did not confirm, but did suggest strongly, that the rig was of sound construction, and did not have any serious error or misalignments which noticeably affected the crack propagation direction, even with the hand alignment method currently employed.

### 5.2.4 Discussion

The rig, together with the thicker load cell, showed a clear ability to propagate an induced crack in a controllable fashion. This was shown by the small but measurable crack growth between load steps, where the crack did not proceed unstably. This raised confidence that the rig could induce crack growth slow enough to be undetected by the naked eye if the motor step function were to be used. This would be verified in the electron microscope aspect of the testing.

In the crack skewness experiments, all specimens showed the crack remaining within the $a_{off} < {}^{W}/_{8}$ skewness limit. However, there is little further information one can use to predict further displacement of the crack, and the problem with it is that the skewness effect often becomes exaggerated the further down the specimen a crack propagates. That is, once the crack has distorted slightly away from the centreline of the specimen, there is then one narrower (and one wider) ligament to each side of the DT specimen. The narrower ligament experiences a greater stress due to the stress distribution of the applied load, and the crack is further deflected as explained in Section 3.1.3. This deflection quickly becomes more pronounced, causing the crack to emerge from the sides of the specimen instead of the opposing longitudinal end. While this did not happen with the three specimens that were bench tested, it could not be discounted as none of these specimens cracked to complete failure. What is encouraging is that the cracks remained well within the 1.875mm allowable limit for the length tested, up to 40% of the specimen length, for all three specimens tested. These comprised the sum of the bench test observations; no other specimen tests were conducted and/or discounted for any reason. This consistency provides further evidence of the reliability of the rig in its ability to propagate a straight crack.

With regards to the suitability of the observed performance for SEM work, fracture toughness testing remains valid regardless of the eventual crack deflection behaviour as explained in Section 3.1.3. Slow crack observations in the SEM also do not rely on accurate stress intensity calculations as much as Velocity - Stress Intensity (v-K) experiments, and as long as the field of view may be adjusted to

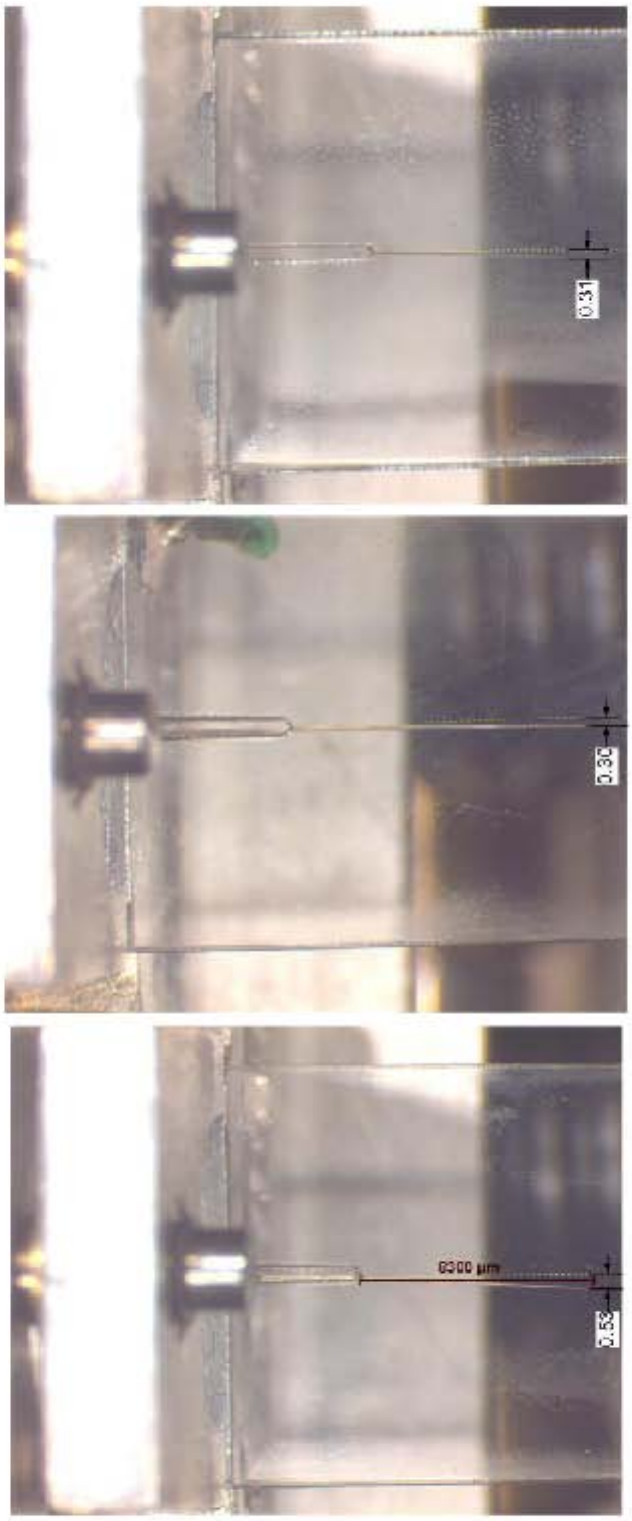


**Figure 5.10:** Crack skewness measurements for PMMA specimens

**Table 5.4:** Comparison of theoretical and observed RPM

| Observed RPM | Coil Frequency | Theoretical RPM |
|---|---|---|
| $30 - 31$ | 6.17 Hz | 30.85 |

accommodate the travelling crack, valid observations may still be made about the nature of crack propagation on a microstructural scale.

v-K tests are potentially problematic with the current rudimentary visual methods of specimen alignment, i.e. aligning the specimen visually in terms of its overall position in the rig. Should v-K tests be required in future, a more rigorous method of alignment would have to be devised, such as a notch alignment mark, or a grid placed beneath the specimen.

## 5.3 Stepper Motor Drive

### 5.3.1 Methodology

Once the stepper motor control circuit had been connected to the motor as shown in the circuit diagram in Appendix B, and it had been verified that the direction, pulse, and speed controls were functional as described in Appendix D, the signal output from one coil was connected via a 1 MΩ resistor to a positive input channel on the DAQ (see Figure B.1). A SignalExpress routine was created to capture the voltage trace coming through this channel while the motor was in operation, at a relatively slow speed. The routine recorded the frequency of the wave-form and applied Equation 4.1 to the result, giving the overall theoretical rotational speed of the motor. This value was compared to a timed observation of the number of rotations completed in 60 seconds.



### 5.3.2 Results

The voltage trace is shown in Figure 5.11. As expected, the output of the transistor was a square wave-form with a high amplitude spike on the initial gate-opening. This spike corresponds to the magnetisation of that particular coil, which in turn relates to the rotational speed of the motor.

The results and comparison are presented in Table 5.4.

The highest coil frequency recorded was 19.3Hz, corresponding to a motor rotational speed of 96.5rpm. At higher transistor switching frequencies, the stepper

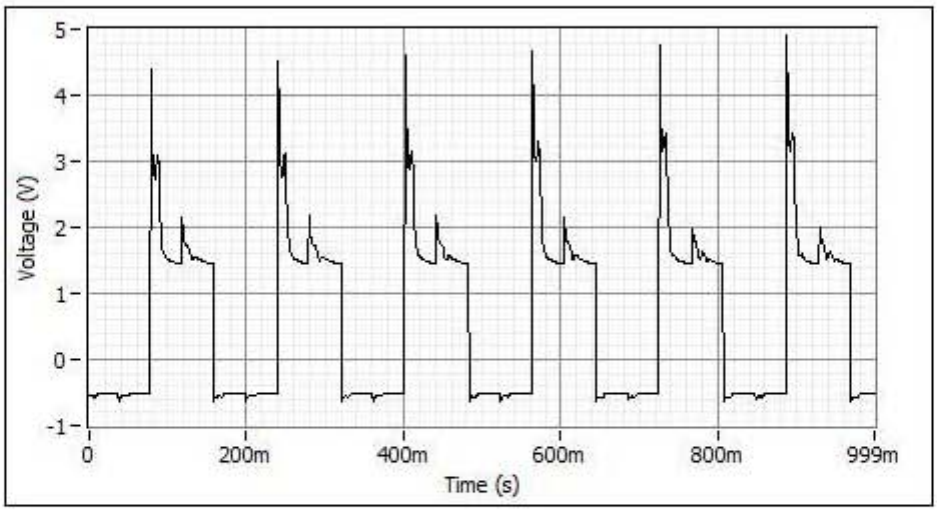


**Figure 5.11:** Voltage trace of one of the four transistor-switched stepper motor coils. The frequency of the wave-form was recorded at just over 6 Hz, which may clearly be seen from the graph.

motor reached its upper torque limit and stalled. This corresponds to a crosshead speed of just over 0.1mm/min.

### 5.3.3 Discussion

The stepper motor drive presented an adequate range of rotational motor speeds for the purposes of propagating stable cracks in the scanning electron microscope. The highest attainable speed before the motor load limit was reached was 96.5rpm, but it was not likely that this would be required of the system inside the SEM, as loading speeds in that situation are slow, and are better achieved by the motor pulse function.

A faster motor would have to be investigated should the need arise to have crosshead speeds faster than the 0.1mm/min upper limit.

## 5.4 Data Acquisition Card (DAQ)

Although the data acquisition device was a commercial product, an evaluation was run to determine its sensitivity, drift, and accuracy. The results of this evaluation had no bearing on the performance of the loading rig in applying a stable, incrementally precise load to the specimen under investigation. It was considered prudent, however, to investigate the reliability with which the applied loads could be read and recorded with the current setup.

### 5.4.1 Methodology

The device was connected to an external, low current DC power supply, which was dialled up from 0V to output 1.5V. This was then left to run for two lengthy periods, separated by a brief increase in the voltage which was then brought down to 1.5V. The DAQ voltage output was recorded continuously. The purpose of this was to check whether the reading from the device corresponded within reasonable limits to the input voltage, to observe whether there was any drift in the reading over the two periods, as well as to determine any effect on the readings between the approach from a high or low initial voltage.

### 5.4.2 Results

The initial DAQ readings were compared to the readings from a digital multimeter connected to the same voltage source. This was done to determine the accuracy with which the DAQ values were reported. It was found that both the DAQ and the multimeter readings of the source showed 1.54V on average for the first ten minutes of the experiment. The experiment was then continued with the DAQ readings alone.

Figure 5.12(a) shows the voltage trace given by the DAQ over a period of approximately 46 minutes, having dialed to 1.5V starting from 0V. After this period, the voltage was increased to approximately 3 volts, and reset to an indicated output of 1.5V in order to see whether the approach from above had any effect on the recorded reading. The result of this is approximately 75 minute test shown in Figure 5.12(b).

In the first trace it can be seen that the voltage drifts down from 1.540V to 1.535V over 46 minutes; a decrease of 5mV. In the second trace it decreases from 1.540 V to 1.529 V in approximately 75 minutes; a change of 11mV. As a more equitable comparison, and generalising the descent as linear for comparison purposes, the rate of downward drift is $1.79 \times 10^{-6}\,{}^{mV}/_{\mathrm{s}}$ in the first trace, and $2.44 \times 10^{-6}\,{}^{mV}/_{\mathrm{s}}$ for the second half of the test. The second trace exhibits a steeper decrease over time as compared with the first trace.

The noise level in the DAQ is shown to be relatively high compared to the nominal reading (as shown by the approximately 3 mV value bandwidth), although all the reported values are still within the uncertainty range of the DC output source. Due to both of these factors, little can be concluded about the influence of increasing or decreasing towards a certain voltage on the DAQ readings. Even so, the downward drift in the second 'post-increase' trace is a pronounced feature that is not as apparent in the first instance, where the signal was dialled in from

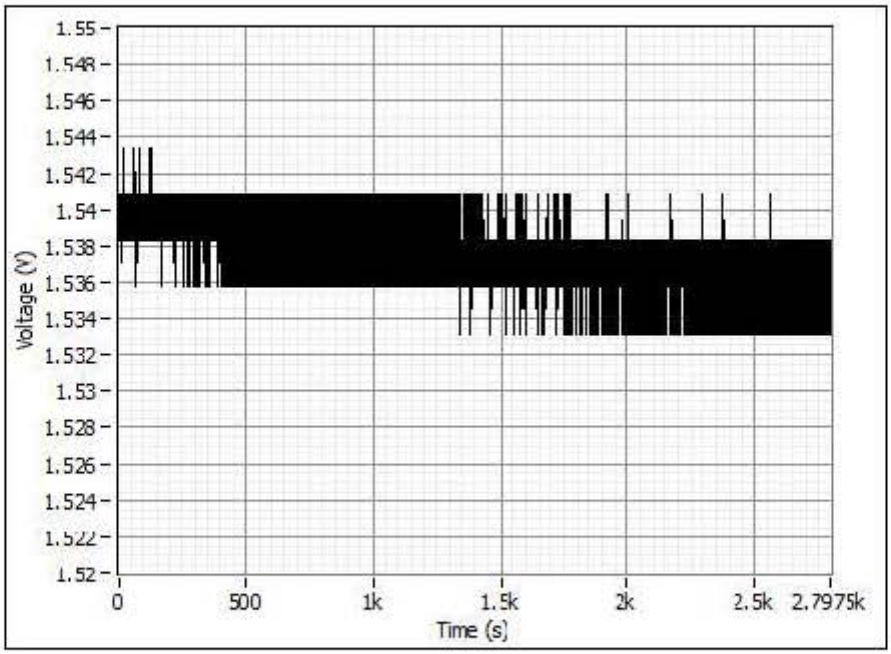


(a)

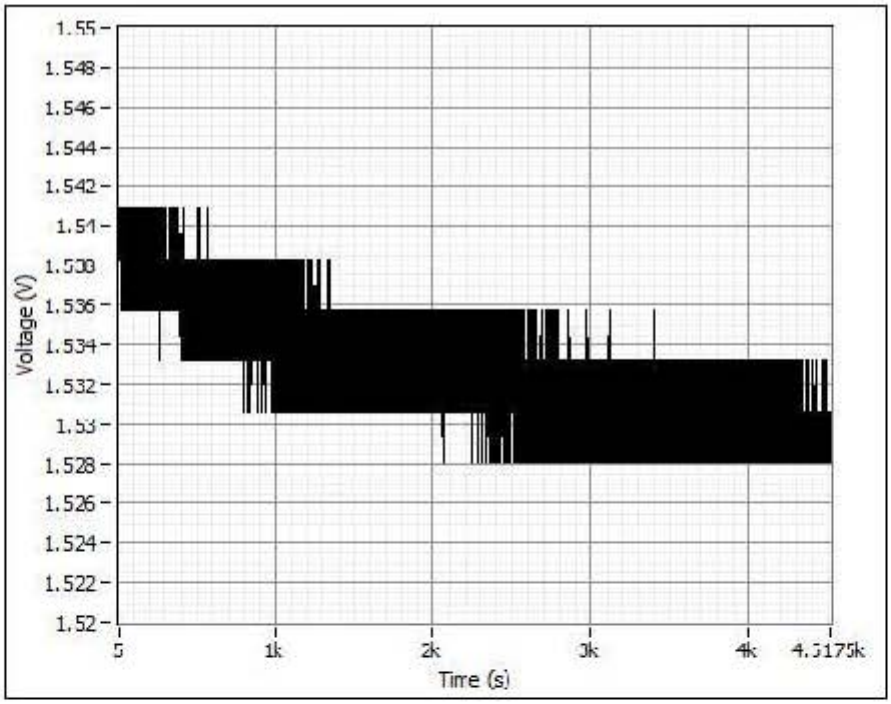


(b)

**Figure 5.12:** Voltage trace of DAQ recording the output from a DC power supply at (a) 1.5V displayed output and (b) 1.5V displayed output after shifting to 3V and decreasing to 1.5V.

below and held level. Following on from this, and from the plausible estimate that a SEM observation is likely to take in the region of 60 minutes, one must assume a minimum possible shift of $\pm 10\,\text{mV}$ in the experimental DAQ reading in practice, especially if the applied load is being decreased from an upper value.

### 5.4.3 Discussion

The DAQ was found to report values within the range of uncertainty present, despite having a relatively high noise output. The minimum input voltage it can accept is 1V, meaning that the 12-bit DAQ should have a resolution of $1/4096 = 0.24\,\text{mV}$, yet the noise width exceeds this value. For this reason, the overall performance of the DAQ is not particularly suitable to precision work.

It was decided ultimately to leave the output as it was, with a comment on the uncertainty factor and the possibility of investigating the relationship between gain and uncertainty in future work.

## 5.5 Uncertainty

An understanding of the uncertainty in a system is integral to any experimental setup. The main contributor to the uncertainty in this setup is the calibration of the strain bar by means of a 10kN load cell. As discussed, this contributes at least 5N uncertainty to any measured load.

Other sources of uncertainty include the strain indicator, whose reading in microstrain has an inherent drift of approximately $3\,\mu\varepsilon$, as well as being sensitive to movement of the connecting wires, which may contribute an estimated further $5\,\mu\varepsilon$. This $\pm 8\,\mu\varepsilon$ results in a load uncertainty of 0.75N according to Table 5.3.

There was both a drift in the DAQ reading as well as a noise inherent in the reading when tested at 1.5V. Neither of these values should be affected by the actual voltage going through the device, i.e. both the noise and the drift should remain constant over any voltage. The observed reading had a bandwidth of approximately$3\,\text{mV}$, resulting in a noise level of $\pm 1.5\,\text{mV}$. The accountable drift was recommended at 10mV, which gives a total uncertainty in the DAQ reading of $\pm 11.5\,\text{mV}$. Using the strain indicator output parameter of $0.465\,\text{mV}/\mu\varepsilon$ and Equation 5.3, the load uncertainty inherent in the DAQ is 2.64N.

The total of all these load uncertainties is $\pm 6.9\,\text{N}$. In Section 4.1.2 it was reported that the graphite specimens used had a fracture load of approximately 50N. The analysis of these uncertainties shows that any fracture toughness or loading values

**Table 5.5:** Summary of uncertainties inherent in the in situ SEM loading system

| | Uncertainty Value | Load Equivalent |
|---|---|---|
| Load/strain calibration | – | $\pm 5\,\mathrm{N}$ |
| Strain indicator drift & noise | $\pm 3\,\mu\varepsilon \pm 5\,\mu\varepsilon$ | $\pm 0.75\,\mathrm{N}$ |
| DAQ drift & noise | $\pm 10\,\mathrm{mV} \pm 1.5\,\mathrm{mV}$ | $\pm 2.64\,\mathrm{N}$ |
| Total | – | $\pm 6.9\,\mathrm{N}$ |

gained may be subject to error, and given the fracture toughness, the experimental uncertainty is in the region of 13.8%. Table 5.5 summarises these values.

This chapter has highlighted the performance of the rig in key areas, and it was in this configuration that the rig was installed in the SEM according to Appendix D. The following chapter presents the results of the material testing conducted in the SEM.

# Chapter 6

# Material Testing

In this chapter, selected micrograph images from the SEM testing are presented, which illustrate viability of the *in situ* SEM miniature DT testing facility, and also the mechanisms involved in damage accumulation in the materials tested. These results are also discussed within the context of brittle material behaviour. PMMA results are shown first, as they enable an understanding of the capabilities of the mini-DT system. Nuclear graphite images are then presented: the notch tip damage images are presented first, followed by crack tip damage, microcrack damage, and selected crack wake features. These provide insight into the mechanisms of toughening and embrittlement in graphite fracture. Videos of the loading sequences are available on the attached DVD, under the file names given in the text.



## 6.1 SEM Experimental Methodology

For the SEM tests, the rig and affiliated systems were installed and operated in accordance with the procedures set out in Appendix D, and the specimens were loaded onto the rig in the same manner as in the bench tests, described in the previous section.

PMMA specimens were used with the rig in the SEM initially, in order to commission the rig and determine the performance parameters that could be expected with graphite or other brittle material testing. Video capture of the loading sequences was performed, and the velocities of crack propagation were determined by visually measuring the extent by which a crack had grown over a certain amount of time.

For the graphite specimens, various regions of interest were observed: the notch tip, the main crack tip, and regions of microcracking. At each region, load was

applied and micrographs were taken at a set number of revolutions of the motor, corresponding to a certain crosshead displacement. At the notch tip, this was done in order to observe the development of microcracking in the initial fracture process zone. Loading was continued until the notch area was fully damaged. Damage was considered complete in the region once the macro-crack had passed the field of view, and any microcracks had relaxed, indicating the passing of the stress field associated with the fracture process zone.

At the macro-crack, sequential images were taken ahead of the crack tip in order to observe the processes involved in macrocrack formation: microcracking, jumping, branching, and tortuosity. This was continued until the main crack passed, or until it was clear that the damage had accumulated away from the field of view.

The third type of test involved locating a site at which microcracks could potentially develop, and again taking a sequence of images at successive loading intervals. In this way it was hoped to be pre-emptive, in that damage initiation could be observed from the very beginning, as opposed to only observing it once it had developed sufficiently to be visible.

Aside from the sequences, micrographs of interesting and illustrative features in the crack wake were also taken, as these are often missed in post-fracture SEM tests, where cracks have relaxed and are therefore difficult to make out.

Certain image sequences were run through a digital image correlation algorithm at the University of Manchester, to ascertain whether the technique could provide additional detail in the analyses of the material behaviour.



## 6.2 PMMA Results

### 6.2.1 Fracture Appearance

Figure 6.1 shows a representative image of the cracking behaviour of PMMA under double torsion loading.

On the material side, it is interesting to note that PMMA exhibits microcracking to some degree, although far less than is seen in the polycrystalline ceramics. That is, even though fracture in PMMA is not generally characterised by a fracture process zone, i.e. linking of microcracks, it does appear to have a very localised region of microcracking, in addition to primary crack extension.

This observation is not thought to affect the assumption made in previous research that PMMA conforms to LEFM behaviour. This is because the microcracking in PMMA is more representative of 'bulk' cracking behaviour – the percentage of

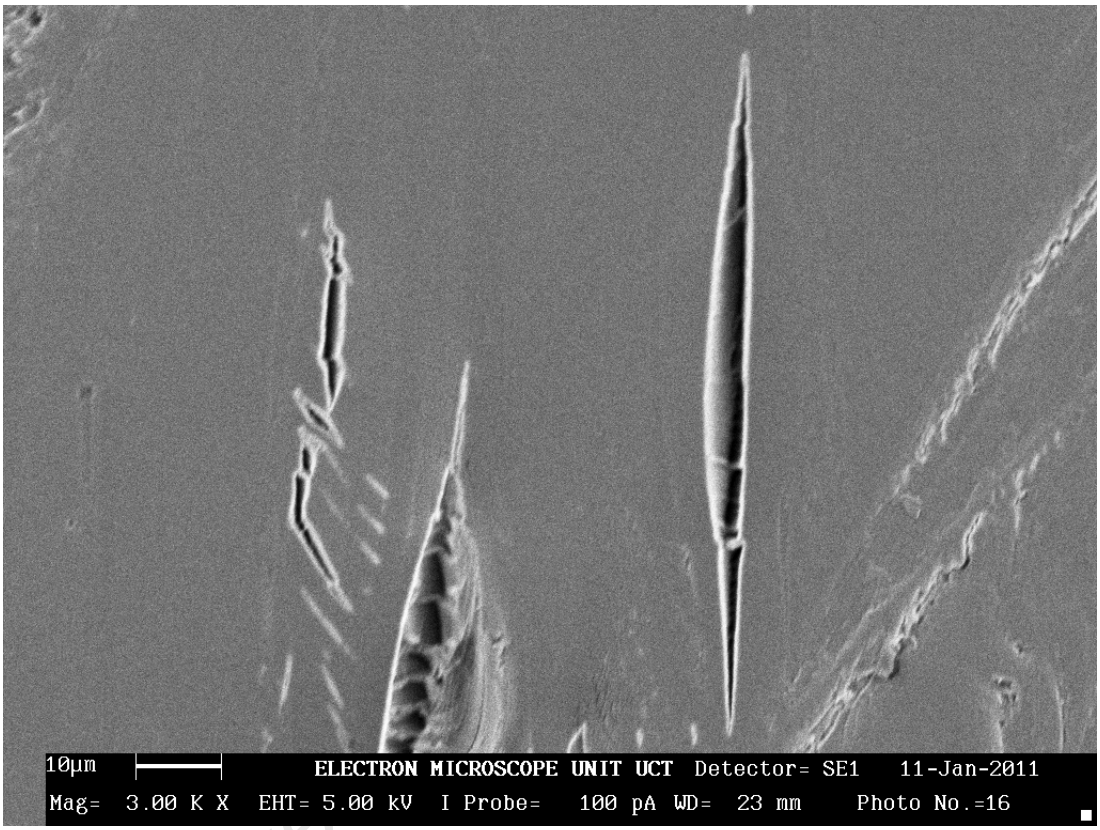


**Figure 6.1:** PMMA specimen cracking under an approximate load of 22N. The scars on the top left and bottom right of the image are from mechanical degradation of the specimen prior to carbon coating, as are the 45° markings to the left of centre. What was a light attempt to provide notable features on the face of the specimen resulted in stress concentration features instead. Note how all 'minor' cracks apparent in this picture are opening under load, in comparison with the behaviour of graphite, shown later. *Movie file: 'Crack growth.wmv'*

microcracking is low compared to a material such as nuclear graphite, and as all the microcracks seem to open under load, they would all likely become part of the main crack. This is unlike graphite, where certain microcracks relax and close down after passing of the main crack. In this way, all (or most) PMMA microcracking contributes to bulk damage, and there is little in the way of energy loss or toughening associated with the 'process zone', as there is with graphite.

### 6.2.2 Slow Crack Performance

With regards to system performance, the PMMA specimens were useful in demonstrating the crack control capabilities of the mini-DT system.

In the video capture clip *'PMMA_ 8_ clip.wmv'*, distributed with this document, the growth of a crack is shown in three different stages at a magnification of 3000×. Propagating from the bottom of the visible display upwards, each stage shown corresponds to a position of the SEM stage. i.e. When the crack propagated too far up the visible display, the SEM stage was adjusted so as to resposition the crack tip at the bottom of the display. In this way, three 'frames' or 'stages' of approximately 0.1 mm are shown for the propagation of one crack.

The video captured the crack behaviour as the load was increased to approximately 25N and then halted. This load, through Equation 3.2, corresponded to a stress intensity factor of approximately $1.16\,\mathrm{MPa}\sqrt{\mathrm{m}}$. Through the v-K relationship for brittle materials, it was expected that at this value of stress intensity there would be some velocity associated with the crack growth. The video, captured in real-time, enabled the average crack velocity per 'stage' to be determined, given that the viewable area is approximately 0.1mm. The first stage shown exhibited a crack velocity of approximately $9 \times 10^{-6}\,\mathrm{m/s}$, which by the third stage had slowed to $v \approx 2 \times 10^{-6}\,\mathrm{m/s}$. See Section C.3 for calculations.

During the period shown in the clip, the strain was noted as having relaxed from 262 - 255 microstrain, corresponding to loads of 24.7 - 24.1N, and hence stress intensities of 1.16 - 1.13$\mathrm{MPa}\sqrt{\mathrm{m}}$ during the first and the third frame, respectively.

These stress intensity factors, and corresponding crack velocity values, were plotted against each other and these v-K data points compared to a comprehensive plot by Becker [12] for PMMA. As one can see in Figure 6.2, the v-K values for the two crack stages fall within the red scatter band, which corresponds to the classic Evans methodology for the DT specimen, with thickness correction – the same method used here to calculate stress intensity.

This result is important as it verifies that this mini-DT system is capable of

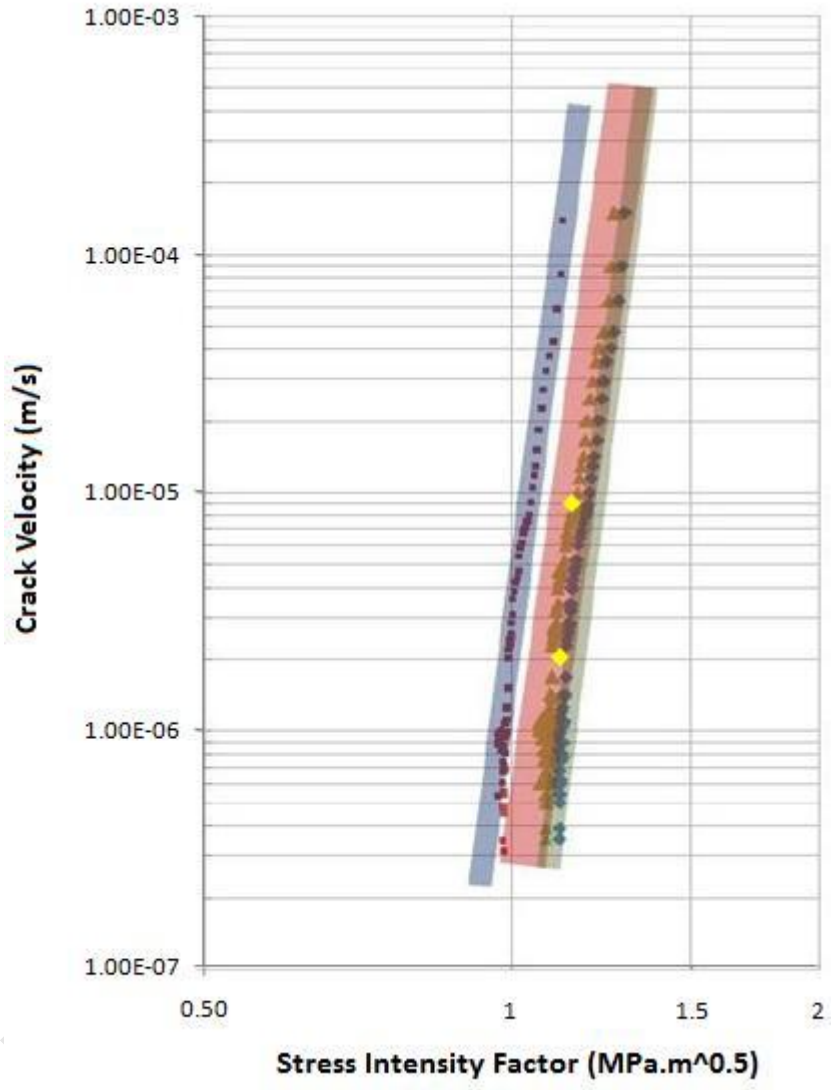


**Figure 6.2:** v-K data points for PMMA specimen in the mini-DT rig. The data points (yellow diamond) are superimposed on a plot by Becker [12] for PMMA, which shows the scatter bands associated with the Evans (red), Ciccotti (blue), and Chevalier (green) methods of calculating the stress intensity. The stress intensities for the PMMA specimens in the current work were calculated according to the Evans methodology, and can be seen to fit within the margin of error of the macro-data.

producing results in line with existing v-K crack growth data derived from macro-tests.

Images out of another sequence taken at low load are shown in Figure 6.3. While the time taken to propagate these cracks cannot be determined exactly as the micrographs are averaged from the top down over a time period, one can gain an estimate by the fact that for this sequence, the loading, averaging, and capturing sequence took approximately 90 seconds. The assumption is therefore made here that the time taken to propagate between the states shown in the successive images is 90 seconds (a conservatively fast estimate).

Given this time frame, and the ratios between the micron marker and crack lengths in successive images, the crack velocity was calculated to be of the order of $19\,{}^{nm}/_{s}$, or $19 \times 10^{-9}\,{}^{m}/_{s}$ (see Section C.3). This is far below previously measured crack velocities.

## 6.3 Graphite Results

The following paragraphs cover the testing of nuclear graphite in the SEM. Images and results from the testing are presented alongside comments about the material behaviour. An overall discussion on graphite microfracture in the context of this testing is presented at the end of the chapter.

### 6.3.1 Notch Tip

Figure 6.4 shows the notch of specimen S123_3 at increasing stages of applied load, from left to right, top to bottom.

A crack forms stably at the notch tip, despite the fact that in graphite the initial fracture toughness, close to the beginning of the specimen, is higher than the value exhibited in the constant stress intensity region (refer back to Figure 3.3 on page 35). Of the three graphite specimens tested, each initiated a crack on the furthest protruded portion of the notch. In addition, of these three specimens, each crack propagated fairly straight, albeit with a certain amount of tortuosity, showing that even and symmetrical loading may be achieved in the DT rig. Figure 6.5 shows example images of the initial crack in each of the specimens.

Each of the specimens was mounted into the rig by hand, and aligned by hand, even though convergent tuning screws were available, and it was found that adequately symmetric loading may be achieved through this careful hand adjustment.

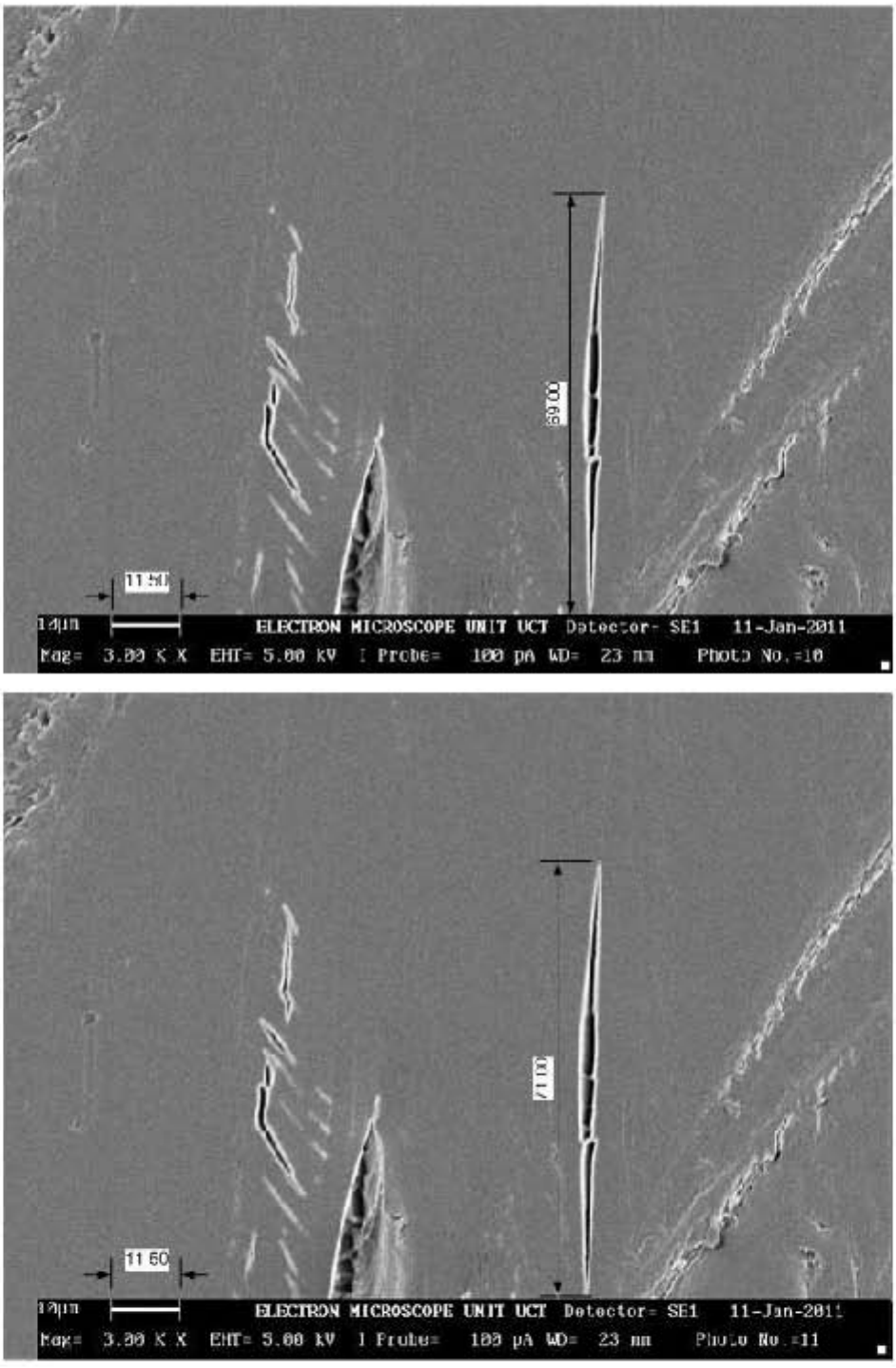


**Figure 6.3:** Selected images from PMMA loading sequence. *Movie file: 'PMMA 8 Crack growth.wmv'*

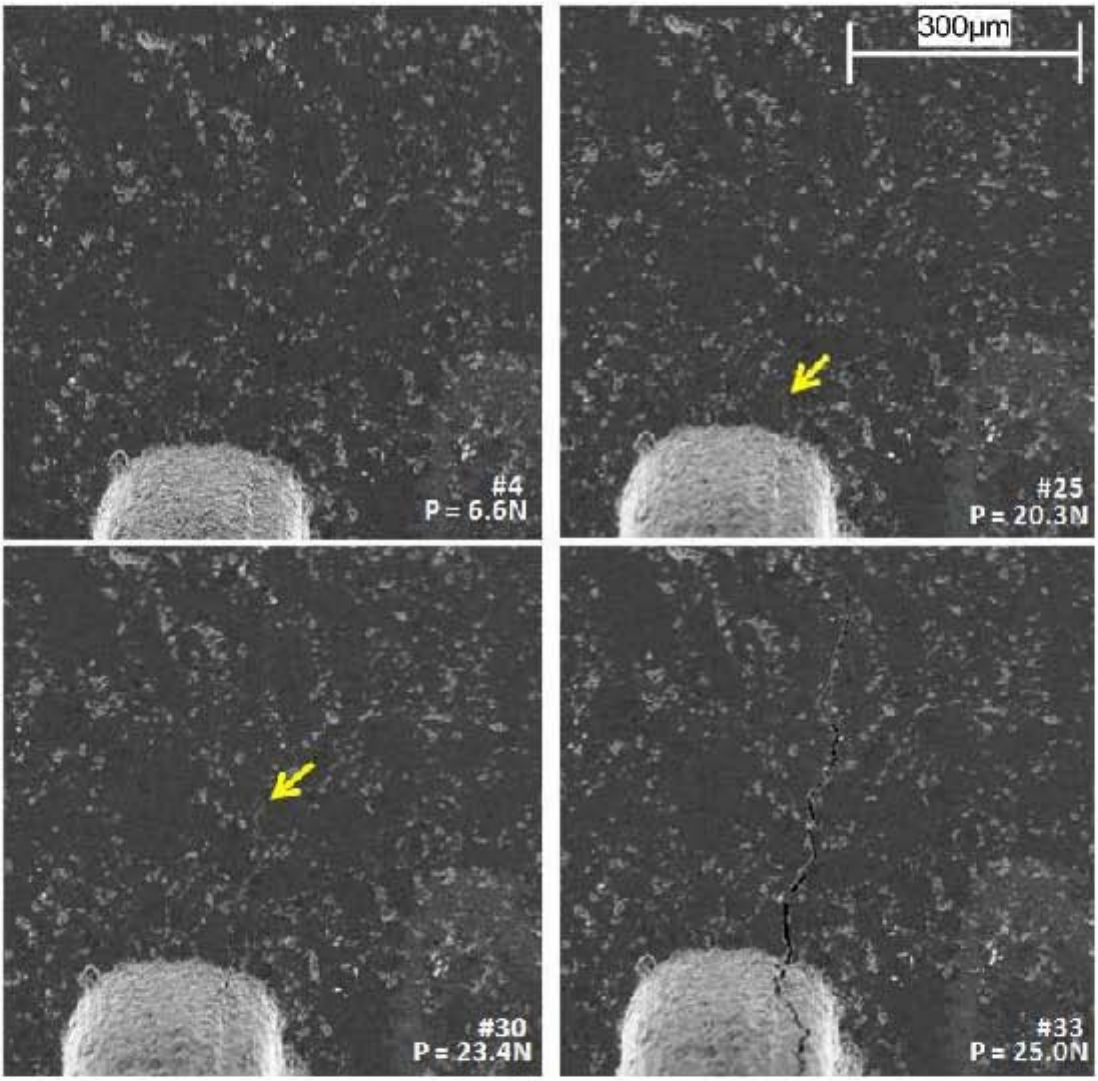


**Figure 6.4:** Selected images from a loading sequence at the notch tip of S123_3. The arrows point out the location of the tip where it is faint. The notch is approximately 0.3mm wide. *Movie file: 'S123_3 Notch.wmv'*

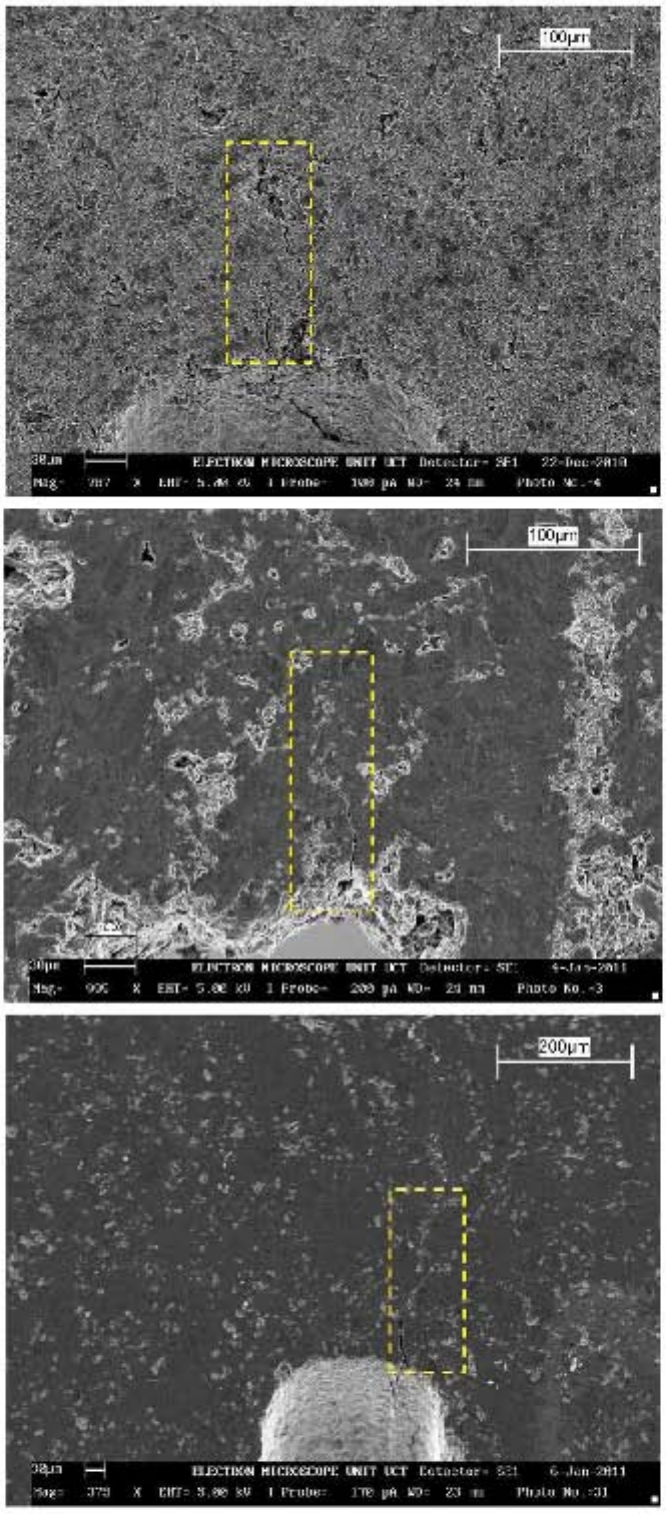


**Figure 6.5:** Initial cracks in each of the three graphite specimens tested. Note the difference in appearance between the topmost image, of an unpolished specimen surface, and the clarity of the remaining images, showing polished specimen surfaces. Very few surface features could be distinguished from the first (unpolished) test specimen, and the remainder of the specimens were polished to facilitate better observations.

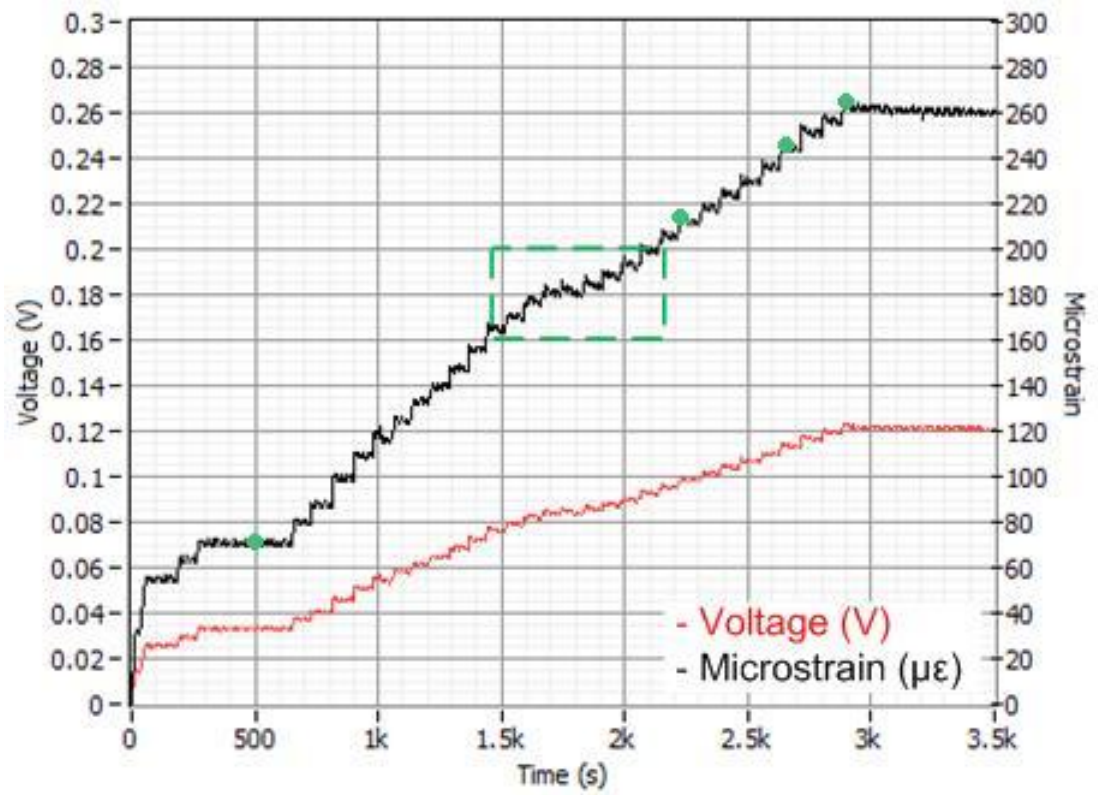


**Figure 6.6:** Notch loading sequence voltage trace, with the conversion to microstrain shown. The dots mark the points at which the images in Figure 6.4 were taken, and the box highlights the loading steps where the notch crack first developed.

Referring again to specimen S123_3, the voltage trace from the notch loading sequence is given in Figure 6.6, and is shown in red. Also shown on these axes is the conversion of the voltage trace to microstrain, shown in black. The points at which the images from Figure 6.4 were taken are shown in green, at 70 $\mu\varepsilon$, 215 $\mu\varepsilon$, 247 $\mu\varepsilon$, and 265 $\mu\varepsilon$.

The progression of the loading sequence can be clearly seen in the appearance of the load 'steps' in Figure 6.6. The vertical face of the steps are the loading increases, whereas the 'horizontal' faces are where the loading was halted, and relaxation was allowed to take place.

Additionally, there are a few other features in the graph which signify certain behaviours in the specimen.

For the first few loading steps, there is little relaxation shown, as can be seen by the constant values of the trace once loading was stopped. Further on, however, as exhibited in the region highlighted in the green box, there is clear relaxation as the trace drops to just below the previous loading level. This behaviour reveals the point

at which cracking initiated in the specimen, although this is not yet visible in the micrograph images taken at these load steps. Aside from an anomalous occurance of relaxation at 120 $\mu\varepsilon$, which may be attributed to a locally stressed portion of the specimen, or a local settling of the rig, examination of the trace shows relaxation becoming apparent from approximately 158 $\mu\varepsilon$ ($\sim$ 15N).

There is a gradient change in the overall graph as well, better seen in the voltage (as opposed to microstrain) trace. This gradient change shows an increase in compliance from before the region of initial 'fast' fracture (where the crack was formed from the notch), suggesting a more controlled crack growth rate. It is interesting, however, that with the subsequent increases in load the relaxation when halted does not become more pronounced in this second region, as one would expect with the crack velocity theoretically increasing due to the v-K relationship. The implication is that the mechanism of crack growth is not completely free in graphite, and is hindered by the microstructural features of the material (e.g. pores, grain boundaries, etc), which may not allow a crack to propagate continuously.

### 6.3.2 Crack Tip Behaviour

The images presented here are representative of the behaviour of a fully formed crack tip, removed from the specimen notch. All images were taken when loading was in the region of 24 - 28N, well below the load required to cause fracture according to the reported fracture toughness value of nuclear graphite.

Figure 6.7 shows some interesting features. The main crack in this image has propagated up from the bottom of the image, and diverted its course at the point marked with an 'x' towards a filler particle outlined in yellow, then split around the particle before arresting in the centre of the image. An entirely new crack then appears to have formed at the boundaries of a nearby filler particle (also outlined in yellow), which has then taken on the full effect of the applied load and propagated upwards out of the picture. This is a good example of crack "jumping," as described in Section 2.2.2.

Careful examination of the outlines of the filler particles reveals that these appear to be a main determinant in a potential crack growth direction, in that the crack path is seen to follow them exactly, even to the extent where a well-established crack path is diverted, or where the crack "jumps" to a nearby particle boundary. This behaviour is also seen in Figures 6.8 and 6.9.

Both Figures 6.7 and 6.8 show the characteristic of a crack opening *around* a grain boundary, as opposed to through the grain. Figure 6.9 shows a sequence of

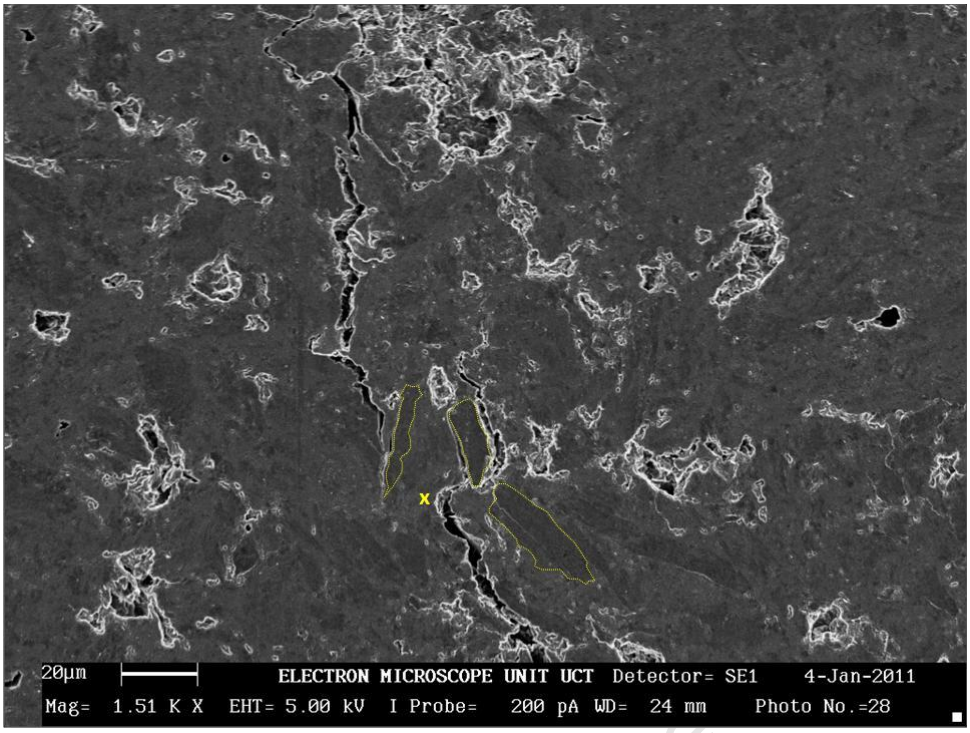


**Figure 6.7:** Crack "jump" features and secondary cracking in specimen S123_2

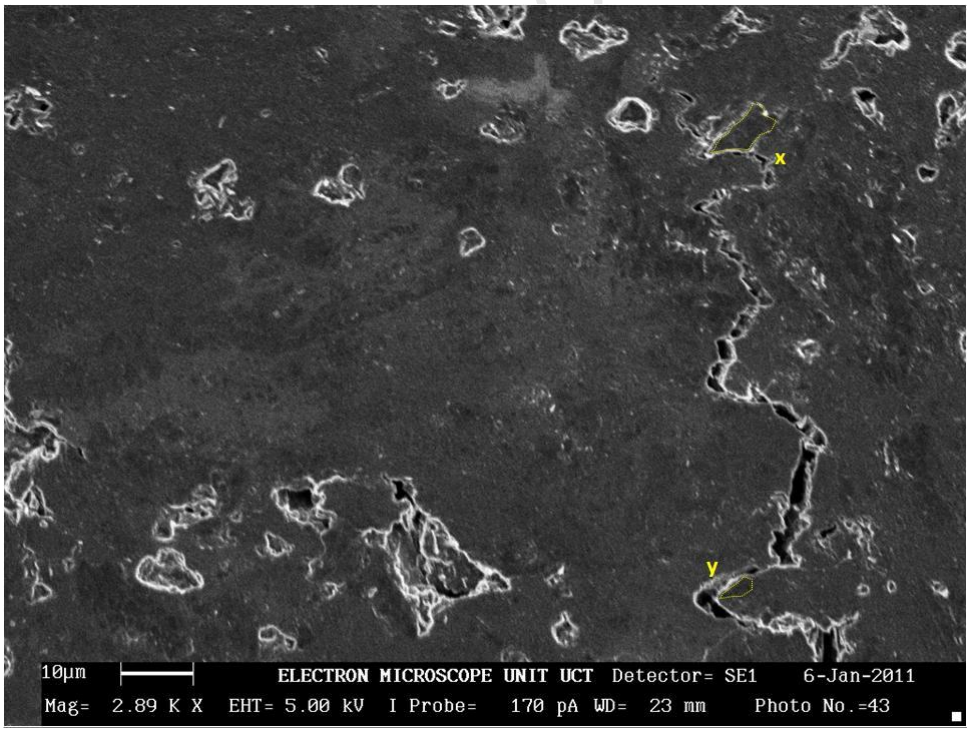


**Figure 6.8:** Tortuous crack path in Specimen S123_3. At locations marked 'x' and 'y' the crack changes direction in order to follow the line of the weaker grain boundaries.

cracking (sequentially from top to bottom) which also exhibits this behaviour at first, but makes an interesting comment about the local stresses associated with grain boundary cracking:

In the image sequence shown in Figure 6.9, a tortuous crack path is being produced by the linking of the upwards-propagating crack with the highlighted grain boundary. The crack meets the boundary in an unfavourable position, which would ordinarily result in the higher stress intensity shear opening mode (mode II, illustrated in Figure 2.2) had the main crack continued on this path. What has ocurred instead is that the local mode I fracture toughness for the region is lower than the mode II stress intensity required to overcome the friction provided by the crack faces and to open the crack in this shearing manner. The crack subsequently fails in mode I, creating *entirely new* crack faces in previously undamaged material. This observation provides empirical evidence of the contribution of frictional surfaces, and hence grain orientation, to overall toughening.

### 6.3.3 Microcracking Behaviour

Figure 6.10 shows a portion of material where multiple possible crack paths became significantly developed under loading. The first image highlights areas of partial damage (microcracking) at a certain load step, including a large unopened crack forming to the left of the apparent main crack, while the second image shows the same region after the main crack has passed upwards and beyond the field of view. The leftmost crack has developed to a large extent, but then subsequently halted, allowing the eventual main crack to absorb the energy of the stress field caused by the applied loading.

In general, the crack path behaviour is dominated by local effects, as seen in the previous section. At the top of the main crack is a substantial stress field which results from the applied loading. This stress field acts on existing microcracks, causing localised areas of high stress intensity. When this localised stress intensity exceeds the local fracture toughness, the microcracks propagate or extend, linking to extend the main crack. The stress field then moves on with the extension of the main crack, resulting in the observed relaxation of cracks which may have opened (but not propagated) under the influence of the field.

Returning to the behaviour observed in Figure 6.10, from the first image it is unclear as to which was the weaker path, as even though the leftmost crack was large and fast developing, the 'main' crack path exhibited a fair amount of microcracking. However, the cause of the localised lower fracture toughness which eventualy resulted

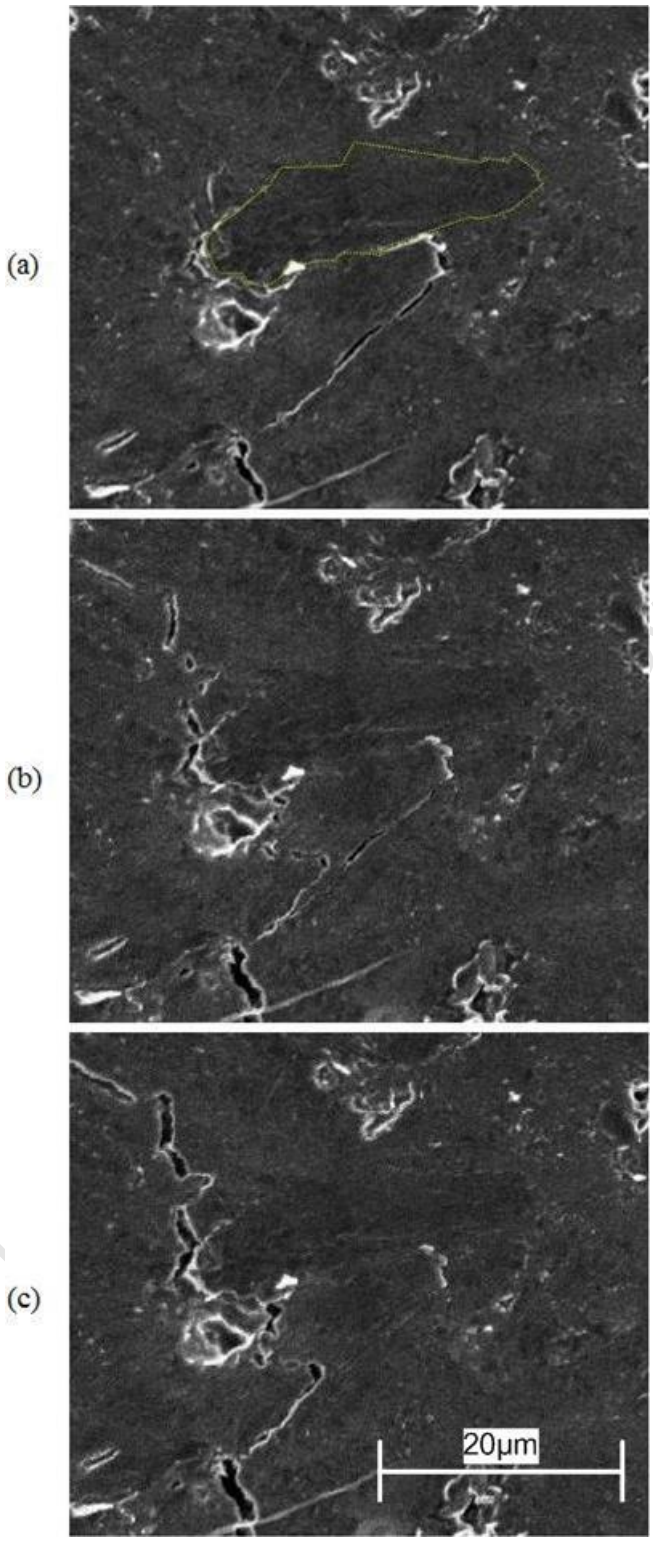


**Figure 6.9:** Crack opening sequence in specimen S123_3.The crack is initially on course to open in a shearing motion due to forming along the bottom-most face of the filler particle (boundary highlighted). Previously undamaged material then opens instead, in a lower energy mode than previously.

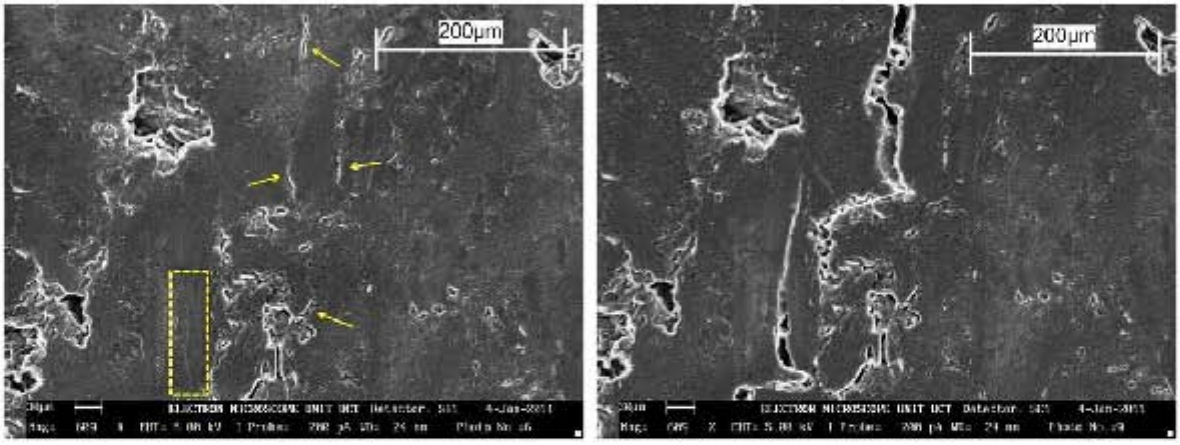


**Figure 6.10:** Images of crack tip loading in specimen S123_2, showing the partial development but eventual collapse of a large subsidiary crack.

in major propagation may be gleaned from examining the second image, and noticing that there is a deviation in the crack path around the upper quarter of the image. This, even though not immediately visible, suggests the presence of a sub-surface grain which has subsequently been skirted by the crack.

Figure 6.11 shows further images of microcracking behaviour, and emphasizes the ability of the mini-DT technique to manifest and observe evidence of the opening, closing, and changing of microcracks as they propagate in a loading sequence.

### 6.3.4 Crack Wake Features

Other features of toughening were seen in the *wake* of cracks that had passed the field of view, including branching, tortuosity, and crack jumping. Examples are given in Figures 6.12 - 6.15.

### 6.3.5 Digital Image Correlation

Digital image correlation was performed on certain crack growth sequences, using an algorithm at the Graphite Research Unit at the University of Manchester. The technique had limited success in this case in showing up movement and damage that was not already visible in the SEM, although it did exhibit some movement detail. Figure 6.16 shows an image sequence of DIC performed on a region of specimen S123_3. It is the same region as shown in Figure 6.11. The main crack is shown very clearly, with some of the larger microcracking detail also highlighted. This sequence enables one to better identify areas where microcracks have shut down, although the detail is not different from that which may be observed in the original

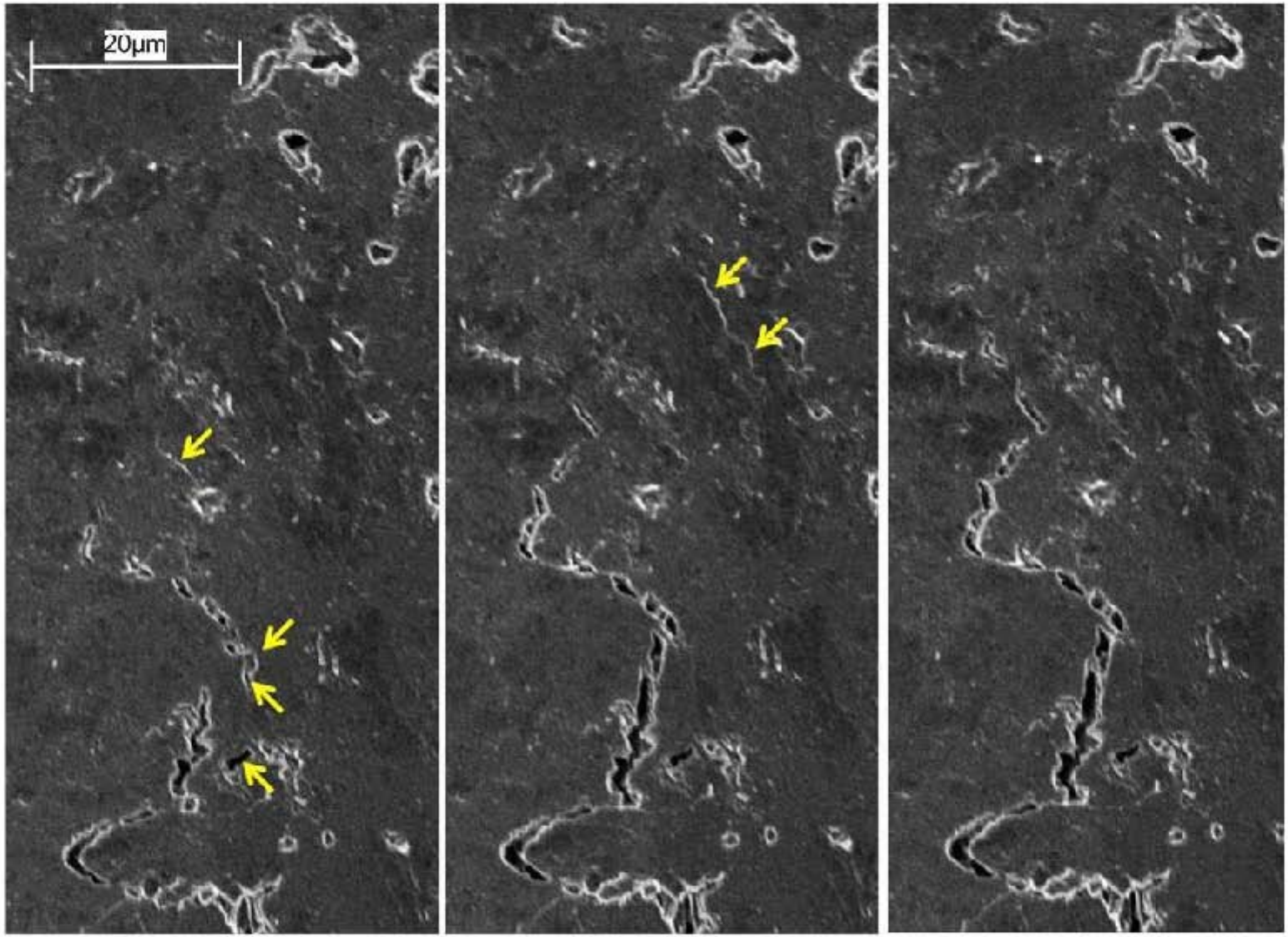


**Figure 6.11:** Sequence of images showing the behaviour of microcracks in the vicinity of a crack tip in specimen S123_3. Arrows point to microcracks which are present in one image, which change or disappear by the following image. *Movie file: 'S123_3 Tip 1.wmv'*


Department of Mechanical Engineering
University of Cape Town

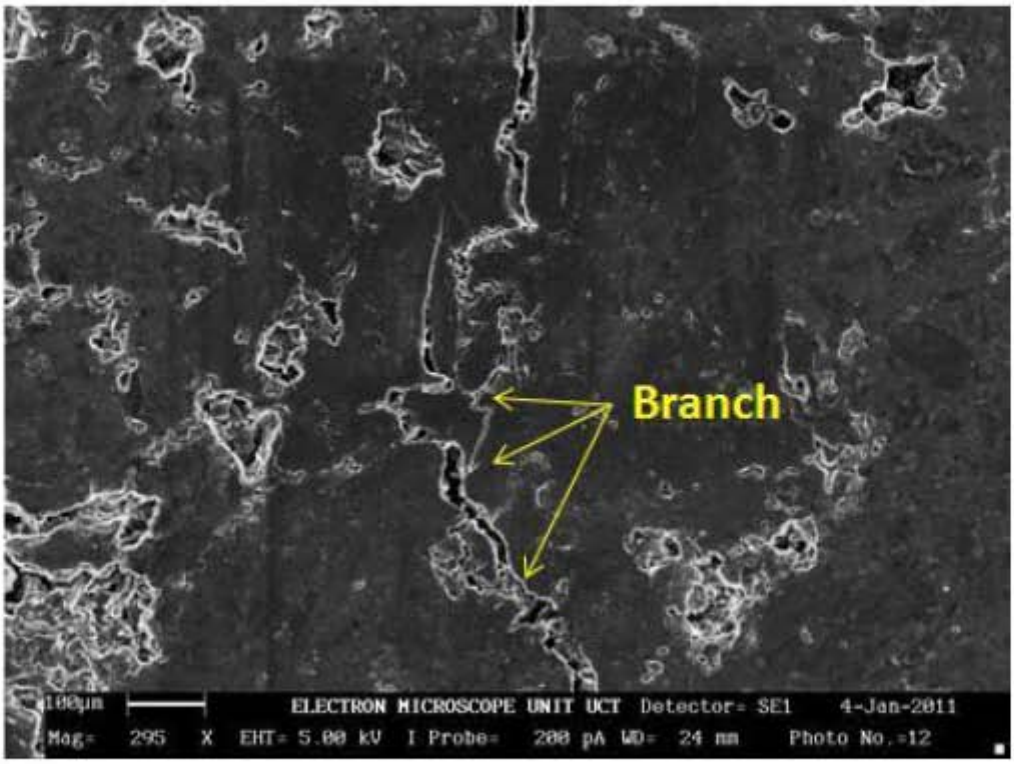


**Figure 6.12:** Features of crack propagation: branching

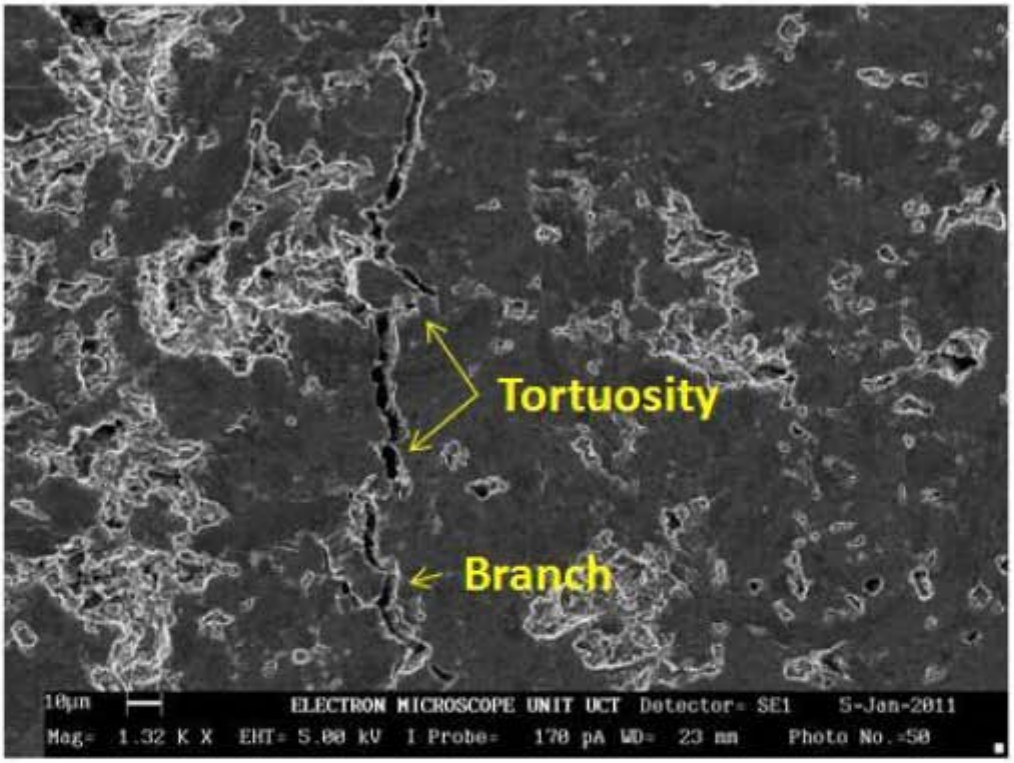


**Figure 6.13:** Features of crack propagation: branching and tortuosity

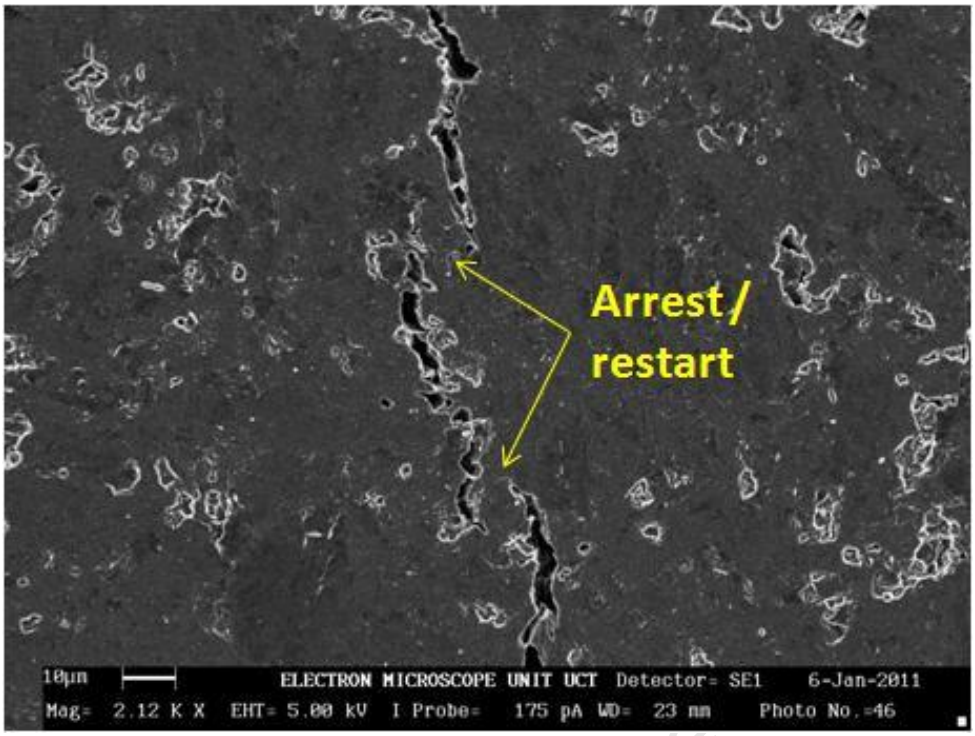


**Figure 6.14:** Features of crack propagation: multiple arrest and restart points

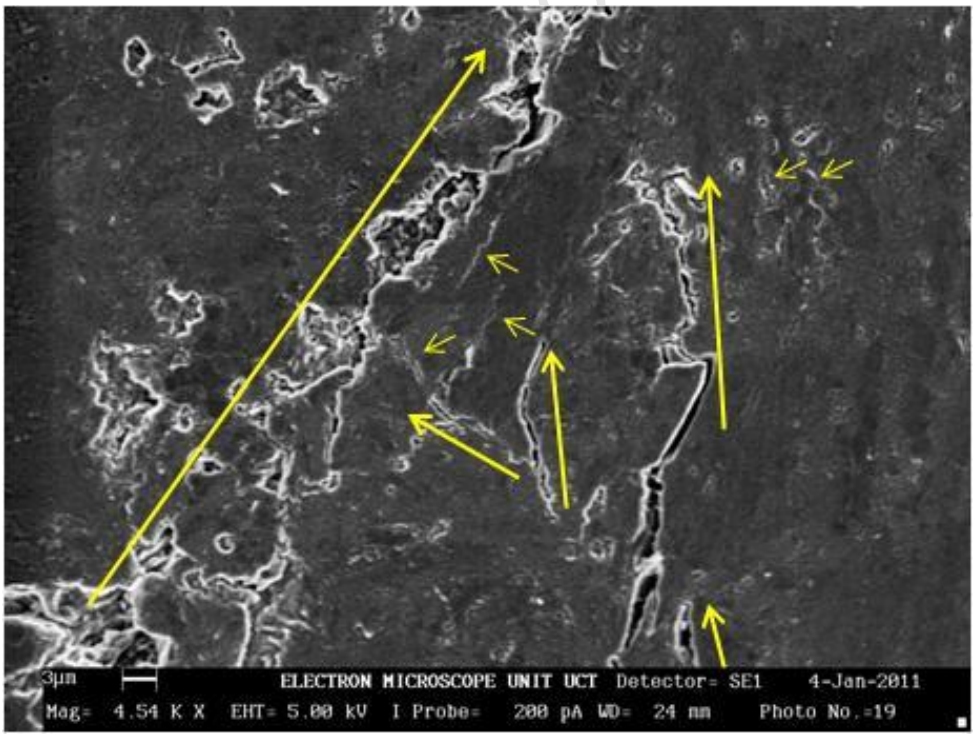


**Figure 6.15:** Features of crack propagation: multiple propagating cracks, with microcracking

images. Also, caution must be taken in interpreting images such as this, as there is an inherent level of noise, as well as error associated with displacement of the original images.

Despite the shortcomings, the technique does present a very useful prospective tool in the analysis of damage development at this scale. Investigation of the optimal settings, and a finer resolution, for the technique could produce greater detail and highlight regions of stress which do not yet exhibit visible microcracking (i.e. in SEM micrographs).

### 6.3.6 Discussion

What can be seen from the images above, and from the others distributed with this document, is that a significant factor in the eventual direction of crack path development was the presence of filler particles in the graphite matrix. In an examination of 24 visible crack-grain boundary interactions in all images taken, it was found that 17 interactions involved the crack following the grain boundary closely, whereas the remaining seven cracks passed through a filler particle. This is an occurance of 71% for this sample size. The complete set of observed interactions is marked in the computer images folder 'Crack Paths', distributed electronically with this document.

As seen in Figure 6.9, where a crack developed at a grain boundary that was perpendicular to the main crack propagation direction, the energy required to pass through a filler particle is even greater than that required to form a completely new crack in the binder material. From a strength point of view, this shows the benefit of unfavourably orientated grain boundaries with respect to propagation direction (and increased toughness), and confirms the measurements of Becker [5] and others who report a higher fracture toughness value for perpendicularly orientated cracks (with respect to extrusion direction of the material) than for those orientated parallel to the extrusion direction. It also supports the case that for applications where graphite is exposed to high heat and irradiation, which induces non-uniform stress conditions (i.e. stress which cannot be assumed to apply in one direction only) and localised damage, a more isotropic material is favourable, given that there is an even distribution of grain boundary directions and uncertainty as to which direction the stresses will cause a crack to propagate.

A side point to be made is that crack tortuosity may be seen as an indication of crack toughening, as opposed to a cause. Tortuosity is caused by linking of variably orientated microcracks, which are most likely to derive from variably orientated

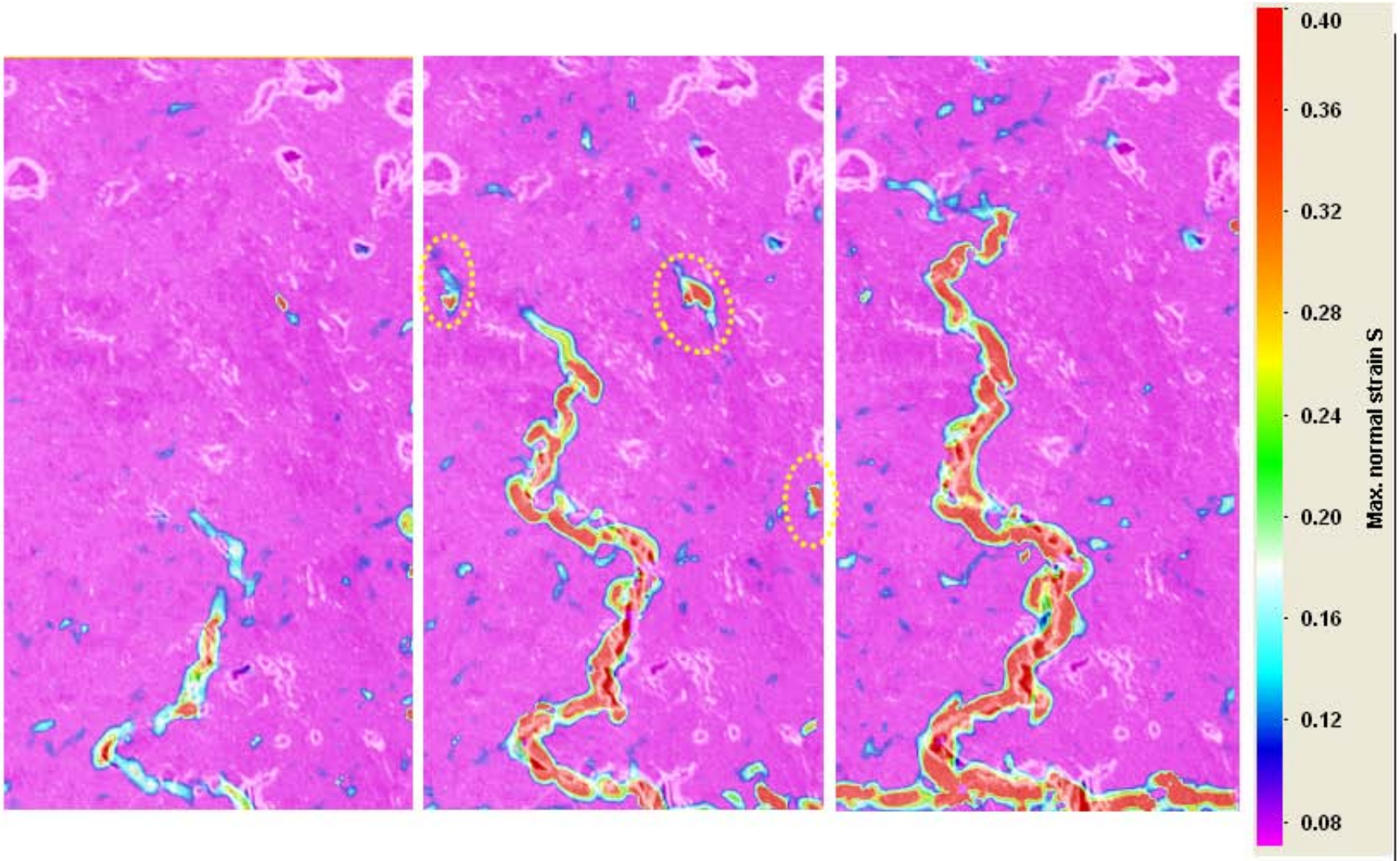


**Figure 6.16:** Images from a DIC analysis on crack features in specimen S123_3. The analysis was run images from the same sequence as shown in Figure 6.11. Note the highlighted features which change between the second and third images, showing areas which close down once the main crack has propagated.

filler particles. The friction caused in the shear opening mode associated with unfavourably orientated microcracks is the actual mechanism of toughening, whereas the tortuosity itself is a byproduct of this process. This is worth mentioning because macro-scale tortuosity may in some cases be caused by other mechanisms, such as the arresting of a main crack and reinitialising of another crack nearby, or the following of a crack around a filler particle grain boundary which is orientated in such a way as to not produce friction (i.e. a 'cup and cone' type opening), which is a point of weakness. It should however, also be noted that, for nuclear graphite, this observation applies to the current grain size tested only, and may not hold in coarser structured graphite.

# Chapter 7

# Discussion on System Performance

This chapter is a review of the performance of the system and its suitability for purpose, similar to that given in Chapter 4. This chapter extends the review to the performance of the system in conjunction with the SEM, as well as discussing the issues that were uncovered during testing. An analysis of the behaviour of the rig is separate to a material testing discussion, although rig performance may have had an effect on the results gained for the materials tested. The reader is therefore advised to read this and the previous chapter together, taking note of this possibility.



## 7.1 General Overview of mini-DT System

This paragraph holds a discussion of the value of the mini-DT system in general. Given the information that one can get from macro-tests, can the mini-DT system contribute to the knowledge base surrounding nuclear graphite, and other brittle materials? Firstly, a few comparisons are discussed.

The macro system relies on an external load actuator, whereas this system, by default because of its working environment, has a built-in load actuator. The external load actuator can ramp more quickly, whereas the internal system is limited in speed (to just under 100rpm, which converts to a maximum crosshead speed of approximately 0.1mm/min), but is able to control crack growth due to the precision that is a result of this limitation.

A futher point is that one can determine characteristics using the macro-system that are difficult to determine with the miniature version. In the larger system, v-K curves can be generated, and fracture toughness tests can be performed due to the fast ramping capability of an external load applicator. Observation on that scale is also easier due to techniques such as digital image correlation (DIC), which highlight

regions of damage which may or may not contribute eventually to a macrocrack.

However, in the study of graphite and other similar materials, it is the micro-damage that is of interest, as the macrocrack may be seen as region where material damage is at 100%, whereas it is the development and arrangement of microcracks that result in this macro-damage. While bulk behaviour is of interest, it is also of use to understand the micro-damage process to be able to more fully characterise the damage mechanisms in these materials.

To this end, the mini-DT system has shown merit.

The technique has managed to show 'real-time' interaction of cracks with the microstructure on a scale which has not been seen before. In a purely cursory study of the fracture behaviour of graphite, the system enabled the observation of the proportion of influence of grain structure and filler particles on the development of microcracks. This study can be expanded to try and confirm such values for use in statistical modelling.

Because of the precise loading and measurement capability as compared to macro-testing, subtle changes in loading were observed at values which lay within the uncertainty range of most macro-loading facilities. This adds a dimension to the study of micro-damage, or damage which is invisible to the observer, outside of DIC techniques.

Overall the mini-DT technique used *in situ* in a scanning electron microscope is of value in the study of brittle and quasi-brittle materials such as graphite.



## 7.2 In situ SEM Performance

The overall performance of the rig inside the SEM was highly satisfactory. Apart from initial problems with the SEM/motor coupling arrangement (discussed below), the movement was free, with a suitable displacement range in the x- and y-directions. Specific components which deserve comment are discussed here.

### 7.2.1 Specimen Mounting

Good load symmetry was achieved using the hand alignment method described in Appendix D. It was found that the action of the fine-tuning screws were hindered somewhat by the loading fork, and that while straight crack growth could be achieved without them, should their use be required a modification to the rig would have to be made to accommodate smaller screws (perhaps ISO M2).

### 7.2.2 Load Application

The self-rectifying loading fork and symmetrically driven crosshead contributed largely to the achieved straightness of crack growth, as well as the consistency of the crack initiation point. As shown in the previous chapter, the crack in all three specimens initiated in the region of the notch tip, as opposed to occasionally initiating further down the side of the notch, as in-house experience dictates may happen with other systems.

The slow loading rate was beneficial at this magnitude and, with the 1 rev = 1.25 $\mu$m crosshead displacement ratio (800 revolutions for 1mm displacement), appears to provide a level of control not reported previously.

### 7.2.3 Field of View

The SEM image field of view was 9mm wide at the lowest magnification achievable, which was 42X. Depending on the type of material being observed, this may or may not be adequate, as it has been shown previously that the size of the microcracking process zone is larger in the DT specimen than in other fracture mechanics specimens [5]. Previous work on coarse graphite has revealed damage zone sizes of as much as 20% of the specimen width, which translates to 3mm in the current specimen, or full screen width at 126X magnification. However, at such a low magnification, the ability to observe the *behaviour* of the micro-damage is lost, considering the majority of microcracking observations in this work were made at magnifications in excess of 1000X. Additionally, the information gained by observing the whole low-magnified region could instead be gained with a technique such as DIC. The mini-DT technique should as such be seen as complementary to the macro-system in this regard, with fields of view in the range of 1mm down to $\sim 85\mu$m at a magnification of 4500X.



### 7.2.4 Range of Movement

The double universal joint setup within the SEM operated very well. The stage and rig were able to move to the limits of the specimen edges in the x-direction, with the motor still operating at these points. Rotating the motor *while* translating the stage, while possible, might not be smooth as there is no lubrication permitted in this system.

The range of movement in the y-direction was adequate for the tests performed for this work. However, the temporary mounting of the tilt/rotation mechanism on the SEM chamber door did have the capacity to impinge on the outside edge of the

rig if the stage was moved too far towards the door, i.e. in the event of following a crack past a certain length. While it did not affect the current work, this is a potential issue for work where the crack should be followed to complete specimen failure.

### 7.2.5 SEM/Motor Coupling Arrangement

It is worth mentioning some of the difficulties encountered in getting the stepper motor connected to the SEM shaft in a manner which transmitted the required torque without excessive wobble, and the remarkably simple solution that eventually presented itself.

Initially, a rigid coupling was tried, but rejected due to a machining misalignment which caused excessive wobble, as mentioned in Paragraph 4.3.7.2. With the realisation that the concentricity tolerances needed to prevent wobble were probably unattainable without computerised machining techniques, the idea was discarded.

A one-piece flexible aluminium coupling was then obtained, which also proved unsuccessful, with the grub screw having stripped during the application of loads in excess of 200N on polycrystalline diamond. The non-uniform diameters of the SEM shaft along its length also made seating of grub screws difficult.

It was eventually decided to make use of the original hand dial which had been present on the SEM. The dial was 15mm in diameter, so to match it a similar dial was obtained to fit to the end of the stepper motor shaft, with a piece of silicon tubing placed over both of these. This arrangement worked very well, as the tubing contracts in a direction perpendicular to any applied tension. This meant that as the motor shaft turned, the torsional force transmitted to the other end of the tubing drew it tighter over the hand dial. It was found that additional securing measures (such as cable ties, glue, etc) were not needed.



## 7.3 Peripheral Systems

### 7.3.1 DAQ Card

While the theoretical sensitivity of the 12-bit DAQ card was adequate for the purposes of this work, the actual sensitivity achieved was less than desired, for the reasons of noise and drift mentioned in Section 5.5. With a reference voltage input of 1V, the resolution of the readout should have been in the region of 0.2mV, or just under half a microstrain. As the resolution of the strain indicator was only one

**Table 7.1:** Comparison of DAQ and indicator readings for strain in Specimen S123_3

| | DAQ | Strain indicator | Difference | Error % |
|---|---|---|---|---|
| 1 | 70 | 65 | 5 | 7.7 |
| 2 | 260 | 254 | 6 | 2.4 |
| 3 | 274 | 265 | 9 | 3.4 |
| 4 | 288 | 280 | 8 | 2.9 |
| 5 | 259 | 251 | 8 | 3.2 |
| 6 | 208 | 200 | 8 | 4.0 |
| 7 | 275 | 270 | 5 | 1.9 |

microstrain, the 12-bit resolution was the correct theoretical choice. However, with a noise bandwidth of 3mV, or over 6 microstrain, the required sensitivity could not be achieved.

A possible method of mitigating this effect is to apply a large gain to the output of the strain indicator. Currently, the indicator has a resolution of $1\,\mu\varepsilon$, and puts out $0.465\,\mathrm{mV}/\mu\varepsilon$. If the output were to be amplified by 7×, it would show $3.25\,\mathrm{mV}/\mu\varepsilon$. This would at least bring the resolution of one microstrain to within the 3mV noiseband of the DAQ. The required range of microstrain readings necessary would depend on the material undergoing testing. Taking the example of graphite, with a fracture load of approximately 50N, the microstrain reading at this load would be $50/94480 \approx 530\mu\varepsilon$ (from Equation 5.4), which in turn would result in a required maximum voltage of $530 \times 3.25 = 1722.5$mV. The highest input voltage to the DAQ would then be taken as the next highest integer, in this case 2V. At 2V input, the resolution of the DAQ becomes $2/4096 = 0.49$mV, which is far below the resolution required for one microstrain. The danger, however, is that it is not only the DAQ which has uncertainty and noise, but also the strain indicator; by multiplying the output from the indicator one may also multiply its uncertainty to above that of the DAQ, which negates the purpose of the amplification exercise.

Additionally, the voltage drift mentioned in Section 5.4 did manifest itself during material testing. This was identified during cross-checking of the strain indicator reading and the voltage recording during loading. Figure 7.1 shows the full loading trace recorded during the testing of Specimen S123_3, while Table 7.1 compares the readings from the DAQ and the strain indicator at various points, marked as dots in Figure 7.1. The maximum error presented by the DAQ, taking the strain indicator value as sound, was 7.7%, identifying it as a major contributor to the overall uncertainty analysed in Section 5.5.

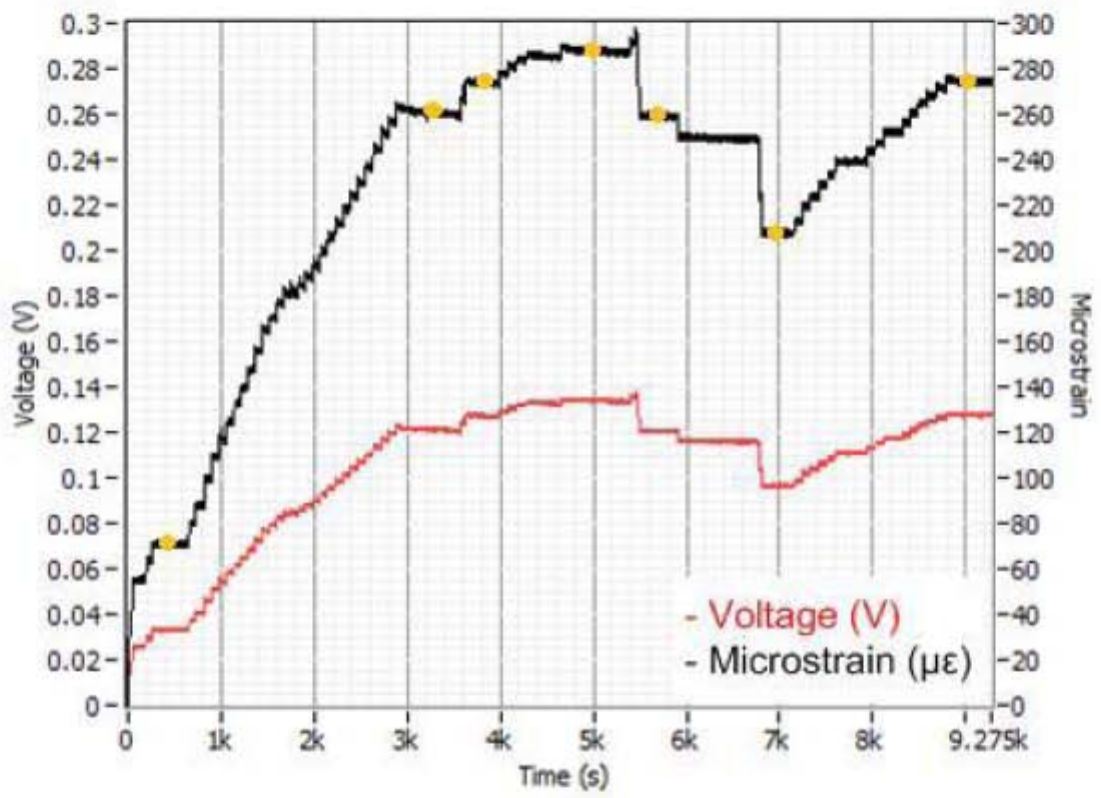


**Figure 7.1:** Full loading trace recorded during experiments with specimen S123_3. The dots mark the points where manual readings from the strain indicator were recorded.

### 7.3.2 Strain Indicator

The strain indicator worked well as a tool in this initial stage for checking against the DAQ figures in order to evaluate the performance of the DAQ. As a contributor to uncertainty, however, it could possibly be cut out in future experiments. A calibration of the load cells could be done using the DAQ system only, which has the capability to measure the resistance of a strain bridge. This would incorporate some of the uncertainty of the DAQ into the load cell calibration, and reduce the amount of connecting cabling between all the systems, thus also helping to reduce noise input.

### 7.3.3 Stepper Motor and Controller

The stepper motor was initially quite noisy in bench applications, in which there was a direct link between the motor and the rig shaft through one coupling. This coupling was, like the SEM/motor interface, initially a rigid coupling. It was found that substituting one universal joint for the rigid coupling smoothed the noise and reduced wobble on both the motor and the rig sides. One universal joint is suitable in this application as the misalignment between the motor and rig shafts is not great enough to cause a noticeable variation in velocity, as is sometimes apparent with only a single joint. Wobble from the driven SEM shaft to the rig was not apparent at all, due to the double joint system employed there.

The stepper motor controller was capable and functional, with all the required capabilities needed to conduct observations in the SEM on a smaller scale than has been done before. One negative aspect, forewarned in Appendix D, was its tendency to overheat and to cause the motor to overheat if a coil was inadvertently left energized, as in the 'pulse' mode when no pulsing is being commanded. Various options may be investigated, from current limiting to a temperature relay, or perhaps a modification of the switches used so that 'pulse' mode is not permanently selectable, reverting back to 'continuous' mode on release of the switch.

# Chapter 8

# Conclusions & Recommendations

The following chapter provides conclusions and recommendations for the miniature double torsion technique, in line with the lessons learnt from the system evaluation, as well as actual use during material testing. Basic conclusions are made concerning the material testing itself, and recommendations for possible future work on such material using the technique are given. It is recognized that the technique is beneficial in this field, and the types of observations made with it may be expanded upon in future.



## 8.1 Conclusions

With regard to the objectives given in Section 1.3, all were met. Referring to those objectives, the following conclusions are made about the success of this project:

### 8.1.1 The Apparatus

- A miniature version of the double torsion test rig was developed for use *in situ* inside a scanning electron microscope (SEM). It was evaluated on the bench using PMMA specimens, and *in situ* experiments were conducted on PMMA and nuclear graphite specimens. It was installed in the chamber of the UCT SEM housed in the Electron Microscope Unit. The rig interfaced well with the chamber and its performance was highly satisfactory. In particular, the key performance outcome was the superb control which could be achieved over the load applied to the specimen. The relevant design figures are:
  - An input gear ratio of 400:1, coupled with a lead screw of 0.5mm pitch, resulting in a crosshead displacement of 1.25 $\mu$m per motor revolution;

  - A coupled 48 step stepper motor reduced the achievable crosshead displacement to just over 26 nm per motor pulse;
  - The maximum achievable continuous speed of the motor was 96.5rpm, corresponding to a maximum crosshead displacement of 0.1mm/min;

- The following performance observations were made during material testing of nuclear graphite specimens, which had a reported fracture toughness of approximately 2.2 MPa$\sqrt{\text{m}}$:

  - 190 revolutions of the motor were required to induce damage noticeable on the load vs time output curve of a specimen – this damage was not yet visible to the naked eye;
  - A further 100 revolutions were required to produce visible damage;
  - The 290 revolutions to produce visible damage resulted in an applied load of 20.3N, approximately 0.07N per revolution.

- In tests of polymethylmethacrylate (PMMA) specimens, crack growth rates down to 19 nm/s were observed directly through live video capture.

- It was found that the rig and associated load cell could handle a large range of loads, but reached the upper limit of the initial coupling arrangement used at approximately 200N. The final coupling arrangement was not tested, but it is recommended that future tests not require loads above aproximately 150 - 200N.

From these observations, it can be seen that very fine control over loading rates can be achieved, thereby producing fine control over crack growth. Additionally, reading the load data and monitoring the load vs time trace proved to be a useful tool in identifying damage accumulation not yet visible in the SEM micrographs. This monitoring of output data can be used to mitigate the uncertainties resulting from not being able to observe subsurface behaviour in the material.

### 8.1.2 Nuclear Graphite

- Double torsion specimens of nuclear graphite, having a maximum grain size of $180 - 200\mu$m, provided by PBMR, were examined and fractured with the rig while inside the SEM. Due to the achievable loading rate of the rig, high-ramp rate fracture toughness tests were not performed. The experiments were

used to observe the damage development and cracking behaviour of nuclear graphite, by controlled fracture of the specimens.

- The influence of grain boundary microstructure, most notably the orientation of filler particles in the graphite matrix, was empirically confirmed. Evidence of crack tortuosity, as well as other friction-toughening mechanisms was provided. These observations agree with figures reported previously [5] which show higher fracture toughness values for cracks propagating perpendicular to the graphite extrusion direction, rather than parallel to it.

- Various other features of slow crack growth in nuclear graphite were presented, including crack jumping, branching, and diversion. It was shown that most (71% in the current observations) interactions of a main crack with a filler particle involve the crack diverting around the boundary of the particle, as opposed to passing through the particle. This confirms that the boundary between the filler and binder particles is the predominant source of weakness in the development of damage in the graphite matrix. However, the tortuous behaviour produced by the crack diverting between the randomly aligned filler particles contributed to an improved toughness for this material, than had the filler particles been aligned more uniformly parallel to the overall crack growth direction.

Given the above, it may be concluded that the objectives of the project were met. It is difficult to draw conclusions from the results as to the implications for graphite service life, but now that there is a greater understanding of the mechanisms which result in either toughening or weakening of the material, one may investigate the development of a technique to enhance the effect of one and diminish the other.

The *in situ* SEM double torsion facility provides an excellent technique for understanding the mechanisms of microfracture behaviour: of brittle materials in general, and nuclear graphite in particular.

## 8.2 Peripheral System Aspects

Certain aspects of the testing facility which was developed may be regarded as 'peripheral' to the main apparatus. That is the equipment which is commercial, or may be easily substituted with an alternative without dismantling the structure of the rig, or affecting its loading functionality. This section provides further comments regarding those aspects of the system, and their effect on its performance.

### 8.2.1 Load Cell

Load was measured via a strain-gauged steel bar, mounted between the supports of the device. Initially, two bars with a 5mm wide cross-section with differing thickness were evaluated: a 2mm thick bar, with a theoretical plastic limit of 62N, and a 4mm thick bar, with a theoretical plastic limit of 248N. The bars were evaluated in terms of their sensitivity to load, and their general suitability for the purpose.

The 4mm load cell was found to be sensitive enough for the graphite work, while being able to exhibit a wide range of values: just below $10\,\mu\varepsilon$ per Newton. It also contributed to more stable crack growth in PMMA specimens than the 2mm bar, and reduced the overall machine compliance relative to the thinner bar.

Despite the satisfactory qualitative performance of the load cell, its compliance behaviour is unknown. It is recommended that compliance tests be run on the load cell with a machine such as the ZWICK Universal Tensile Tester, in order to determine its contribution to the overall load trace presented for different materials, and particularly for the interpretation of the load traces presented for the graphite in this report.

As a further note, the calibration of the load cell contributed the greatest amount of uncertainty to the load reading capability of the system. This was a result of the use of a 5kN load cell to measure load on the testing machine – the smallest available at the time. An attempt should be made to verify the results of the calibration using a suitably sized load cell, thereby greatly reducing the level of uncertainty which currently exists in the load retrieval train.

### 8.2.2 Stepper Motor

A 7.5° stepper motor was coupled to the input shaft of the DT rig, enabling 48 incremental pulses per full motor revolution. The coupling was made through a flexible tube attachment from the motor to the SEM interface, and a double universal joint series arrangement from the SEM interface to the rig, which compensated for parallel misalignment between the interface and rig input shafts.

Whilst a stepper motor is, by default, a 'noisy' motor, the substitution of universal joints and flexible couplings for rigid methods diminished the effects of vibration from the stepper motor considerably. The use of two universal joints in series also ensured the input motion was constant relative to the motor shaft. This contributed to the stable loading performance of the rig, and its ability to induce a controlled crack at a slow rate in the test material.

The strength of the motor in this application was its slow rotation capability,

although this could in turn be a limitation if the ability to do fast ramping load tests is required for fracture mechanics experiments. If a faster motor, or more precision, is need, a servomotor should be considered. The stepper motor does however remain the simpler electronic solution, especially in terms of possible expansion to computer controlled loading sequences.

### 8.2.3 Strain Indicator

A P3500 strain indicator was used to read the strain values directly from the strain gauges mounted on the load cell (see 8.2.1).

It proved a useful tool in terms of providing an at-a-glance idea of the loads being experienced, but contributed approximately 0.75N to the overall uncertainty in the final recorded load, due to drift and noise. Although this was the smallest source of uncertainty in the setup, the possibility of eliminating the strain indicator should be investigated. Tests should be run with the load cell wires connected straight to the DAQ, to see if the resulting signal is strong enough or if the possibility of independent amplification should be investigated.

If the strain indicator is to be used, it is recommended that a gain should be applied to its voltage output in order to overcome the noise inherent in the DAQ. The maximum voltage input to the DAQ in the graphite tests was 1V, out of an available capacity of 10V. It was calculated that the output from the indicator could be amplified by as much as 7× before the maximum expected load produced in graphite tests would exceed the input capacity of the DAQ.

This section has discussed the performance of some of the peripheral devices, external to the rig structure, employed in the experimental setup. Comment was made on their perceived suitability after having gained experience using them, and the recommendations made were based on this experience, so ensuring a more refined total system in the future. The final section describes future developments and research which may be applied using the current device as a starting point.

## 8.3 Future Work

- There is potential for computer automation of the stepper motor controller. This would allow for very precise loading routines, which enables the design of tests in line with constant-load and constant-displacement techniques, but on a very small scale. A subroutine for LabView SignalExpress would have to be

developed where the DAQ receives input data and compares it to a signal from the load cell, which prompts a corrective signal to the motor. The frequency response of both the motor and the DAQ should be tested to see whether a setup such as this would be efficient.

- Provision was made in the original design to install a heating stage below the specimen mounts. If this were incorporated, the current experiments could be reperformed at various temperatures, in order to observe and compare any changes at this scale. The heat transfer characteristics of the SEM chamber should be investigated before this is done, however. Although the environment is a vacuum, any accidental transmission of excessive heat (due to leakage, etc.) could damage components integral to the microscope chamber.

# References


[1] Integrated Resource Plan for Electricity. Revision 2. 2011. http://www.doe-irp.co.za/content/IRP2010_2030_Final_Report_20110325.pdf - [Last Accessed: 06 April 2011]

[2] PBMR Ltd. Why PBMR? http://www.pbmr.co.za/index.asp?Content=229 - [Last Accessed: 18 January 2010]

[3] Schubert, F.; Nickel H. & Breitbach, G. 1991. Structure design criteria for HTR - a summary report. *Nuclear Engineering and Design*, 132: 75 - 84. Elsevier Science B.V.

[4] Tsang, D.K.L & Marsden, B.J. 2006. The development of a stress analysis code for nuclear graphite components in gas-cooled reactors. *Journal of Nuclear Materials*, 350: 208 - 220. Elsevier B.V.

[5] Becker, T.H. 2010. Understanding and Modeling the Damage and Fracture Characteristics of Nuclear Grade Graphite. PhD Thesis, University of Cape Town. Unpublished, Cape Town.

[6] Gerry, D.J. 1966. PhD Thesis, University of Vermont. Reported in [11].

[7] Kies, J.A. & Clark, B.J. 1969. *Fracture 1969:* 483. London: Chapman Hall.

[8] Chevalier, J.; Saadaoui, M.; Olagnon, C. & Fantozzi, G. 1996. Double torsion testing a 3y-TZP ceramic. *Ceramics International*, 22(2): 171 - 177.

[9] Vekinis, G.; Ashby, M.F. & Beaumont, P.W.R. 1990. *R*-Curve behaviour of $Al_2O_3$ ceramics. *Acta Metallurgica Et Materialia*, 38(6): 1151 - 1162. Pergamon Press, Ltd.

[10] Salem, J.A.; Radovic, M.; Lara-Curzio, E. & Nelson, G. 2006. Fracture Toughness of Thin Plates by the Double-Torsion Test Method. Submitted to Ceramic Engineering and Science Proceedings.

[11] Tait, R.B.; Fry, P.R. & Garrett, G.G. 1987. Review and Evaluation of the Double-Torsion Technique for Fracture Toughness and Fatigue Testing of Brittle Materials. *Experimental Mechanics*, 27(1): 14 - 22, March. Springer Science.

[12] Becker, T.H. 2008. The Double Torsion Beam Technique: An Experimental Evaluation of the Technique, and its Application to Nuclear Graphite. Unpublished MSc Thesis, University of Cape Town.

[13] Becker, T.H.; Marrow, T. J & Tait, R.B. 2011. An Evaluation of the Double Torsion Technique. *Journal for Experimental Mechanics*, DOI 10.1007/s11340-011-9468-1. Published online: 19 February 2011.

[14] Higgins, D.D. & Bailey, J.F. 1976. *Proceedings of the conference on hydraulic cement pastes: their structure and properties*, 283 - 296. Sheffield: Cement and Concrete Association.

[15] Roberts, W.; Lehtinen, B. & Easterling, K.E. 1976. An in situ SEM study of void development around inclusions in steel during plastic deformation. *Acta Metallurgica*, 24(8): 745 - 758. Elsevier, Ltd.

[16] Akers, S.A.S.; Garrett, G.G. & Tait, R.B. 1977. In-situ scanning electron microscope observations of flexural failure of asbestos cement. *Proceedings of EMSSA*, 7: 57. Electron Microscopy Society of Southern Africa.

[17] Davidson, D.L. & Nagy, A. 1978. A low frequency cyclic loading stage for the SEM. *Journal of Physics E: Scientific Instruments*, 11: 207 - 210. Institute of Physics Publishing Ltd.

[18] Davidson, D.L. & Lankford, J. 1979. Dynamic real time fatigue crack propagation at high resolution as observed in the SEM. *Internationl Journal of Fracture*, 17(3): 257 - 275. Springer Science.

[19] Vehoff, H. & Neumann, P. 1979. In situ SEM experiments concerning the mechanism of ductile crack growth. *Acta Metallurgica*, 27(5): 915 - 920. Elsevier, Ltd.

[20] Manning, M.I. & Goodhew, D.J. 1979. An hydraulic straining stage of use in scanning electron microscopes. *International Journal of Fracture*, 12: 464 - 466. Springer Science.

[21] Tait, R.B. & Bohm, H. 1980. In situ SEM examination of double torsion fracture of concrete. *Proceedings of EMSSA*, 10: 29. Electron Microscopy Society of Southern Africa.

[22] Mindess, S. & Diamond, S. 1982. A device for direct observation of cracking of cement paste or mortar under compressive loading within a scanning electron microscope. *Cement and Concrete Research*, 12: 569 - 576. Elsevier, Ltd.

[23] Nagy, A. & Campbell, J.B. & Davidson, D.L. 1984. A high temperature cyclic loading stage for the SEM. *Review of Scientific Instruments*, 55: 778 - 782. American Institute of Physics.

[24] Tait, R.B.; Akers, S.A.S.; Gerneke, D.A.; Schultes, K.S. 1988. Dynamic in situ load deflection testing of fibre cement composites in the SEM. *Proceedings of EMSSA*, 18: 39 - 40. Durban: Electron Microscopy Society of Southern Africa.

[25] Tait, R.B. & Garrett, G.G. 1986. Direct observation of fracture in brittle materials in the SEM using a double torsion testing technique. *Scanning*, 8: 129 - 138. FACM, Inc.

[26] Tait, R.B. & Garrett, G.G. 1986. In situ double torsion fracture studies of cement mortar and cement paste inside a scanning electron microscope. *Cement and Concrete Research*, 16: 143 - 155. Pergamon Press, Ltd.

[27] Ewalds, H.L. & Wanhill, R.J.H. 1989. *Fracture Mechanics*. London: Edward Arnold.

[28] Ortiz, M. 1988. Microcrack coalescence and macroscopic crack growth initiation in brittle solids. *International Journal of Solids and Structures*, 24(3): 231 - 250. Pergamon Press, Ltd.

[29] Koster, A.; Matzner, H.D. & Nicholsi, D.R. 2003. PBMR design for the future. *Nuclear Engineering and Design*, 222: 231 - 245. Elsevier Science B.V.

[30] Quadakkers, W.J. 2004. Corrosion of High Temperature Alloys in the Primary Circuit Helium of High Temperature Gas Cooled Reactors. Part II: Experimental Results. *Materials and Corrosion*, 36(8): 335 - 347. Verlag GmbH & Co.

[31] Xiaowei, L.; Jean-Charles, R. & Suyuan, Y. 2004. Effect of temperature on graphite oxidation behavior. *Nuclear Engineering and Design*, 227: 273 - 280. Elsevier, B.V.

[32] Hacker, P.J.; Neighbour, G.B. & McEnaney, B. 2000. The coefficient of thermal expansion of nuclear graphite with increasing thermal oxidation. *Journal of Physics D: Applied Physics*, 33: 991 - 998. Institute of Physics Publishing Ltd.

[33] Mitchell, B.C.; Smart, J.; Fok, S.L. & Marsden, B.J. 2003. The mechanical testing of nuclear graphite. *Journal of Nuclear Materials*, 322: 126 - 137. Elsevier B.V.

[34] Ishiyama, S.; Burchell, T.D.; Strizak, J.P. & Eto, M. 1996. The effect of high fluence neutron irradiation on the properties of a fine-grained isotropic nuclear graphite. *Journal of Nuclear Materials*, 230: 1 - 7. Elsevier Science B.V.

[35] Ouagne, P.; Neighbour, G.B. & McEnaney, B. 2002. Crack growth resistance in nuclear graphites. *Journal of Physics D: Applied Physics*, 35: 927 - 934. Institute of Physics Publishing Ltd.

[36] Salazar, A.; Pastor, J.Y. & Llorca, J. 2002. In situ observation of damage nucleation in graphite and carbon/carbon composites. *Carbon*, 40: 609 - 616. Elsevier Science Ltd.

[37] Shi, L. *et al.* 2008. Analysis of crack propagation in nuclear graphite using three-point bending of sandwiched specimens. *Journal of Nuclear Materials*, 372: 141 - 151. Elsevier B.V.

[38] Nemeth, N.N. & Bratton, R.L. 2010. Overview of statistical models of fracture for nonirradiated nuclear-graphite components. *Nuclear Engineering and Design*, 240: 1 - 29. Elsevier B.V.

[39] Berre, C. *et al.* 2008. Failure analysis of the effects of porosity in thermally oxidised nuclear graphite using finite element modelling. *Journal of Nuclear Materials*, 381: 1 - 8. Elsevier B.V.

[40] Zou, Z.; Fok, S.L.; Oyadiji, S.O. & Marsden, B.J. 2004. Failure predictions for nuclear graphite using a continuum damage mechanics model. *Journal of Nuclear Materials*, 324: 116 - 124. Elsevier B.V.

[41] Tucker, M.O. 1979. The application of fracture mechanics to the notch sensitivity of graphite. In: IAEA technical committee meeting on mechanical behaviour of graphite for high temperature reactors. IAEA, France. Available online: http://iaea.org/inisnkm/nkm/aws/htgr/fulltext/iwghtr3_9.pdf - [Last Accessed: 5 January 2010]

[42] Burchell, T.D. 1995. A microstructurally based fracture model for polygranular graphites. *Carbon*, 34(3): 297 - 316. Elsevier Science Ltd.

[43] Jones, A.N. *et al.* 2008. Microstructural characterisation of nuclear grade graphite. *Journal of Nuclear Materials*, 381: 152 - 157. Elsevier B.V.

[44] Joyce, M.R.; Marrow, T.J.; Mummery, P. & Marsden, B.J. 2008. Observation of microstructure deformation and damage in nuclear graphite. *Engineering Fracture Mechanics*, 75: 3633 - 3645. Elsevier Ltd.

[45] Wen, K.; Marrow, J. & Marsden, B. 2008. Microcracks in nuclear graphite and highly orientated pyrolytic graphite (HOPG). *Journal of Nuclear Materials*, 381: 199 - 203. Elsevier B.V.

[46] Srinivasan, M. 2008. On estimating the fracture probability of nuclear graphite components. *Journal of Nuclear Materials*, doi:10.1016/j.jnucmat.2008.07.029. Available online.

[47] Broek, D. 1988. *The Practical Use of Fracture Mechanics*. The Netherlands: Kluwer Academic Publishers.

[48] Bradt, R.C. 1983. *Fracture Mechanics of Ceramics*. Plenum Pub. Corp. Reported in [12].

[49] Wang, X-S.; Wu, B-S. & Wang, Q-Y. 2005. Online SEM investigation of microcrack characteristics of concretes at various temperatures. *Cement and Concrete Research*, 35: 1395 - 1390. Elsevier, Ltd.

[50] Tait, R.B. 2005. In situ scanning electron microscope fracture and crack growth studies at the micron level. Powerpoint presentation for University of Stellenbosch.

[51] Hall, G.; Marsden, B.J. & Fok, S.L. 2006. The microstructural modelling of nuclear grade graphite. *Journal of Nuclear Materials*, 353: 12 - 18. Elsevier B.V.

[52] Ding, Y.; Wang, C.; Li, M. & Bang, H-S. 2005. In-situ SEM observation on fracture behaviors on Sn-based solder alloys. *Journal of Materials Science*, 40: 1993 - 2001. Springer Science.

[53] Evans, A.G. 1972. A method for evaluating the time-dependent failure characteristics of brittle materials - and its application to polycrystalline alumina. *Journal of Materials Science*, 7(10): 1137 - 1146.

[54] Shyam, A. & Lara-Curzio, E. 2006. The double-torsion testing technique for determination of fracture toughness and slow crack growth behavior of materials: A review. *Journal of Materials Science*, 41(13): 4093 - 4104. Springer Science.

[55] Fuller, E.R. Jr. 1979. An Evaluation of Double Torsion Testing - Analysis. *Fracture Mechanics Applied to Brittle Materials. ASTM STP 678*: 3 - 18. S.W. Freiman, Ed., American Society for Testing and Materials.

[56] Pollet, J.C. & Burns, S.J. 1979. Crack velocity correction factor for the crack front shape in double torsion specimens. *Journal of the American Ceramics Society*, 62(7): 426 - 427. Reported in [13]

[57] Leevers, P.S. 1986. Large deflection analysis of the double torsion test. *Journal of Materials Science Letters*, 5(2): 191 - 192.

[58] Ciccotti, M.; Negri, N.; Gonzato, G. & Mulargia, F. 2001. Practical application of an improved methodology for the double torsion load relaxation method. *International Journal of Rock Mechanics and Mining Sciences*, 38(4): 469 - 576. Reported in [13].

[59] Pletka, B.J.; Fuller, E.R., Jr. & Koepke, B.G. 1979. An Evaluation of Double Torsion Testing - Experimental. *Fracture Mechanics Applied to Brittle Materials. ASTM STP 678*: 19 - 37. S.W. Freiman, Ed., American Society for Testing and Materials.

[60] Albuquerque, M.C.F. & Rodrigues, J.A. 2008. Study of the Dimensions of Double-Torsion Test Specimens. *Materials Research*, 11(3): 281 - 288.

[61] The Electron Microscope Unit. SEM School: Notes on Scanning Electron Microscopy. http://sbio.uct.ac.za/Webemu/SEM_school/index.php - [Last Accessed: 13 January 2010]

[62] Leica Cambridge Ltd. (pub). 1993. *Stereoscan 440 Operator Manual*. Version 1. Cambridge, England.

[63] Xu, X.H.; Wang, G.; Ke, F.J. & Wang, W.H. 2008. In situ observations on the fracture process of metallic glassy ribbons. *Scripta Materiala*, 59: 657 - 660. Elsevier, Ltd.

[64] Wang, X-S. *et al.* 2008. SEM in-situ investigation on failure of nanometallic film/substrate structures under three-point bending loading. *International Journal of Fracture*, 151: 269 - 279. Springer Science.

[65] Ghisleni, R. *et al.* 2009. In situ SEM indentation experiments: instruments, methodology, and applications. *Microscopy Research and Technique*, 72: 242 - 249. Wiley-Liss, Inc.

[66] Yawny, A.; Malarria, J.; Soukup, E. & Sade, M. 1997. Stage for in situ mechanical loading experiments in a scanning electron microscope (Philips 515) with a small chamber. *Review of Scientific Instruments*, 68(1): 150 - 154. American Institute of Physics.

[67] Sørensen, B.F.; Horsewell, A.; Jørgensen, O. & Kumar, A.N. 1998. Fracture resistance measurement method for in situ observation of crack mechanisms. *Journal of the American Ceramic Society*, 81(3): 661 - 669.

[68] Frotscher, M. *et al.* 2008. In situ scanning electron microscopic study of structural fatigue of struts, the characteristic elementary building units of medical stents. *Materials Science and Engineering A*, 481 - 482: 160 - 165. Elsevier B.V.

[69] LoadTech Load Cells. *s.a.* An introduction to foil strain gauge based load cells. *Engineer's Technical Handbook*. Melville, Gauteng: Red Bird Media: 165 - 166.

[70] National Instruments Corporation. 2009. Measuring Strain with Strain Gages. http://zone.ni.com/devzone/cda/tut/p/id/3642 - [Last Accessed: 13 January 2010]

[71] Wikipedia.com. 2010. *Scanning Electron Microscope*. http://en.wikipedia.org/wiki/Scanning_electron_microscope - [Last Accessed: 13 January 2010]

[72] Lagattu, F.; Bridier, F.; Villechaise, P. & Brillaud, J. 2006. In-plane strain measurements on a microscopic scale by coupling digital image correlation and an in situ SEM technique. *Materials Characterization*, 56: 10 - 18. Elsevier Inc.

[73] Davidson, D.L. 1979. The observation and measurement of displacement and strain by stereoimaging. *Scanning Electron Microscopy/1979/II*: 79 - 86. SEM Inc, AMF O'Hare.

[74] Tait, R.B. 1990. Microcrack fracture zone studies using stereo imaging. *Proceedings of EMSSA*, 20: 33 - 34. Grahamstown: Electron Microscopy Society of Southern Africa.

[75] Tatschl, A. & Kolednik, O. 2003. A new tool for the experimental characterization of micro-plasticity. *Materials Science & Engineering A*, A339: 265 - 280. Elsevier Science B.V.

[76] Waldron, Miranda. 2010. UCT SEM operator. Conversations with the author during 2010, Cape Town.

[77] Tait, R.B. & Cekiso, K. 2009. Images captured as part of an undergradute thesis underway at the University of Cape Town in October 2009. Cape Town, University of Cape Town.

[78] Tait, R.B. & Becker, T. 2007. Fracture toughness testing of graphite; Round robin test series. Internal Report, University of Cape Town.

[79] Donsteel & Forgings. *s.a.* Technical information: AISI 1055 key steel.

[80] MatWeb Material Property Data. 2010. Data sheet for AISI 1055 Steel, hot rolled. http://www.matweb.com/search/DataSheet.aspx?MatGUID=c40f8cc77d5e46e1af49f7173abf34f9 [Last Accessed: 11 November 2010]

[81] CME Metrology cc. 2010. Calibration Certificate for 10kN load cell, part no. 08-4075. Calibration performed by T. Thompson, March 2010. University of Cape Town.

[82] Crowcroft, P. 2004. K179 Unipolar Steppermotor Driver. http://kitsrus.com/pdf/k179.pdf [Last Accessed: 26 January 2011]

[83] Hewes, J. 2010. 555/556 Monostable. http://www.kpsec.freeuk.com/555timer.htm [Last Accessed: 07 March 2011]

# Appendix A

# Manufacturing Drawings

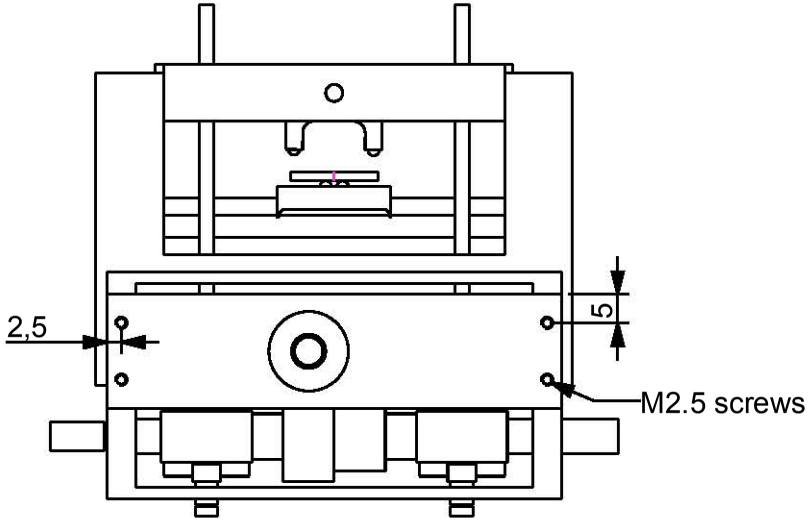


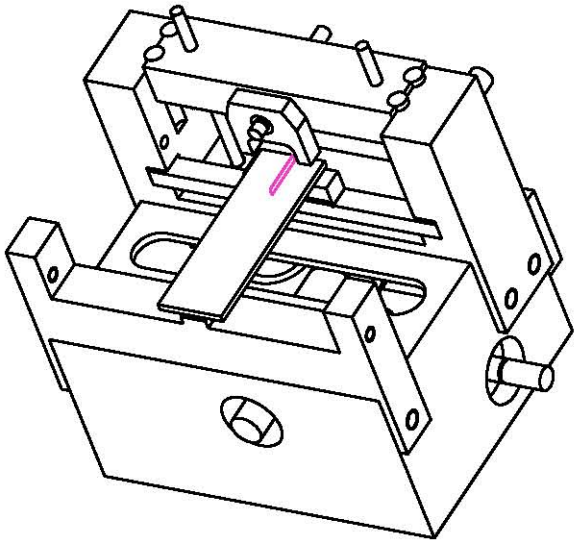

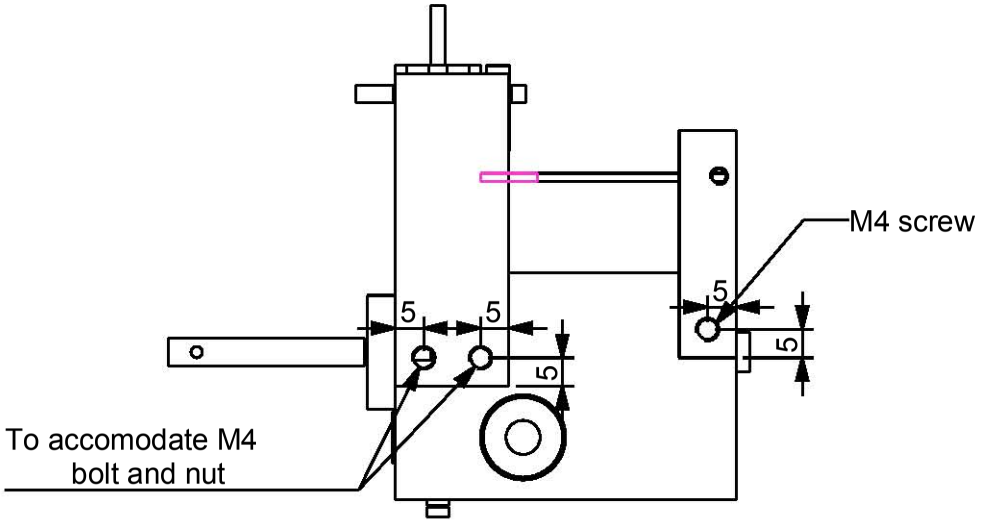


| Item | Name | Qty | Material |
|---|---|---|---|

| | | | | |
|---|---|---|---|---|
| | University of Cape Town<br>Department of Mechanical Engineering | | | |
| | Title<br>Total Assembly | | | |
| Dimensions in mm<br>Tolerance U.O.S.<br>0.1 | Scale<br>0,650 | Date<br>07/05/2010 | Sheet<br>1 | of<br>12 |
| | Drawn By<br>Kathryn Rosie | | Drawing Number<br>-- | |

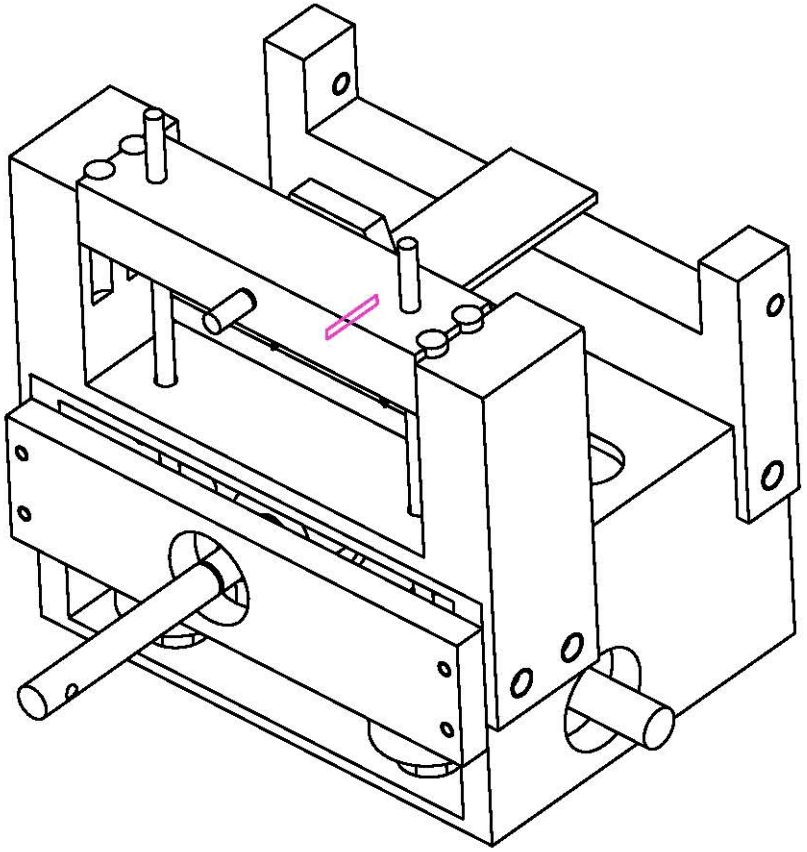

| Item | Name | Qty | Material |
|---|---|---|---|

University of Cape Town
Department of Mechanical Engineering

Title: DRIVE ASSEMBLY

| Dimensions in mm Tolerance U.O.S. | Scale | Date | Sheet | of |
|---|---|---|---|---|
| 0.1 | 1,000 | 07/05/2010 | 2 | 12 |

| Drawn By | Drawing Number |
|---|---|
| Kathryn Rosie | -- |

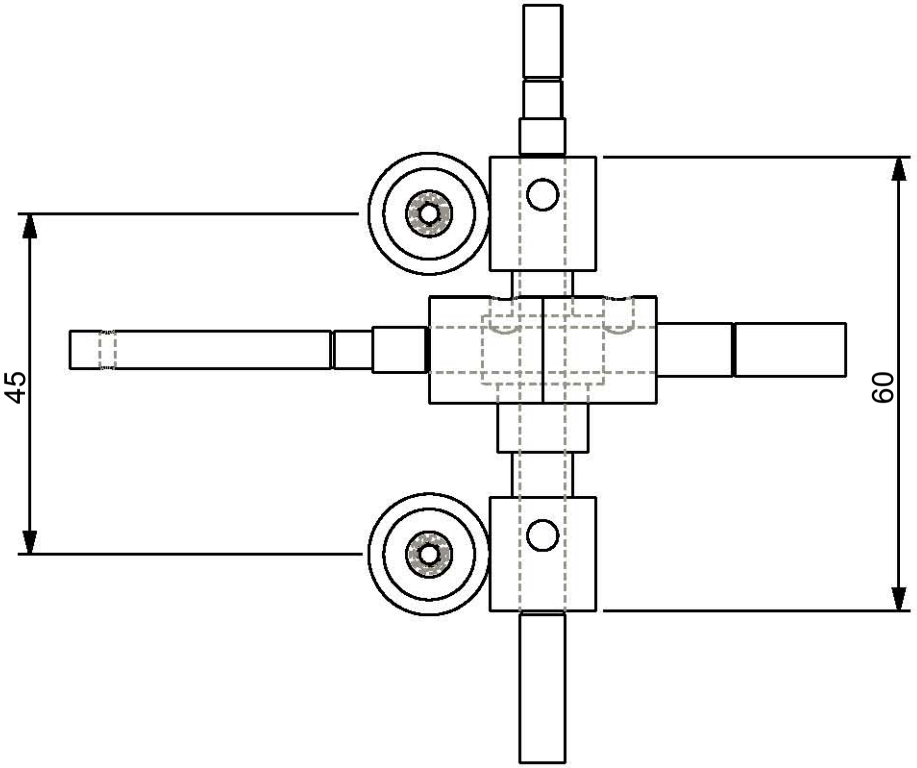


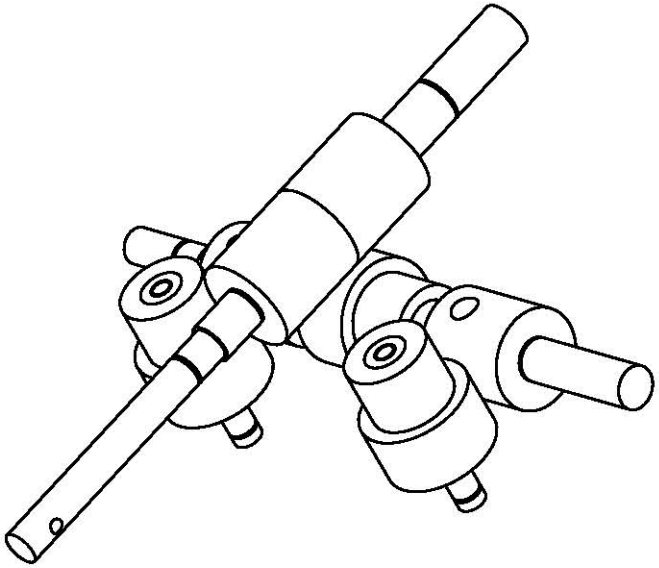

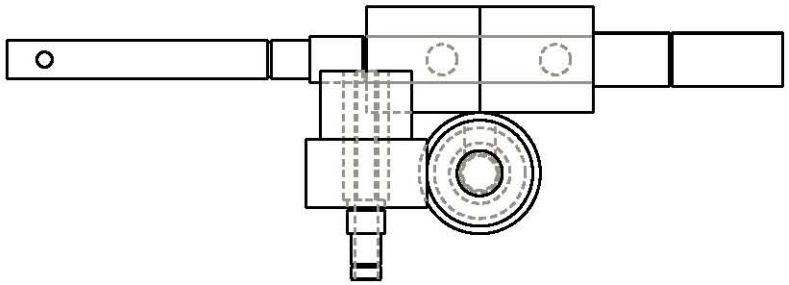

| Item | Name | Qty | Material |
|---|---|---|---|
| 4 | INTERMEDIATE_SHAFT | 1 | |
| 3 | INPUT_SHAFT | 1 | |
| 2 | NUT | 2 | SST |
| 1 | NUTGEAR | 2 | BRASS |

University of Cape Town
Department of Mechanical Engineering

Title
DRIVE ASSEMBLY

| Dimensions in mm Tolerance U.O.S. | Scale | Date | Sheet | of |
|---|---|---|---|---|
| | 1,000 | 21/04/2010 | 2a | 12 |
| | Drawn By | | Drawing Number | |
| 0.1 | Kathryn Rosie | | -- | |

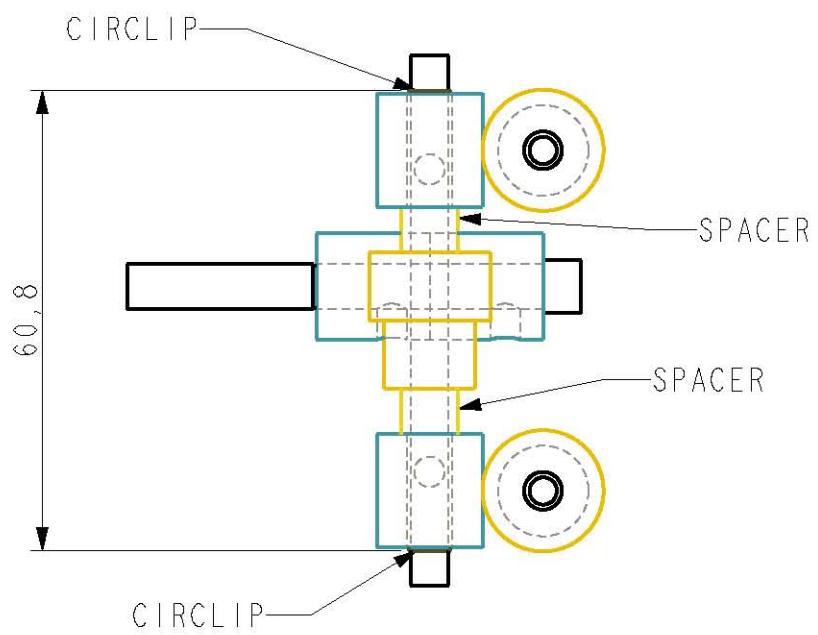


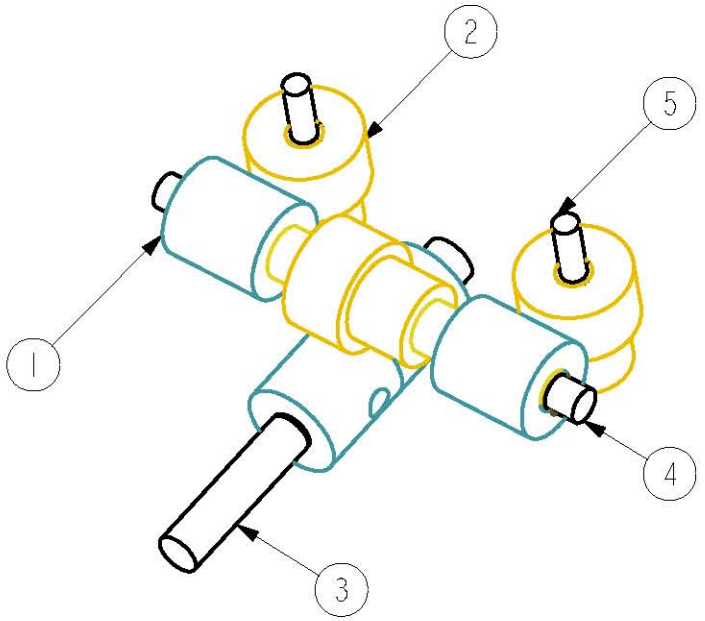


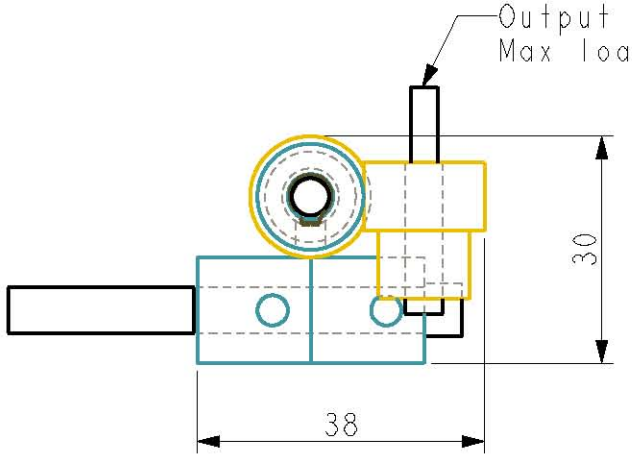


Required reduction: ±400:1

| Item | Name | Qty | Material |
|---|---|---|---|
| 5 | FEMALE THREAD | | |
| 4 | INTERMEDIATE SHAFT | | |
| 3 | INPUT SHAFT | | |
| 2 | WORM GEAR | 3 | BRASS |
| 1 | WORM | 3 | BRASS |

University of Cape Town
Department of Mechanical Engineering

Title: DRIVE ASSEMBLY MOCK-UP

| Dimensions in mm Tolerance U.O.S. | Scale | Date | Sheet | of |
|---|---|---|---|---|
| 0.1 | 1,000 | 16/03/2010 | 1 | 1 |
| | Drawn By: Kathryn | | Drawing Number: 1 | |

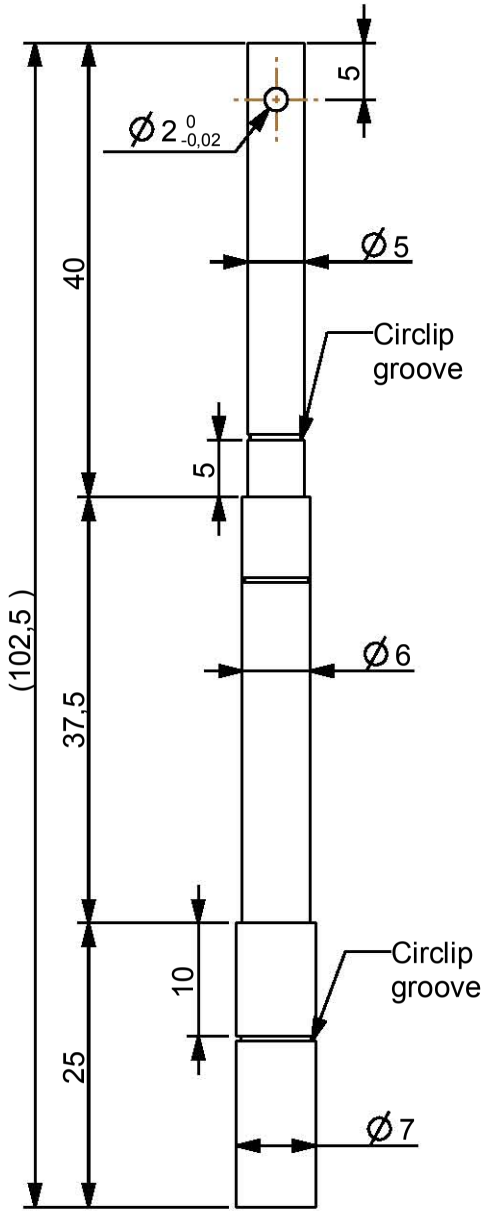


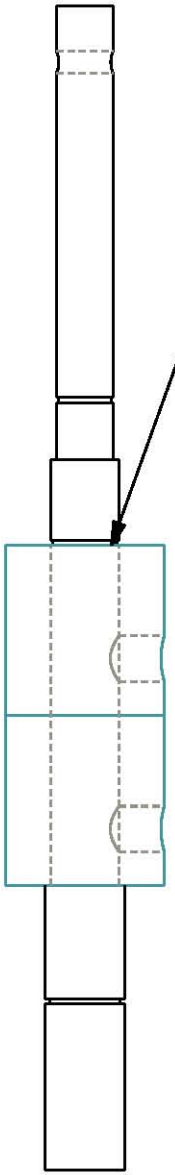


Shaft/bush: Sliding fit (H7/g6)
Shaft/gear: Locational transition fit (H7/k6)

| | | | |
|---|---|---|---|
| 2 | INPUT_SHAFT | 1 | SST |
| 1 | WORM | 1 | BRASS |
| Item | Name | Qty | Material |

University of Cape Town
Department of Mechanical Engineering

Title
INPUT SHAFT ASSEMBLY

| | | | | |
|---|---|---|---|---|
| Dimensions in mm Tolerance U.O.S. | Scale 1,500 | Date 21/04/2010 | Sheet 3 | of 12 |
| | Drawn By Kathryn Rosie | | Drawing Number -- | |
| 0.1 | | | | |

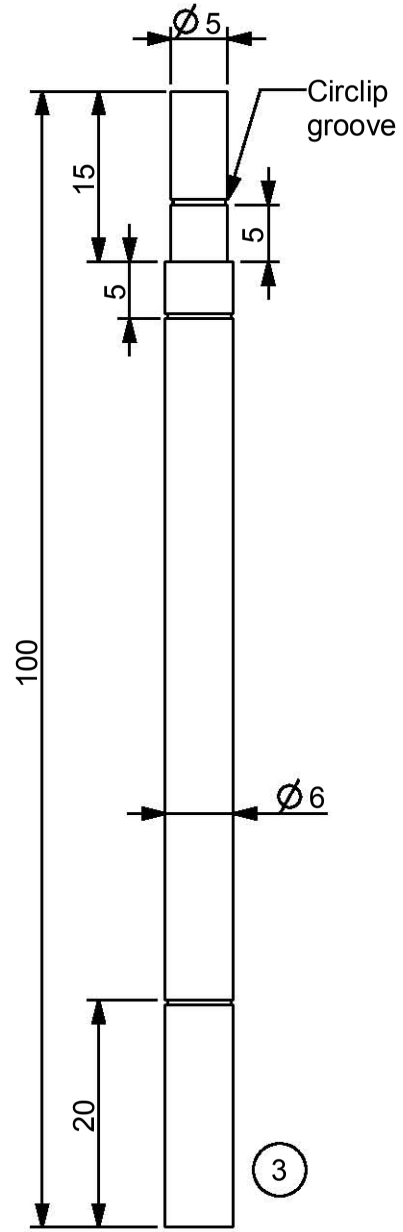


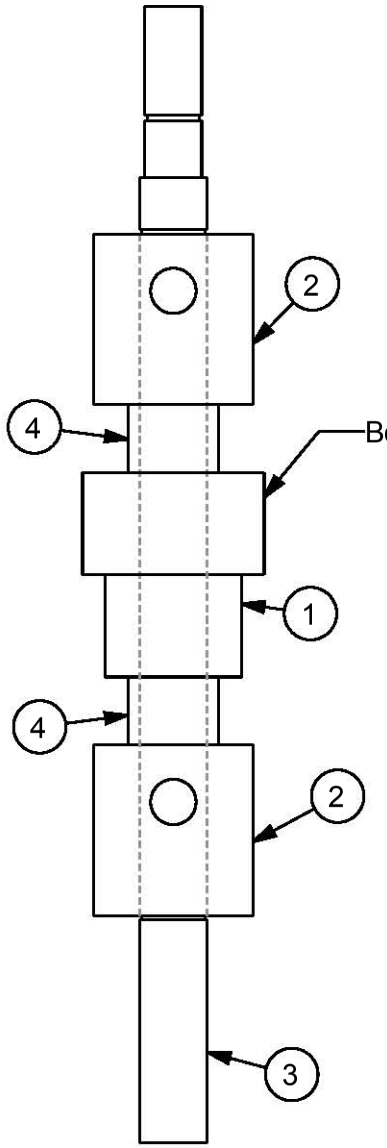


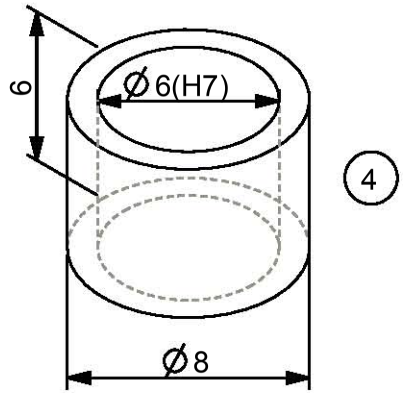


Ø6(H7)

Shaft/bush: Sliding fit (H7/g6)
Shaft/gear: Locational transition fit (H7/k6)

| Item | Name | Qty | Material |
|---|---|---|---|
| 4 | SPACER | 2 | SST_304 |
| 3 | INTERMEDIATE_SHAFT | 1 | SST |
| 2 | WORM | 2 | BRASS |
| 1 | GEAR | 1 | BRASS |

University of Cape Town
Department of Mechanical Engineering

Title: Intermediate Shaft & Assembly

| Dimensions in mm Tolerance U.O.S. | Scale | Date | Sheet | of |
|---|---|---|---|---|
| 0.1 | 1,500 | 07/05/2010 | 4 | 12 |
| | Drawn By: Kathryn Rosie | | Drawing Number: -- | |

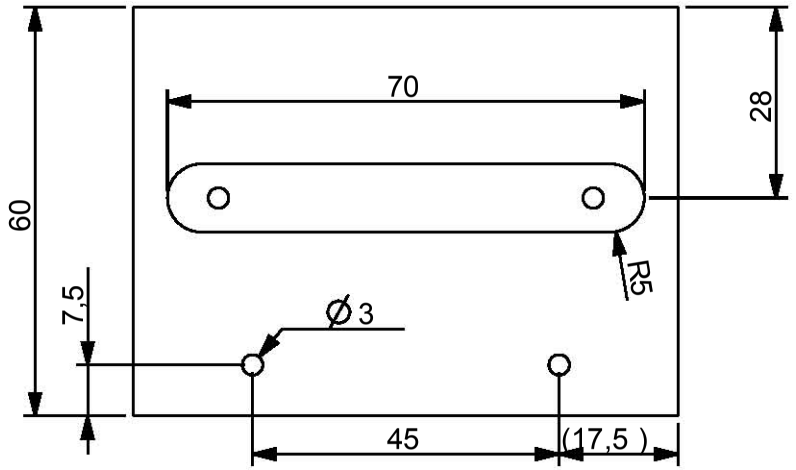


3

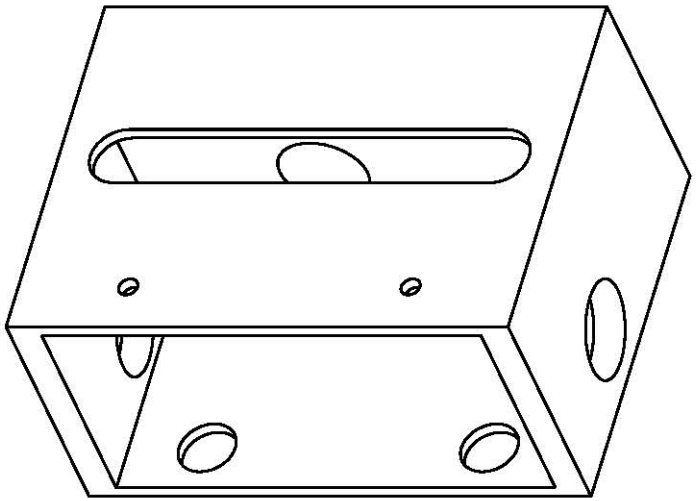

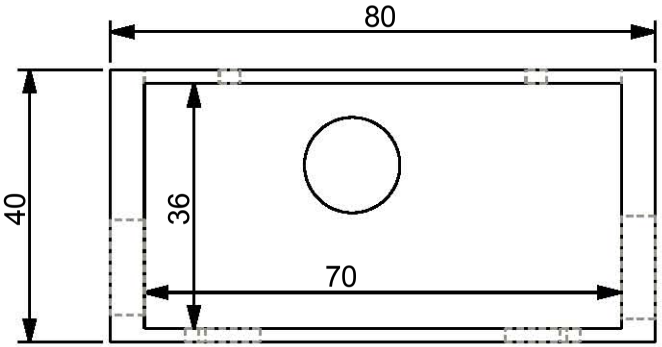


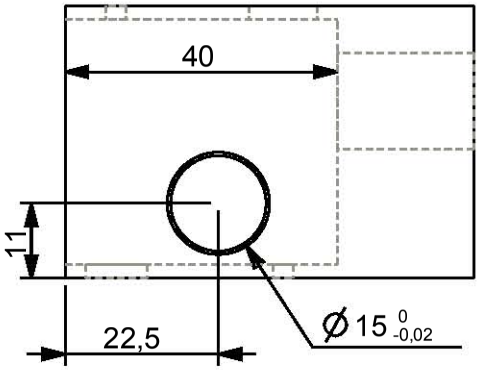


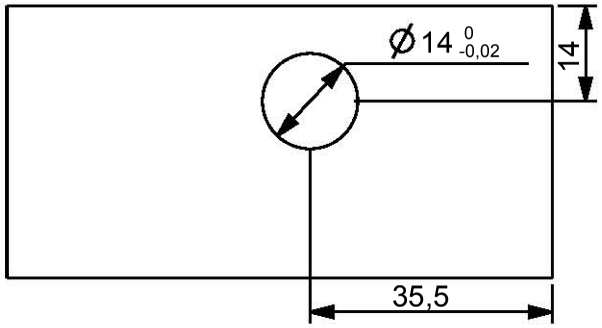


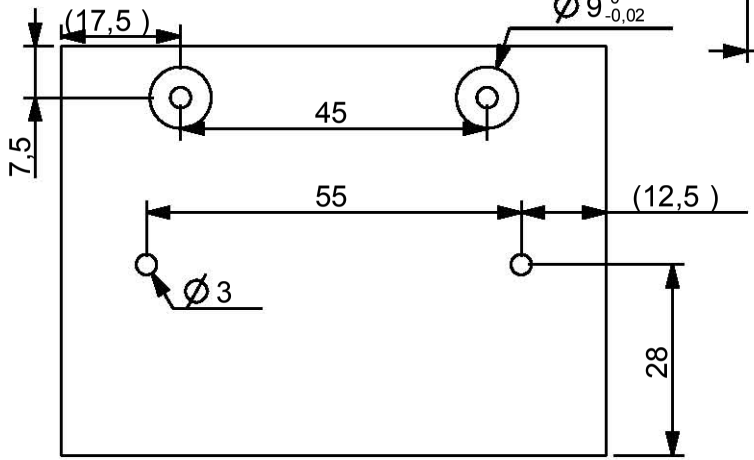


All holes H7
Base/bushes: H7/p6

| Item | Name | Qty | Material |
|---|---|---|---|

| | | | | |
|---|---|---|---|---|
| | University of Cape Town<br>Department of Mechanical Engineering | | | |
| | Title: BASE | | | |
| Dimensions in mm<br>Tolerance U.O.S.<br>0.1 | Scale: 0,900 | Date: 07/05/2010 | Sheet: 5 | of: 12 |
| | Drawn By: Kathryn Rosie | | Drawing Number: -- | |

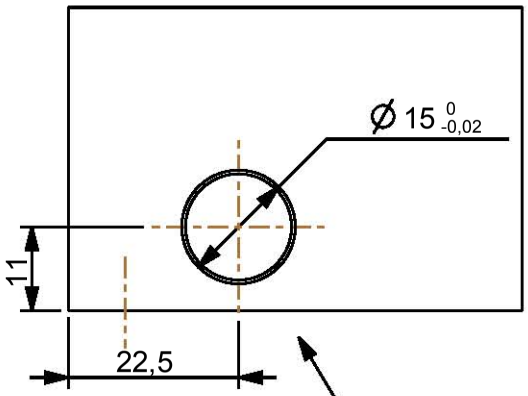


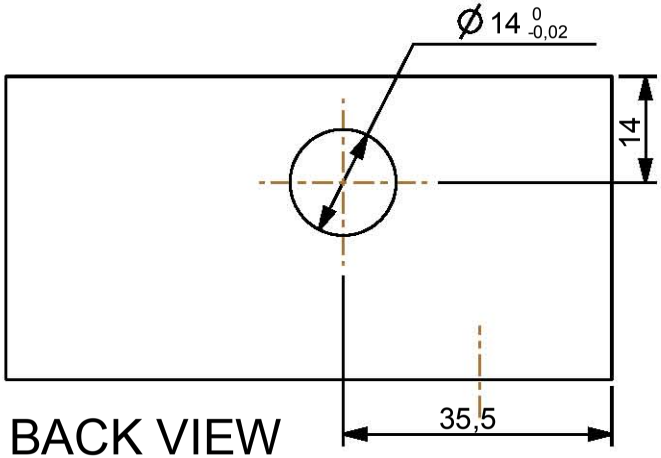


BACK VIEW

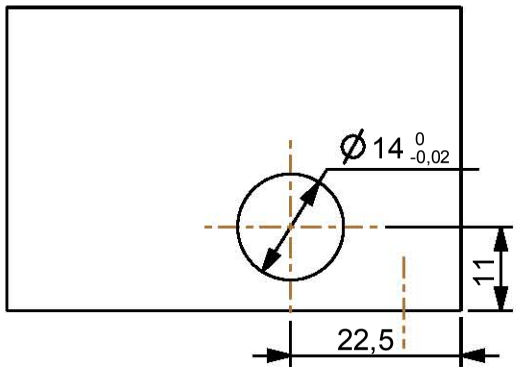


Note different Ø hole directly opposite on other wall

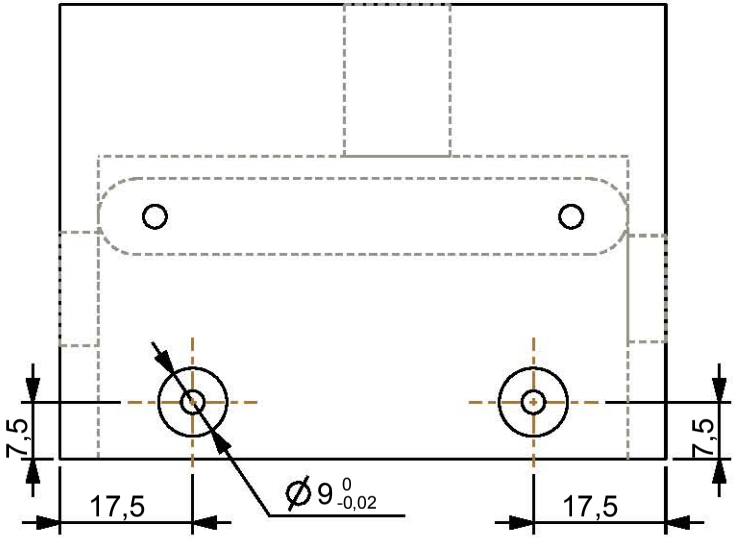


| | | | |
|---|---|---|---|
| Item | Name | Qty | Material |
| | University of Cape Town<br>Department of Mechanical Engineering | | |
| | Title: Bearing hole modifications | | |
| Dimensions in mm<br>Tolerance U.O.S.<br>0.1 | Scale: 1,000 | Date: 29-Jun-10 | Sheet: 6 of 12 |
| | Drawn By: Kathryn Rosie | | Drawing Number: -- |

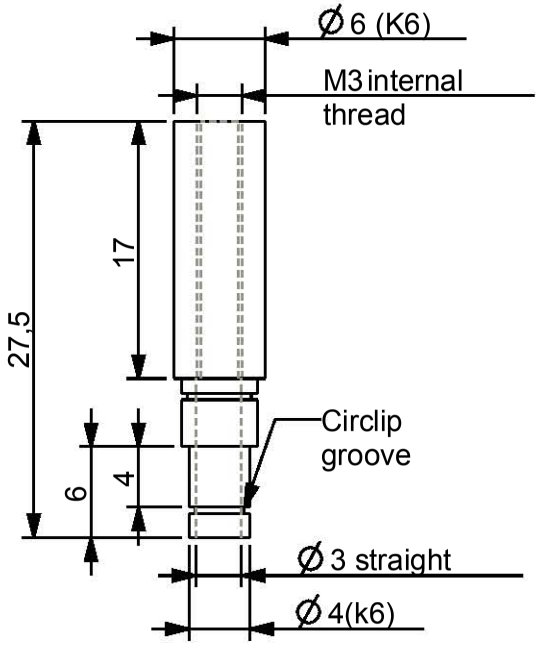


2

Gear/nut: Locational transition fit (H7/k6)

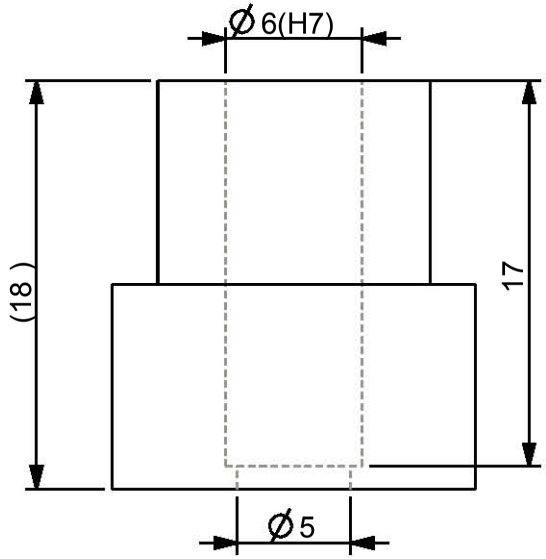


1

| Item | Name | Qty | Material |
|---|---|---|---|

| | | | | |
|---|---|---|---|---|
| | University of Cape Town<br>Department of Mechanical Engineering | | | |
| | Title<br>NUT AND GEAR | | | |
| Dimensions in mm<br>Tolerance U.O.S.<br>0.1 | Scale<br>3,000 | Date<br>07/05/2010 | Sheet<br>7 | of<br>10 |
| | Drawn By<br>Kathryn Rosie | | Drawing Number<br>-- | |

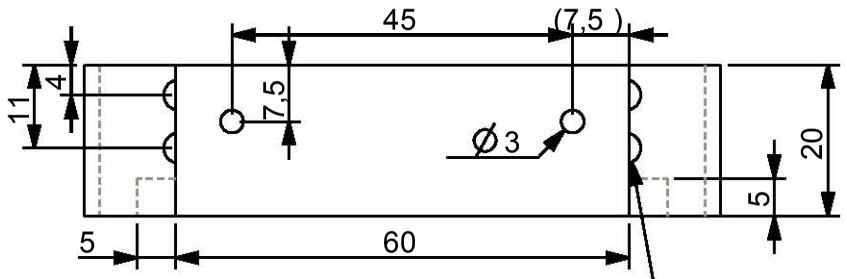


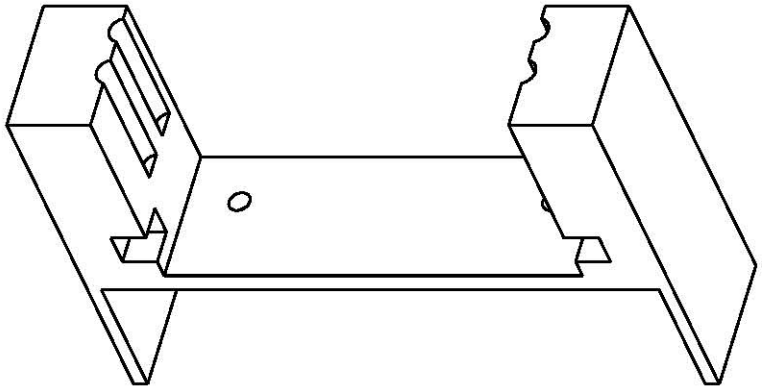

Ø4(H8), recessed into adjacent part by 0.5mm
Toleranced to allow pins to slide, but not rattle.

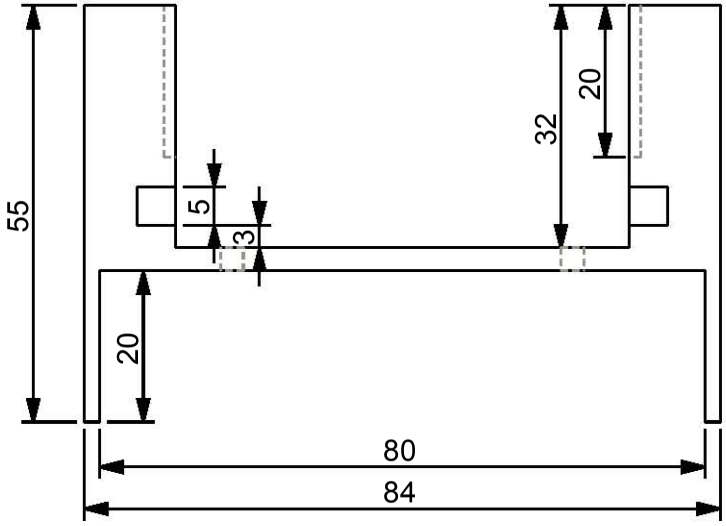


| Item | Name | Qty | Material |
|---|---|---|---|
| | | | |

University of Cape Town
Department of Mechanical Engineering

Title: FRONT SUPPORT

| Dimensions in mm Tolerance U.O.S. | Scale | Date | Sheet | of |
|---|---|---|---|---|
| 0.1 | 1,000 | 07/05/2010 | 8 | 12 |

Drawn By: Kathryn Rosie

Drawing Number: --

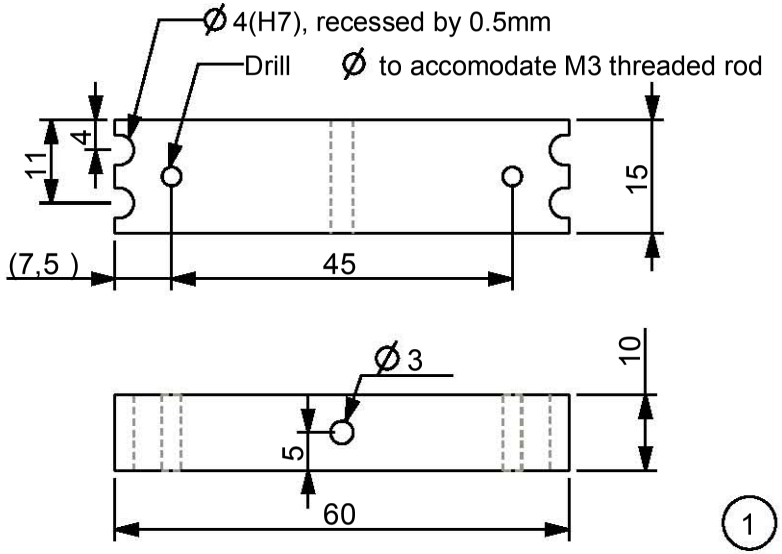


1

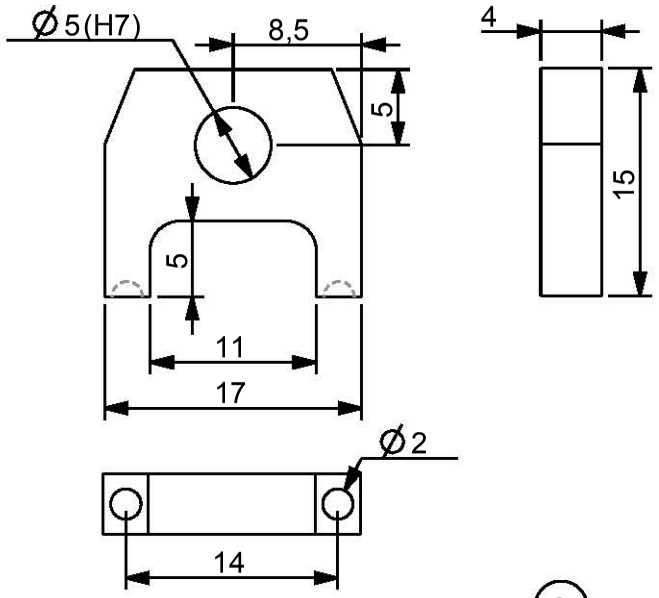


2

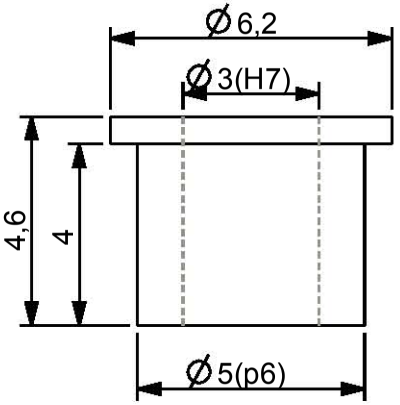


3

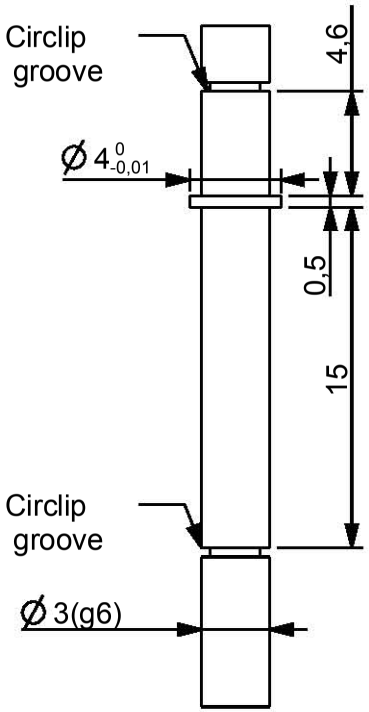


4

Crosshead/pin (pts 4&11): Press fit (H7/p6)
Front supp/pin (pts 5&11): Sliding fit (H8/p6)

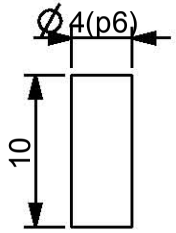


5

| Item | Name | Qty | Material |
|---|---|---|---|
| | | | |

University of Cape Town
Department of Mechanical Engineering

Title: PARTS DRAWINGS

| Dimensions in mm Tolerance U.O.S. | Scale | Date | Sheet | of |
|---|---|---|---|---|
| 0.1 | 1,000 | 07/05/2010 | 9 | 12 |

Drawn By: Kathryn Rosie

Drawing Number: --

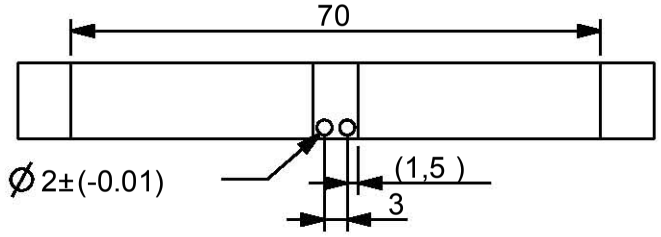


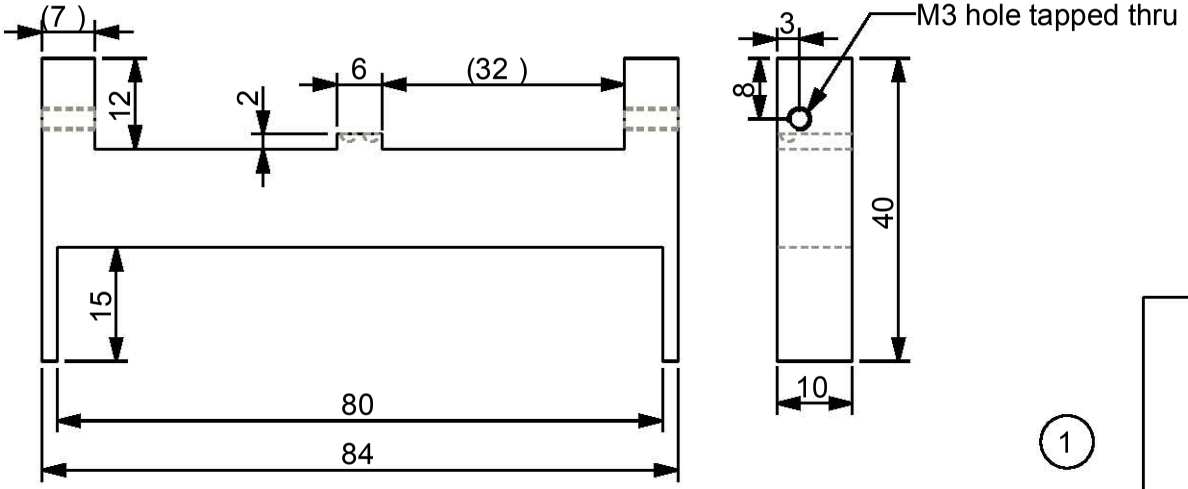


1

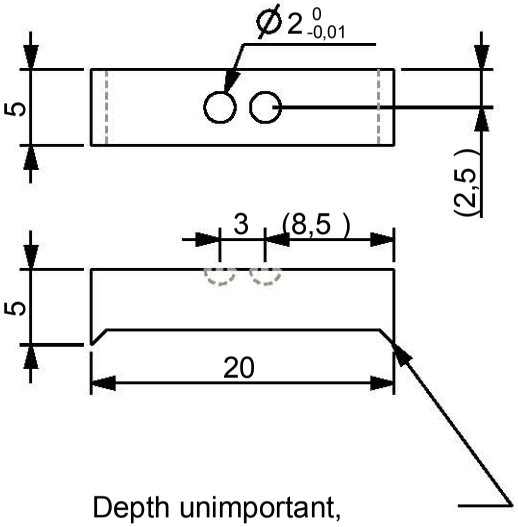


2

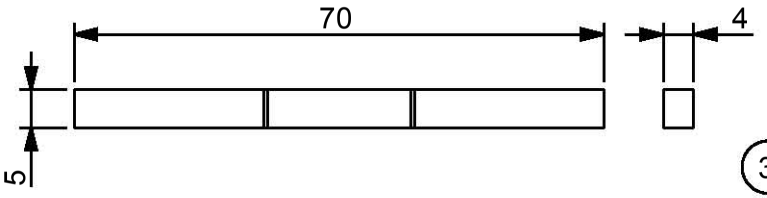


3

| Item | Name | Qty | Material |
|---|---|---|---|
| | | | |

University of Cape Town
Department of Mechanical Engineering

Title: PARTS DRAWINGS

| Dimensions in mm Tolerance U.O.S. | Scale | Date | Sheet | of |
|---|---|---|---|---|
| 0.1 | 2,000 | 07/05/2010 | 10 | 12 |

| Drawn By | Drawing Number |
|---|---|
| Kathryn Rosie | -- |

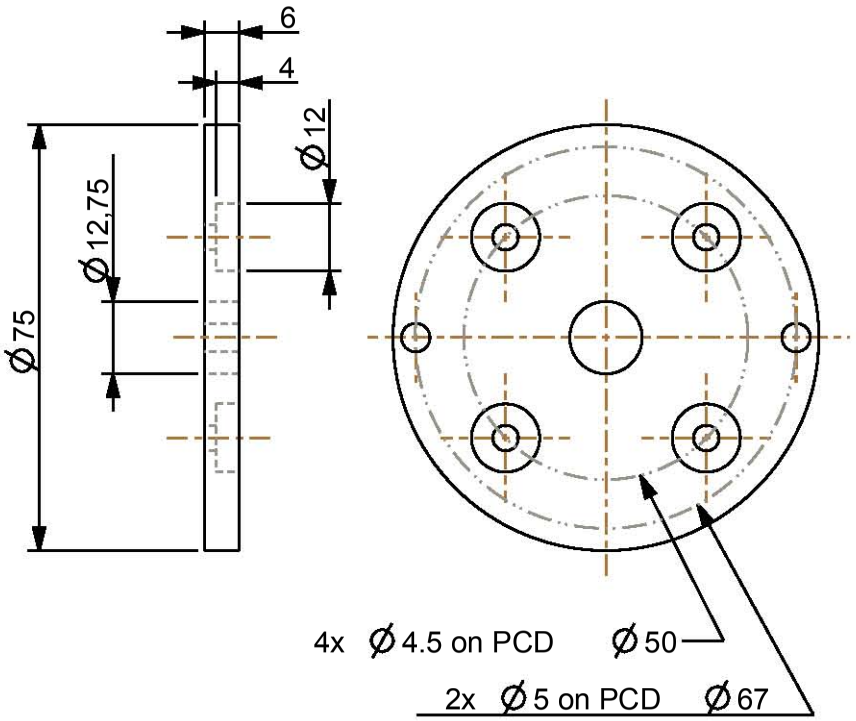


2

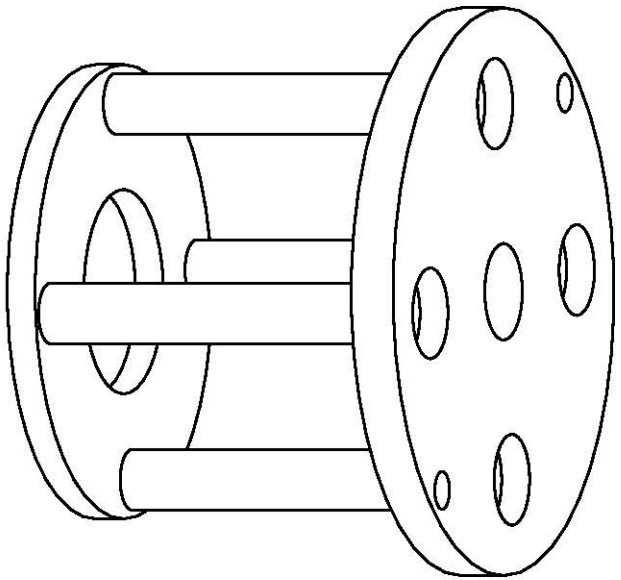

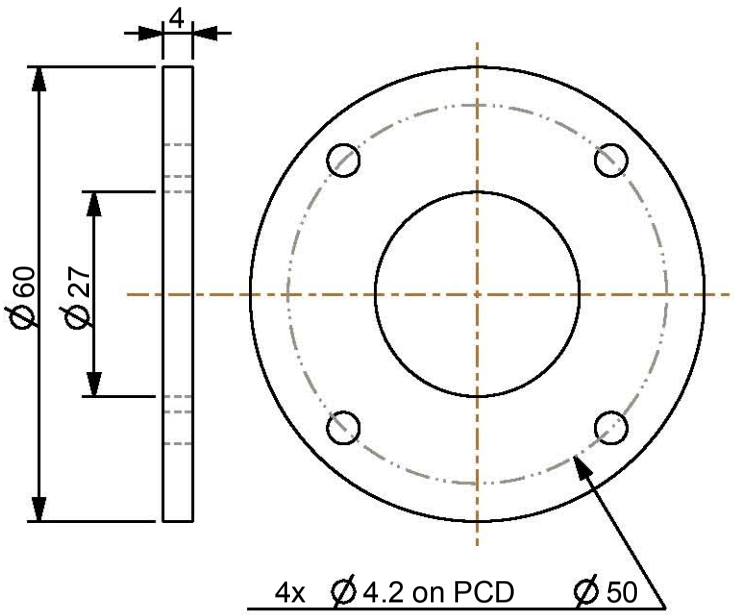


3

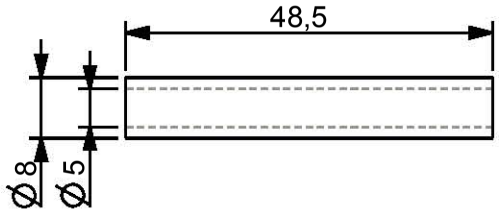


1

ALL PARTS STAINLESS STEEL

| Item | Name | Qty | Material |
|---|---|---|---|

| | | | | |
|---|---|---|---|---|
| | University of Cape Town<br>Department of Mechanical Engineering | | | |
| | Title<br>SEM/MOTOR ADAPTER | | | |
| Dimensions in mm<br>Tolerance U.O.S.<br>0.1 | Scale<br>1,000 | Date<br>01-Oct-10 | Sheet<br>11 | of<br>12 |
| | Drawn By<br>Kathryn Rosie | | Drawing Number<br>-- | |

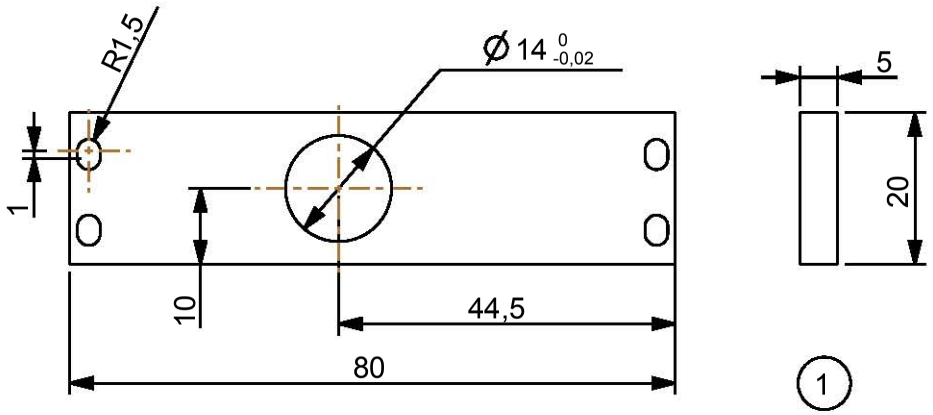


1

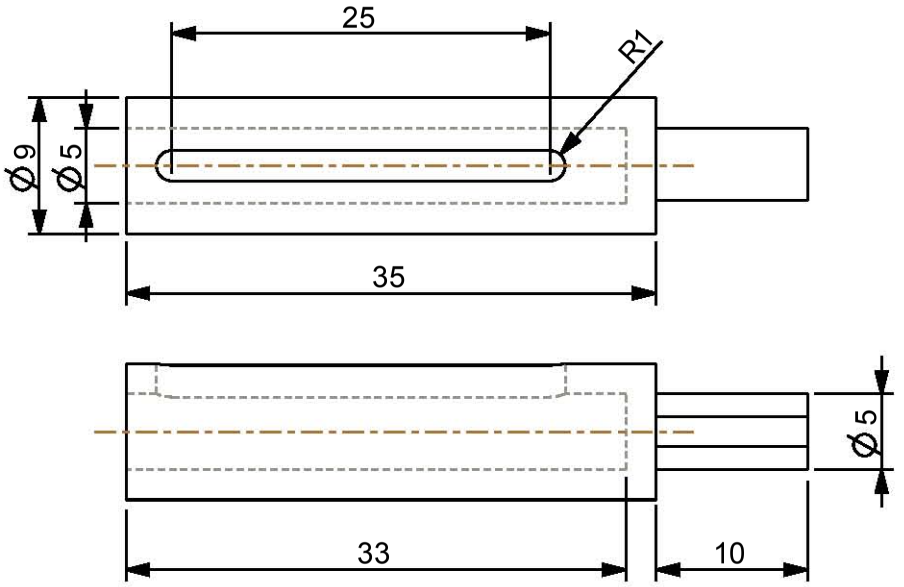


2

Mill 0.5mm in

| Item | Name | Qty | Material |
|---|---|---|---|
| | | | |

University of Cape Town
Department of Mechanical Engineering

Title
PARTS DRAWINGS

| Dimensions in mm Tolerance U.O.S. | Scale | Date | Sheet | of |
|---|---|---|---|---|
| | 2,000 | 07-Aug-2010 | 12 | 12 |
| | Drawn By | | Drawing Number | |
| 0.1 | Kathryn Rosie | | -- | |

# Appendix B

# Circuit Diagrams

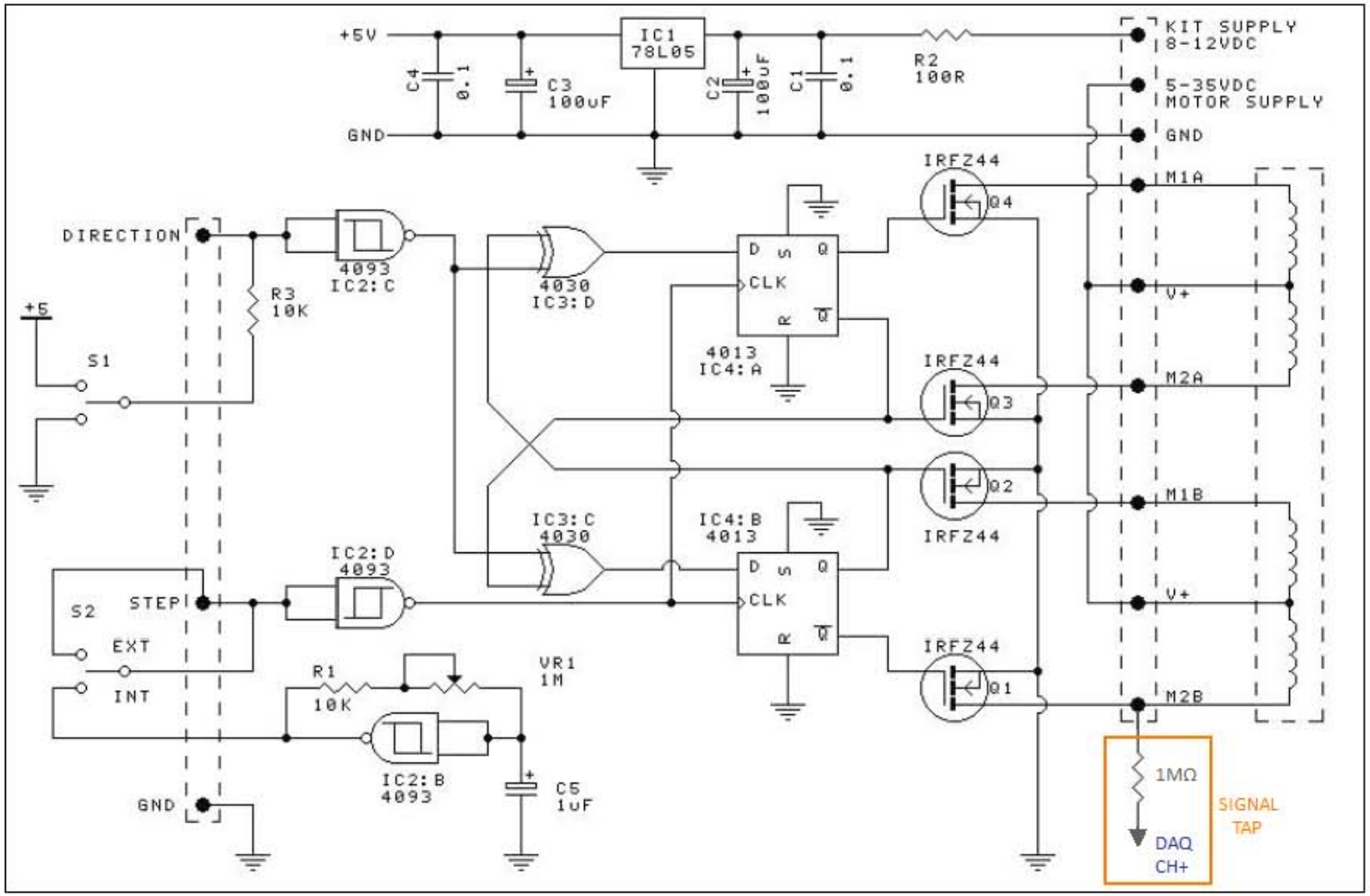


**Figure B.1:** Stepper motor control circuit, modified from the original KitsRUs diagram [82] to represent the signal tap from the circuit board to the DAQ, in order to determine motor speed.

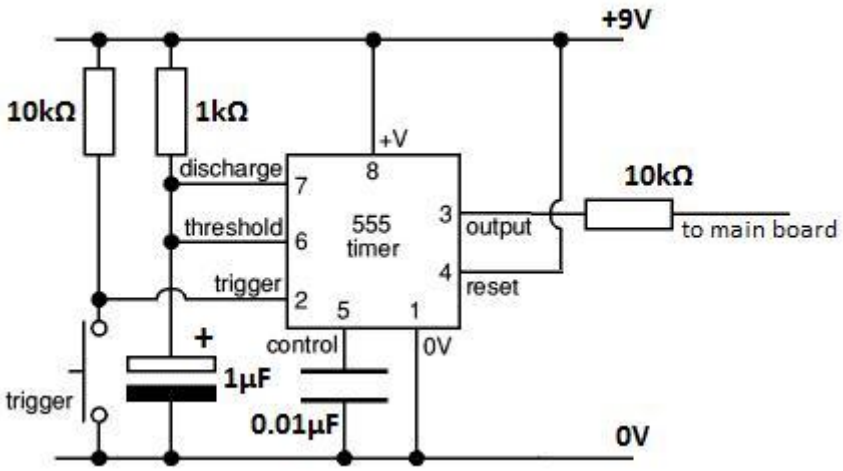


**Figure B.2:** Step function circuit. The output of this circuit connected to the 'EXT' line on the main board, shown as the 'STEP' junction in Figure B.1. This circuit is a 555 timer circuit setup in a monostable configuration, and is modified from the original by The Electronics Club [83].

# Appendix C

# Calculations

## C.1 Loading

### C.1.1 Thickness Correction Factor

This is the thickness correction factor automatically included in Evans' classic methodology for the analysis of stress intensity in a DT specimen. The variables $d$ and $W$ correspond to the dimensions of the DT specimen shown in Figure 3.1.

$$\begin{aligned} \tau &= \frac{2d}{W} \\ &= 2 \cdot \frac{1.5}{15} \\ &= 0.2 \end{aligned}$$

$$\begin{aligned} \psi &= 1 + 0.6302\tau + 1.2\tau \cdot e^{-\pi/\tau} \\ &= \underline{\underline{0.874}} \end{aligned}$$

### C.1.2 Required Load

The load that the rig would be required to transmit for a specimen having dimensions $45 \times 15 \times 1.5$mm, and a fracture toughness of 10MPa$\sqrt{\text{m}}$, in order to be certain of initiating a crack in that specimen.

$$
\begin{aligned}
P &= K_{Ic}\left(\frac{3w_m^2}{Wd^4(1-\nu)\psi(d,W)}\right)^{-1/2} \\
&= \left(10\times10^6\right)\left(\frac{3(0.007)^2}{0.015\cdot0.0015^4\cdot(1-0.2)\cdot0.874}\right)^{-1/2} \\
&= \underrightarrow{\sim 194\text{N}}
\end{aligned}
$$

# C.2 Strain Bar Evaluation

## C.2.1 Strain Bar Energy Release

The following calculations compare the energy released to crack growth of the thin ($t = 2\,\text{mm}$) and thick ($t = 4\,\text{mm}$) strain bars. Following from Figure 5.5, each calculation is based on the straight line relationship $y = mx$.

| | $t = 2\text{mm}$ | $t = 4\text{mm}$ |
|---|---|---|
| $m$ | 28483 | 94480 |
| $y_2$ | 50 | 50 |
| $x_2 = \frac{y_2}{m}$ | $1.8\times10^{-3}$ | $5.3\times10^{-4}$ |
| $y_1$ | 45 | 45 |
| $x_1 = \frac{y_1}{m}$ | $1.6\times10^{-3}$ | $4.8\times10^{-4}$ |
| Area | $9.5\times10^{-3}$ | $2.4\times10^{-3}$ |
| Quotient | 4 | |

# C.3 v-K Data for PMMA

## C.3.1 Load to Fracture Toughness

Strain data was read off the indicator and marked during the sequences shown in the clip *'PMMA_8_clip.wmv'*, and converted to load and stress intensity data via the calibration relationship of the 4mm strain bar.

| | State 1 | State 2 |
|---|---|---|
| Load, P | 24.7N | 24.1N |
| SIF, K (Eq. 3.2) | $24.7\sqrt{\frac{3\cdot(0.007)^2}{(0.015)\cdot(0.0015)^4\cdot0.874}}$ $= \underrightarrow{1.16\,\text{MPa}\sqrt{\text{m}}}$ | $24.1\sqrt{\frac{3\cdot(0.007)^2}{(0.015)\cdot(0.0015^4)\cdot0.874}}$ $= \underrightarrow{1.13\,\text{MPa}\sqrt{\text{m}}}$ |

### C.3.2 Video Capture Velocity Calculation

The time, $t$, taken for the crack to traverse the 0.1mm high field of view, from the bottom to the top of the screen, was timed in two instances:

| | State 1 | State 2 |
|---|---|---|
| Time, $t$ | 11s | 50s |
| Velocity, $v$ | $\frac{0.1\times10^{-3}}{11}$ $= \underrightarrow{9.1 \times 10^{-6}\text{m/s}}$ | $\frac{0.1\times10^{-3}}{50}$ $= \underrightarrow{2.0 \times 10^{-6}\text{m/s}}$ |

### C.3.3 Image Capture Velocity Calculation

The difference between the distance markers (consistent scale used) in successive PMMA images is shown in Figure 6.3 to be 2 units. Taking a ratio of this to the image scale marker, using the same consistent units (refer to the figures), to get the actual crack propagation, $y$, between the images:

$$\begin{aligned} y &= \frac{2 \cdot (10 \times 10^{-6})}{11.5} \\ &= 1.74\mu\text{m} \end{aligned}$$

Given that the time taken between the images is estimated at 90 seconds:

$$\begin{aligned} v &= \frac{1.74 \times 10^{-6}}{90} \\ &= 1.93 \times 10^{-8}\text{m/s} \\ &= \underrightarrow{19.3\text{nm/s}} \end{aligned}$$

# Appendix D

# Installation and Operation Procedure

This chapter describes the procedure that was followed in installing and operating the rig in the LEO S440 SEM at the Electron Microscope Unit, University of Cape Town. It also covers any considerations one should be mindful of when operating the rig.



## D.1 Installation of the Rig into the SEM

The main rig structure screws onto C-shaped brackets, which fits directly onto the SEM stage. However, in regular SEM use the rotation and tilt mechanism is already in place on these C-brackets. The following points cover the removal and storage of the rotation/tilt mechanism, starting with the chamber door open:

- Make sure there is no specimen stub in the mechanism. Remove it if there is, by means of the grub screw located in the base of the stub.
- Unscrew the mechanism from the C-brackets via the two cap screws in the base, on the right side of the mechanism (i.e. away from the door).
- As the mechanism cannot be fully dismantled from the SEM, it is stored at the top right corner of the chamber door as shown in Figure D.1. One should align the mechanisms so as the be as much out of the way of the DT rig as possible. It is secured in place by means of cable ties around the existing structures on the door.

The next few points cover the actual installation of the rig, starting with the provided universal joint attachments to the input shaft:

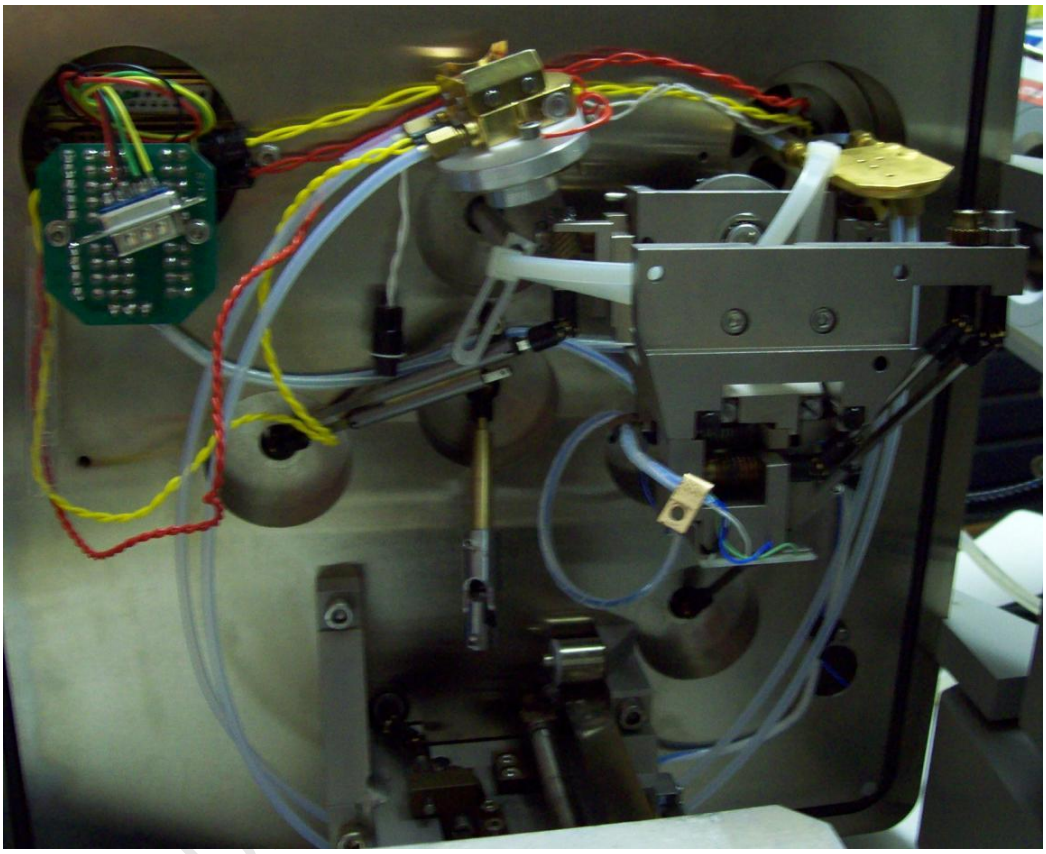

**Figure D.1:** Storage of rotation and tilt mechanism

- Attached the long side of the universal joint to the brass shaft protruding from the door of the SEM. Make sure the shaft is inserted as far as possible, without interefering with the gimbal of the universal joint. The joint is tightened via a grub screw.

- Insert the telescopic side of the rig input shaft into the short side of the universal joint, and tighten the grub screw as before.

- Sit the rig structure atop the C-brackets mounted onto the stage. Both available C-brackets should be used, as this ensures the specimen is at the correct height below the electron beam. Use long screws to fix the C-brackets to the stage.

- Attach the 9-pin strain bar connector to the matching adapter on the SEM door.

The chamber setup is now complete. The motor should now be attached to the exterior side of the chamber door, and is done using a brass spacer, an aluminium mounting bracket, a piece of silicon tubing, and a hand dial. Due to the compact nature of the eventual setup, there is a specific order in which the items are attached which allows the most ease in assembling the coupling.

- Remove the large diameter plate from the aluminium mounting bracket.

- Using M4 screws, attach the brass spacer and small side of the aluminium mount to the SEM door. There are screw holes available around the lower centre hand dial, marked 'ROTATE'. This is connected to the spare brass shaft inside the chamber.

- Slide the piece of silicon tubing over the SEM hand dial, and insert the spare dial into the open end, hollow side facing out.

- Reattached the large diameter plate to the rest of the mount. The silicon tubing and dials should be inserted such that their assembly is just housed inside the mount.

- Attached the motor to the mounting plate, making sure the motor shaft is inserted neatly into the open end of the spare hand dial. The dial is fixed to the shaft by means of a grub screw on the dial. A precision screwdriver is adequate to pierce the silicon tube and tighten the screw.

This concludes the installation of the rig and motor. The final connection to be made is the co-axial cable to the image converter located behind the SEM monitor. The other end of the cable is attached to the yellow component lead of the external USB capture card.

The following section describes the setup and operation of the system. It is, however, recommended that on first use the entire system should be set up with the door open so its operation can be checked before pumping down the chamber.

## D.2 Setup and Operation of the System

Before a test can begin, various electrical connections must be made for power and data logging purposes. The exterior setup requires a Vishay Measurements Group P-3500 strain indicator, and a computer with LabVIEW Signal Express, and video capturing software installed.

- Attach the wires from the 25-pin D-type connector on the SEM door to the correct terminals on the strain indicator.
- Connect the output of the strain indicator to one of the analogue input channels on the USB ni-DAQ (data acquisition card) using the connector wire provided.
- Setup USB power to:
  - the ni-DAQ acquisition card;
  - the video capture card;
  - the stepper motor hand control.
- Insert a specimen in to the rig, taking care of the alignment. If the crosshead is too far from the desired position on loading, it may be physically repositioned by loosening the supporting nuts. Load the specimen (via the motor) to a noticeable strain (i.e. 2 or 3 microstrain); this prevents the specimen from slipping as the door is closed.
- Close the chamber door, making sure the vacuum seal is cleared of any interference, and that there is nothing that will contact walls or door. It is imperative that the vacuum seal is clean and does not impact anything (even in error), as this could permanently destroy the vacuum integrity.

- Ensure there is a valid reading on the strain indicator, and that all the relevant shafts are turning, *before* venting the chamber.

- Close the door slowly, watching carefully in the chamber stereoscope that nothing is impacted while this happens. The chamber may now be vented and testing may begin.

The following points describe the use of the hand control for the motor, with reference to Figure D.2.

- Power to the circuit is controlled via the On/Off slider switch on the side of the control box (Item 1). This is the primary means of starting and stopping the rotation of the motor.

- The speed of the motor is varied through the dial on the side of the control box (Item 2) Clockwise speeds up the rotations, clockwise slows the rotations.

- The direction of the motor is controlled via a toggle switch (Item 3).

- Item 4 toggles the control circuit between 'continuous' and 'pulse' mode. In continuous mode, the motor rotates at a speed set by the dial control. In pulse mode, the push button (Item 5) may be used to pulse the motor in the given direction. Each pulse is 1/48th of a revolution. **The circuit should NEVER be left in pulse mode, as there is no current limiting, and prolonged use at this setting causes the motor coils, the circuit, and the 9V battery inside to overheat.**

The following is a list of tips that were determined to be important during the operation of the system for this thesis:

- Monitor the SEM system vacuum while rotating the motor. The port in use was originally designed for hand speeds, and various issues had to be overcome in making sure it could be used for this system. If the vacuum starts dropping when the motor is turned, lower the rotation speed, or pause a moment to let the vacuum recover.

- Avoid leaving the specimen loaded and the end of a test, even if it is to remain mounted in the rig. Unload to just above zero (again, in order to avoid slipping). This returns the strain bar to its natural state so as to avoid creep effects.


**Figure D.2:** Motor hand control.The respective items on the control are: (1) on-off switch; (2) speed control; (3) motor direction; (4) internal/external control; (5) pulse button; (6) USB connection point.

- Stepper motors do not start well under load. At higher specimen loads, if the motor starts slowing on startup, turn the speed dial to the slowest setting before starting the motor. It may be then be sped up. At the top end of the range there is a motor resonance, and the shaft will not turn. Lower the speed setting slightly if this is suspected.